# LARGE EDDY SIMULATION OF PRESSURE FLUCTUATIONS INSIDE STENOSED BLOOD VESSELS TOWARDS NONINVASIVE DIAGNOSIS OF ATHEROSCLEROSIS

A THESIS SUBMITTED TO
THE GRADUATE SCHOOL OF NATURAL AND APPLIED SCIENCES
OF
MIDDLE EAST TECHNICAL UNIVERSITY

BY

KAMİL ÖZDEN

IN PARTIAL FULFILLMENT OF THE REQUIREMENTS
FOR
THE DEGREE OF DOCTOR OF PHILOSOPHY
IN
MECHANICAL ENGINEERING

SEPTEMBER 2018

Approval of the thesis:

**LARGE EDDY SIMULATION OF PRESSURE FLUCTUATIONS INSIDE STENOSED BLOOD VESSELS TOWARDS NONINVASIVE DIAGNOSIS OF ATHEROSCLEROSIS**

submitted by **KAMİL ÖZDEN** in partial fulfillment of the requirements for the degree of **Doctor of Philosophy in Mechanical Engineering, Middle East Technical University** by,

Prof. Dr. Halil Kalıpçılar
Dean, Graduate School of **Natural and Applied Sciences** _____

Prof. Dr. Mehmet Ali Sahir Arıkan
Head of the Department, **Mechanical Engineering** _____

Assoc. Prof. Dr. Cüneyt Sert
Supervisor, **Mechanical Engineering Dept., METU** _____

**Examining Committee Members:**

Prof. Dr. Hakan Işık Tarman
Mechanical Engineering Dept., METU _____

Assoc. Prof. Dr. Cüneyt Sert
Mechanical Engineering Dept., METU _____

Assoc. Prof. Dr. Mehmet Metin Yavuz
Mechanical Engineering Dept., METU _____

Prof. Dr. Selin Aradağ Çelebioğlu
Mechanical Engineering Dept.,
TOBB University of Economics and Technology _____

Asst. Prof. Dr. Sıtkı Uslu
Mechanical Engineering Dept.,
TOBB University of Economics and Technology _____

**Date:** **06.09.2018**

**I hereby declare that all information in this document has been obtained and presented in accordance with academic rules and ethical conduct. I also declare that, as required by these rules and conduct, I have fully cited and referenced all material and results that are not original to this work.**

Name, Last name: KAMİL ÖZDEN

Signature:

# ABSTRACT

## LARGE EDDY SIMULATION OF PRESSURE FLUCTUATIONS INSIDE STENOSED BLOOD VESSELS TOWARDS NONINVASIVE DIAGNOSIS OF ATHEROSCLEROSIS

Özden, Kamil

Ph.D., Department of Mechanical Engineering

Supervisor: Assoc. Prof. Dr. Cüneyt Sert

Co-Supervisor: Assoc. Prof. Dr. Yiğit Yazıcıoğlu

September 2018, 148 pages

Atherosclerosis is a cardiovascular disease, in which plaque builds up inside a blood vessel, narrowing it down and forming a stenosis that adversely affects the flow. Because of the stenosis, turbulent flow occurs at the post-stenotic region, which causespressure fluctuations on the vessel wall. The resulting murmurpropogates through the surrounding tissue and reaches the skin surface. These sounds emitted from the stenosed vessels are evaluated as a sign of stenosis. In this study, large eddy simulations are conducted to investigate the turbulence-induced wall pressure fluctuations and resulting acoustic emission. In these simulations, the structures around the blood vessel are not modeled, the vessel wall is considered as rigid and only the flow inside the blood vessel is solved. Simulations are performed under both non-pulsatile and pulsatile flow conditions by using Newtonian and non-Newtonian fluid models. The two main parameters considered for this purpose are the stenosis severity and shape. The results show

that stenosis severity under a certain level does not cause disturbance at the post-stenotic region. For stenoses above this critical level, increasing stenosis severity has an intensifying effect on the wall pressure fluctuations. Eccentric stenosis morphology causes more severe fluctuations than an axisymmetric one. Stenosis shape affects both the magnitude of fluctuations and the duration in which the pressure fluctuations are intense during the pulsatile cycle. Obtained pressure fluctuations are converted into sound and investigated in terms of sound levels and patterns. Sounds emitted from the blood vessels with different stenosis severities and shapes have different sound characteristics, and provide important information about the stenosis. Therefore, both the stenosis severity and shape must be taken into account to develop an acoustic-based diagnostic system.

**Keywords:** Cardiovascular biomechanics, Pressure fluctuation, Non-invasive diagnosis of stenosis, Acoustic radiation, Stenosis severity, Stenosis shape, Large Eddy Simulation (LES)

# ÖZ

## ATEROSKLEROZUN GİRİŞİMSEL OLMAYAN TANISI YÖNÜNDE TIKALI KAN DAMARLARINDAKİ BASINÇ DALGALANMALARININ BÜYÜK GİRDAP SİMÜLASYONU

Özden, Kamil

Doktora, Makina Mühendisliği Bölümü
Tez Yöneticisi: Doç. Dr. Cüneyt Sert
Eş Tez Yöneticisi: Doç. Dr. Yiğit Yazıcıoğlu

Eylül 2018, 148 sayfa

Ateroskleroz, plağın kan damarı içinde biriktiği, daralttığı ve kan akışını olumsuz yönde etkileyen bir tıkanıklık oluşturduğu bir kardiyovasküler hastalıktır. Daralma nedeniyle, stenoz sonrası bölgede türbülanslı akış meydana gelir ve bu da damar duvarında basınç dalgalanmalarına yol açar. Bu etkileşimin neden olduğu üfürüm, damarı çevreleyen dokulardan yayılır ve deri yüzeyine ulaşır. Tıkalı damarlardan yayılan bu sesler, tıkanıklığın belirtisi olarak değerlendirilir. Bu çalışmada, daralma sonrasında oluşan türbülans kaynaklı duvar basınç dalgalanmalarını ve akustik emisyonu ayrıntılı olarak incelemek için büyük eddy simülasyonları yapılmıştır. Bu simülasyonlarda damar etrafındaki yapılar modellenmemiş, damar duvarı rijit kabul edilerek sadece damar içerisindeki akış çözülmüştür. Simülasyonlar, Newton tipi olan ve Newton tipi olmayan akışkan modelleri kullanılarak, hem atımlı olmayan hem de atımlı akış koşullarında gerçekleştirilmiştir. Stenoz şiddeti ve şekli bu amaç için odaklanılan iki ana parametre olmuştur. Sonuçlar, belirli bir seviyenin

altındaki tıkanıklık şiddetlerinin, daralma sonrası bölgede bozulmaya neden olmadığını göstermiştir. Bu seviyenin üzerindeki tıkanıklıklar için, stenoz şiddetinin artması, duvar basınç dalgalanmalarının şiddetini arttıran bir etkiye sahiptir. Eksantrik tıkanıklık morfolojisi, simetrik olanlara göre daha şiddetli dalgalanmalara neden olmuştur. Farklı tıkanıklık şekilleri hem basınç dalgalanmalarının büyüklüğünü hem de bu dalgalanmaların atımlı akış sırasında şiddetli olduğu süreyi etkilemiştir. Maksimum aktivite noktalarındaki duvar basıncı dalgalanma verileri sese dönüştürülmüş ve bu sesler seviyeleri ve biçimleri açısından incelenmiştir. Farklı daralma şiddetine ve şekillerine sahip damarlardan çıkan sesler farklı karakteristiklere sahip olduğundan, tıkanıklık hakkında önemli bilgiler sağlayabilirler. Bu nedenle, akustik temelli bir tanı sisteminin geliştirilmesi için, hem tıkanıklık şiddeti hem de şekli dikkate alınmalıdır.

**Anahtar Kelimeler:** Kardiyovasküler biyomekanik, Basınç salınımı, Damar tıkanıklığının girişimsiz teşhisi, Akustik yayılım, Tıkanıklık şiddeti, Tıkanıklık şekli, Büyük Girdap Benzetimleri

**To my wife Güzin and my daughter Sare**

## ACKNOWLEDGEMENTS

First and foremost, I would like to express my gratitude to my advisors Assoc. Prof. Dr. Cüneyt Sert and Assoc. Prof. Dr. Yiğit Yazıcıoğlu for their continuous support to my Ph.D study and for their guidance, patience and motivation. I would like to thank Prof. Dr. Selin Aradağ Çelebioğlu and Assoc. Prof. Dr. M. Metin Yavuz for their guidance, advice and insight throughout my research. I also would like to thank my colleague and roommate Hüseyin Enes Salman for his moral support and encouragement.

I am thankful to my friends Akif Hacınecipoğlu, Aykut Tamer, Bilal Atar, Muhammed Çakır, Mert İşler, Metin Biçer and Cihat Duru for their friendship and moral support.

Special thanks to TÜBİTAK ULAKBİM High Performance and Grid Computing Center and their technical support team for making it possible to use TRUBA HPC system efficiently in this thesis study.

I would also like to acknowledge and thank Middle East Technical University for the financial support under BAP-03-02-2014-001 and BAP-03-02-2017-006 scientific research projects during this study.

My sincere thanks goes to my parents, my brother and my sister for their love, support and trust. Without them it would be much harder to carry out this study. I have saved the last words of acknowledge to my beloved wife Güzin and to my dear daughter Sare. The period they have been with me during this study has been the best years of my life.

## TABLE OF CONTENTS

## LIST OF TABLES

TABLES

## LIST OF FIGURES

FIGURES

## LIST OF SYMBOLS

SYMBOLS

| | |
|---|---|
| $Re$ | Reynolds number |
| $p'_{RMS}$ | root mean square of pressure fluctuations |
| $p'$ | pressure fluctuations |
| $E_{pp}$ | frequency spectrum of the pressure fluctuations |
| $f$ | frequency |
| $\Delta f$ | unit frequency interval |
| $\rho$ | density |
| $t_{ij}$ | viscous stress tensor |
| $\Delta$ | filter width |
| $\Delta x, \Delta y, \Delta z$ | length, width and height of grid cells |
| $G$ | filter function |
| $\mu$ | dynamic viscosity |
| $\nu$ | kinematic viscosity |
| $\nu_{sgs}$ | subgrid kinematic eddy viscosity |
| $\dot{\gamma}$ | shear rate |
| $\tau_{ij}$ | subgrid-scale stress term |
| $C_s$ | Smagorinsky constant |

| | |
|---|---|
| $S_{ij}$ | rate of strain tensor |
| $Co$ | Courant number |
| $St$ | Strouhal number |
| $\Delta t$ | time step |
| $e$ | percent eccentricity |
| $\delta$ | vertical shift of the axis of the stenosed section from the main vessel axis |
| $y^+$ | wall unit normalised wall distance |
| $\eta$ | Kolmogorov length scale |
| $\varepsilon$ | rate of dissipation of turbulence kinetic energy per unit mass |
| $A$ | cross-sectional area |
| $\vec{\omega}$ | vorticity |

SUBSCRIPTS

| | |
|---|---|
| $eff$ | effective |
| $sgs$ | subgrid scale |
| $res$ | resolved |
| $throat$ | throat of the stenosis |
| $inlet$ | inlet of the blood vessel |

## LIST OF ABBREVIATIONS

| | |
|---|---|
| AD | Acoustic Detection |
| CFD | Computational Fluid Dynamics |
| CSA | Cardiac Sonospectrographic Analyzer |
| CT | Computerized Tomography |
| CV | Control Volume |
| CVD | Cardiovascular Disease |
| DES | Detached Eddy Simulation |
| DNS | Direct Numerical Simulation |
| FFR | Fractional Flow Reserve |
| FVM | Finite Volume Method |
| LES | Large Eddy Simulation |
| MRA | Magnetic Resonance Angiography |
| PDE | Partial Differential Equations |
| PIMPLE | Combination of PISO and SIMPLE Algorithms |
| PISO | Pressure-Implicit with Splitting of Operators |
| RANS | Reynolds Averaged Navier-Stokes |
| RMS | Root Mean Square |
| SGS | Subgrid Scale |

| | |
|---|---|
| SIMPLE | Semi-Implicit Method for Pressure-Linked Equations |
| TKE | Turbulent Kinetic Energy |

# CHAPTER 1

# INTRODUCTION

This section will first provide general information about initiation, progression and complications of atherosclerosis. Then the methods used for diagnosis of this disease will be mentioned and examined in terms of their deficiencies. A literature survey will be given, followedby a section that explains the scope and motivation of the thesis. This chapter will be finished with a general outline of the thesis.

## 1.1 Atherosclerosis

Cardiovascular diseases (CVD) such as coronary heart disease, cerebrovascular disease, peripheral arterial disease, heart attack and stroke are at the top of the causes of mortality throughout the world. These diseases leads more than 17.9 million deaths per year in 2015, a number that is expected to grow to more than 23.6 million by 2030 [1]. Atherosclerosis (stenosis), the major cause of most CVD, is a chronic disease results from accumulation of lipoproteins and inflammation of white blood cells as monocytes and T-cells into the artery wall [2]. This decomposition is initially in the form of a fatty tissue, then transforms into a composite material called atherosclerotic plaque or atheroma. A coronary artery with atherosclerosis is seen in Figure 1.1.

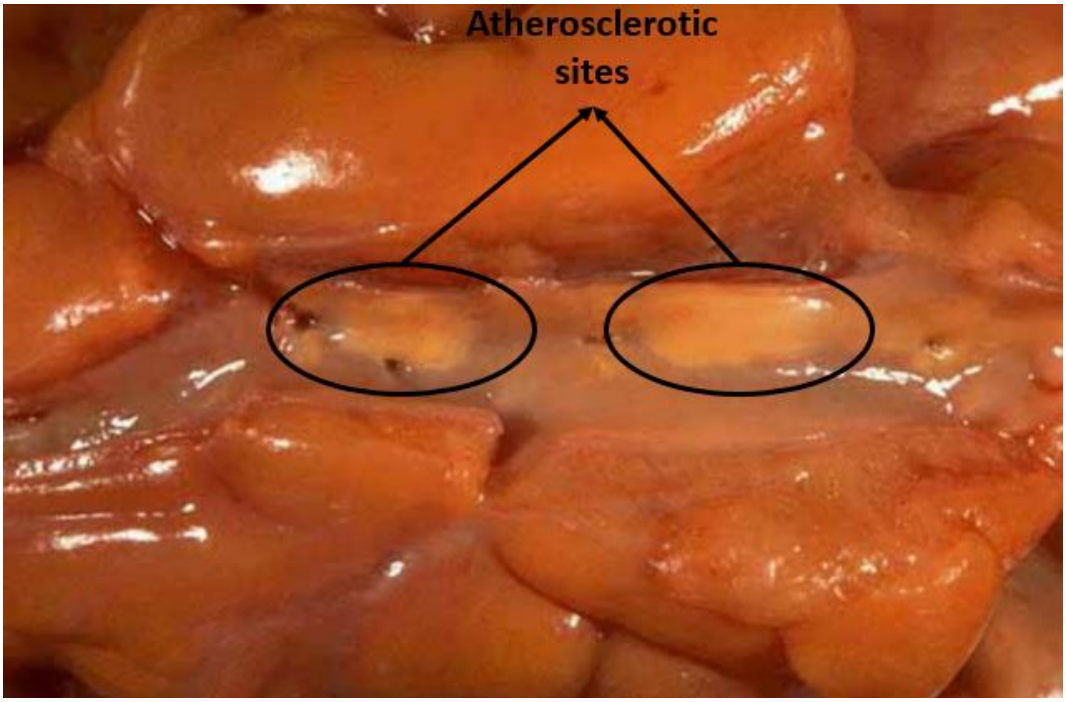


Figure 1.1. Atherosclerosis in a coronary artery (adopted from [3])

The development of atherosclerosis is a gradual process and usually does not show any symptoms if the narrowing of the lumen is not so severe to block blood flow to the tissues or organs. Sometimes, without any symptoms, plaque rupture and thrombus formation can lead to a heart attack or stroke. Microscopic images showing a healthy blood vessel, an atherosclerotic vessel and thrombus formation after plaque rupture are presented in Figure 1.2. If symptoms occur, the severity of them may vary depending on which vessel is affected by atherosclerosis. If there is atherosclerosis in one of the heart vessels, chest pain (angina) may be felt. When atherosclerosis affects one of the vessels leading to the brain, the symptoms can be sudden weakening in the arms or legs, loss of vision in one of the eyes, difficulty in speaking or drooping in the facial muscles. Atherosclerosis in the kidney vessels may lead to symptoms as high blood pressure and kidney failure. All of these symptoms that occur when atherosclerosis reaches a serious size can lead to

permanent damage in the body and even death, so early diagnosis of the disease is of great importance.

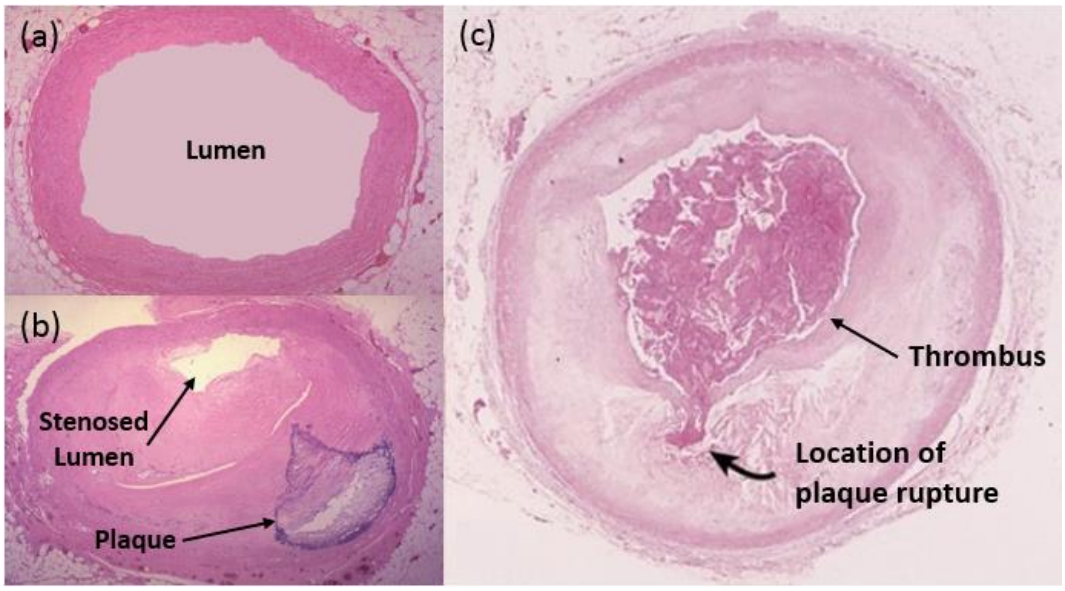


Figure 1.2. Microscopic images of (a) healthy vessel (b) atherosclerotic vessel and (c) thrombus formation after plaque rupture (adopted from [3])

## 1.2 Diagnosis of Atherosclerosis

The most common methods for diagnosing stenosis are as follows. Doppler ultrasound is a test in which high frequency sound waves are used to examine blood flow by taking measurements from various points on vessels that usually provide blood to the arms or legs. Computerized tomography (CT) scan is another diagnosis method using X-rays and computers to produce cross-sectional images of arteries. This method may provide more detailed information than an ultrasound test. However, high doses of radiation are involved in CT scanning which generates a risk of childhood cancer and leukemia in mothers who have imaging during pregnancy [4]. As an alternative to these methods, Magnetic resonance

angiography (MRA) can be used. MRA employs a powerful magnetic field and radio waves to visualize and diagnose atherosclerotic blood vessels. An important drawback of MRA is that it does not depict small vessels or extremely slow blood flow.

Another common technique for diagnosing atherosclerosis is arteriography. The basis of arteriography is the injection of an X-ray contrast agent into the body and obtaining the X-ray image, by which the place of stenosis and degree of narrowing can be detected. This method works better than MRA especially in smaller blood vessels. Arteriography has some risks such as kidney damage due to radiation exposure from X-rays used. In addition, X-ray angiography becomes error-prone if the blood vessel geometry is noncircular since it employs a projected view of vessel geometry [5, 6]. Fractional flow reserve (FFR) is another measurement method developed in 1990s for evaluation of functional significance of stenoses in the coronary arteries. This method is based on the pressure differential across the stenosis. FFR is considered as a gold standard to assess whether any stenosis may lead to ischemia or not [7]. However, both arteriography and FFR are invasive methods in which a catheter has to be placed into the body, which may lead to bleeding or infection after the operation. In addition, injury may occur at the catheterized artery and plaque on the inside of the arterial wall may be dislodged which trigger a stroke or heart attack. Apart from these, all the diagnosis techniques mentioned above are expensive, time consuming and usually only used when a stenosis results in serious clinical symptoms [8]. Therefore, these are not preventive methods, but are carried out in order to determine the extent of the disease.

One of the promising alternative ways to detect stenosis is based on flow induced acoustics. It is well known that distinct sounds known as murmurs emerge from stenosed arteries which can be listened by means of a stethoscope. This non-invasive, inexpensive and safe diagnosis technique is called as auscultation.

Recording and analyzing the sounds produced by blood flow to estimate the extent of arterial stenosis is known as phonoangiography. One of the earliest phonoangiography studies is done by Kartchner and McRae [9] empirically in 1969. They proposed the analysis of cervical bruits, which they called carotid phonoangiography, to obtain information about the extent of carotid stenosis. With their technique, a microphone was applied to the skin at several locations in the neck over the course of the carotid artery, the sounds amplified, and the time series displayed on the face of a cathode ray tube. Sounds that extended into diastole were judged to represent significant internal carotid stenosis, whereas those that were short and systolic were considered radiated or arising from the external carotid artery. Unlike this empirical method, Lees and Dewey [10] analytically showed that amplitude of murmur is proportional to eighth power of ratio of unstenosed diameter to stenosed diameter. This means that small changes in the stenosis size will bring about large changes in sound amplitude. After some initial success in symptomatic patients [11, 12], later studies applying this method to larger, less selective subjects demonstrated poor results for predicting stenosis severity [13, 14, 15]. As the method came into more widespread use and many patients with radiated bruits and with symptoms that arose from diseases other than stenosis formed an ever larger fraction of those studied, the percentage of correct diagnoses became very close to that to be expected by chance. Especially for sounds with frequencies lower than 200 Hz caused by low and mild stenoses, these techniques are poorly predictive of degree of stenosis in asymptomatic patients [13, 14]. Although phonoangiography is not currently used clinically, by means of some research projects it has been investigated whether the use of this method especially at near-surface veins such as carotid vessels, will yield positive results or not [16]. As can be understood, there is still a need to further work at the point of developing non-invasive diagnosis methods using the murmurs caused by turbulent wall pressure fluctuations at stenosed blood vessels.

## 1.3 Literature Survey

The following sections summarize the literature to-date concerning wall pressure fluctuations and emission of the sound due to post-stenotic turbulence. An overview of the clinical-experimental and numerical ones of these studies is presented in a chronological order under sub-sections 1.3.1 and 1.3.2, respectively.

### 1.3.1 Clinical – Experimental Studies

The history of clinical-experimental studies investigating turbulent wall pressure fluctuations and resulting murmurs at the post-stenotic region dates back to the early 1970s. In the first of these studies, Lees and Dewey [10] proposed an acoustic based method called phonoangiography for non-invasive diagnosis of stenosis. They attempted to define the mechanics of sound production by turbulent blood flow and to find an exact solution to relate the sound spectrum detected at the skin to the geometry of the arterial narrowing that produced it. Lees and Dewey proposed an exact relationship between the severity of arterial stenosis, the blood flow velocity, and the sound produced. According to this relation sound produced is proportional with eight power of the ratio of vessel diameter to stenosis diameter. Within the scope of this study, they used the data gathered from two patients with known severe stenosis to confirm the method they proposed.

In a follow-up study, Duncan and co-workers [17] showed that a murmur produced by turbulent blood flow has an energy spectrum against frequency. As frequency increases, the slope of this spectrum changes. The frequency at the position of slope change is called "break frequency", $f_0$, and used to determine the diameter of the stenotic region, $d$, with a simple relationship $d = US/f_0$, where $U$ is the flow velocity and $S$ is the Strouhal number.

Turbulence spectra is measured downstream of blunt shaped stenoses with various severities inside a rigid tube by Kim and Corcoran [18]. Measurements were made at a $Re$ range of 800-2000 by using water as working fluid. It is determined that as

stenosis severity increases the turbulence intensity at post-stenotic region increases for each $Re$. Clark [19, 20] also made turbulent velocity and wall pressure measurements by using a number different shaped nozzles with three degrees of stenosis severity. Non-dimensional power spectra of the maximum intensity were found to be almost independent of stenosis severity and shape, except for oblique nozzles.Tobin and Chang [21] obtained wall pressure spectra at various post-stenotic positions of axisymmetric blunt stenosis model under non-pulsatile flow conditions. Four different stenosis severities between 75%-95% are used over a range of $Re$ of 800-3100. Good universal correlations between spectrum frequency and pressure amplitude with degree of stenosis and a universal power spectral density function at the position of maximum wall pressure fluctuation are achieved. Fredberg [22] conducted experiments with an elliptic stenosis model to investigate the origin and character of vascular murmurs. Five different severities of stenosis models between 55%-91% are used. Main outcome of this study is that the distance downstream of the stenosis at which the mean-square fluctuating pressure reaches its maximum intensity depends to stenosis severity and fluid viscosity.

Kirkeeide et al. [23] conducted experiments in which vessel wall vibrations due to flow through axisymmetric blunt stenosis models with a severity range of 57%-91%. The stenoses are inserted into two different flexible tubes. The flow through the models is non-pulsatile, with the $Re$ ranging from 400 to 5000. Wall vibration intensity is found to be dependent on vessel wall properties, stenosis severity and Re.

Phonoangiography method is tested by Kistler et al. [24] by using 27 carotid bruits of 15 consecutive patients. Correct diagnosis of presence and severity of stenosis is made in 25 of 27 cases (92%) despite the presence of a radiated murmur. Miller et al. [25] also conducted an experimental study to validate phonoangiography. External blunt stenosis with three different stenosis severities is applied to the aorta of dogs. The analysis of the bruits obtained from 10 dogs showed that the relationship between flow through the stenosis and break frequency of the bruit is

linear. Knox et al. [26] assessed 116 carotid artery bruits using phonoangiography. The diameter of the vessel at the site of stenosis estimated by phonoangiography and arteriography were compared and found to agree within 1 mm of each other in 85% of patients.

Lu et al. [27, 28] conducted two different studies investigating intravascular pressure fluctuations and blood flow turbulence. In the earlier of them [27], experiments were carried out intraoperatively in open-chest calves with 40% and 60% stenoses. Energy spectra of velocity fluctuations showed a range of -5/3 power slope in the flow energy spectra which break into -10/3 power slope at approximately 100 Hz. However, it is not possible to talk about distinct slopes in the same frequency range. In the second one [28], an axisymmetric 90% stenosis model in a rigid plexiglass pipe was used to study the velocity and pressure fluctuations downstream downstream of the stenosis. It is found that the differences between peak frequencies of the pressure spectra and the characteristic frequencies of the velocity spectra vary with positions downstream from the stenosis.

Jones and Fronek [29] conducted experiments under non-pulsatile flow conditions with a $Re$ range of 500-1500 for the purpose of improving phonoangiography. They used five different stenosis severities between 50%-90%. An empirical relationship between Strouhal number, stenosis severity and the $Re$ is obtained. Abdallah and Hwang [30] have studied the flow and pressure field in terms of their relation to the murmurs emitted from stenosed arteries. The correlations performed between velocity and pressure fluctuations showed that the main cause of pressure fluctuations is the passage of turbulent eddies with a convective velocity that is a function of the jet exit velocity.

More recently, several experimental studies are conducted by Borisyuk [31, 32, 33, 34] to evaluate the relation between wall pressure fluctuation behind a stenosis and the noise emerged from a stenosed artery. The main findings of these studies can be listed as follows. The stenosis generated acoustic power is found to be approximately proportional to the fourth power of the stenosis severity and fourth

power of the flow's $Re$. The shape of the spectrum of wall pressure fluctuations does not practically depend on stenosis severity and $Re$. However, the spectrum level generally increases/decreases as stenosis severity and (or) $Re$ increase/decrease. The study of the effect of the stenosis eccentricity on the wall pressure statistical characteristics shows that the frequency spectrum is more sensitive to the changes in the eccentricity compared to the root-mean-square pressure. Finally, the characteristic acoustic signs of the presence of the narrowing have been found to be a general increase in the levels of the acoustic power spectrum.

Yazıcıoğlu et al. studied the vibration of a thin-walled cylindrical, both rigid and compliant viscoelastic tube with an 87% blunt axisymmetric stenosis [35]. Wall pressure fluctuations on the inner wall and radial velocity responses at the outer surface of the thin vessel wall are investigated. Experimental measurements are compared with empirical correlations of Tobin and Chang [21] with similar trends in terms of amplitude and spatial-spectral distribution of acoustic radiation. It has been found that spectral distribution of acoustic pressure intensities are almost same for rigid and elastic vessels at the post-stenotic region.

### 1.3.2 Numerical Studies

Numerical studies related to the stenotic vessels became popular in the late 90s because of the capability of gaining better insight into and visualizing properly the post-stenotic flow field. These studies will be summarized below.

Mittal et al. [36, 37] applied large eddy simulation (LES) and direct numerical simulation (DNS) to investigate pulsatile flow through a modeled arterial stenosis as an extension of study of Tutty [38] to 3D. A simple stenosis model has been used that consists of a one-sided 50% semicircular stenosis in a planar channel. In the earlier study, simulations are preformed under pulsatile flow conditions with a peak $Re$ of 2000. As finding of this study it can be said that the higher the energy level of pressure fluctuations at break frequency at which these sounds are generated, the

more the potential of them being transmitted through the arterial wall and being detectable by means of non-invasive means. In the second study, non-pulsatile flow simulations have been carried out over a range of $Re$ from 750 to 2000. Examination of the wall pressure fluctuations indicates that the highest intensity occurs roughly 3–4 channel heights downstream of the stenosis where the separated shear layers impact on the channel walls.

Varghese et al. [39, 40] examined non-pulsatile ($Re$ = 500 and 1000) and pulsatile flow ($Re_{mean}$ = 600) through 75% stenosed tubes using DNS. Both axisymmetric and eccentric morphologies of stenoses are used. The introduction of a geometric perturbation in the form of a 5% stenosis eccentricity of the main vessel diameter at the throat, resulted in transition to turbulence. The early part of decelaration is found as the stage of pulsatile flow where turbulent activity is maximum.

Paul et al. [41] performed LES to study pulsatile flow through an elliptic 50% stenosed model. It has been found that the magnitude of the velocity fluctuations is recorded high at the middle position of every cycle, because of the pulsatile velocity profile which gets maximum at the mid-cycle location. This research showed that LES has the capability of modelling time-accurate transition to turbulent pulsatile flow. Physiological pulsatile flow, with $Re$ varying between 800-1800, through 60% and 70% stenosed channels is simulated with DNS by Khair et al. [42]. It is observed that turbulent kinetic energy (TKE of the flow field is dependent upon the $Re$. In the viscous dissipation subrange of turbulence spectrum of velocity fluctuations TKE eventually converted into thermal energy through the mechanism of molecular dissipation.

Molla and Paul [43] studied pulsatile flow through a channel with double stenosis of 50% severity using LES. Due to the presence of the second stenosis, the turbulent intensity of the flow increased significantly. Seo and Mittal investigated the effect of stenosis severity on acoustic radiation using 2D vessel models with 50% and 75% of stenosis degrees [44] and reported that amplitude of acoustic pressure fluctuations increases significantly for the 75% case. It is found that the bruits are

related primarily to the time-derivative of the integrated pressure force on the post-stenotic segment of arterial wall. Zhu et al. [45] extended this study and developed a new approach to investigate the biomechanics of arterial bruits by including the effect of shear wave propagation on signals obtained from the skin surface. They found that compression and shear waves affects the emitted sound signals from different locations of post-stenotic region. In another study, Seo et al. [46] developed what they called a computational hemoacoustic method that simulate the blood flow inside a stenosed vessel using the immersed boundary technique and the propagation of the generated sound through the surrounding tissues using a linear elastic wave equation.

As a follow up study Salman et al. [47] studied the same problem of Yazıcıoğlu et al. [35] numerically. Although their findings showed good agreement with the reference results in terms of spectral characteristics of wall pressure fluctuations, there was a significant difference in amplitudes. In order to bring these studies one step further, Salman and Yazıcıoğlu [48, 49] modeled the flow-induced pressure field in a stenosed artery as broadband harmonic pressure loading and applied on the inner artery wall. These studies are conducted under non-pulsatile flow conditions with $Re$ of 1000 and 2000. Five different stenosis severities between 50% and 95% are used. Results indicate that stenosis severities higher than 70% lead to significant increase in response amplitudes, especially at high frequencies between 250 and 600 Hz. Moreover, it is observed that increasing level of stenosis leads to an increase in pressure amplitudes on the skin surface where the region which is closest to the stenosed artery has the highest pressure amplitudes.

Very recently, Özden et al. [50] numerically investigated the physiological pulsatile flow through axisymmetrically and eccentrically stenosed realistic and ideal vessel models. It has been found that eccentricity increases the intensity of wall pressure fluctuation and resulting acoustic emission. The difference between the results of axisymmetric and eccentric models in the use of ideal vessels is markedly reduced when real vessels are used.

Note that the literature survey about clinical - experimental and numerical studies are summarized in Tables 1.1 and 1.2, respectively.

### 1.3.3 Recent Technologies

In this section, information about recent technologies employed in non-invasive diagnosis of stenosis is presented. Although all of the studies mentioned above contain valuable information, it is difficult to use these information in clinical practice for acoustic-based diagnosis of vascular stenosis. In recent years, significant technologies have been developed for this purpose.

One group of these technologies focused on acoustic detection (AD) of coronary artery disease (CAD). Since the acoustic signature of coronary turbulence is too faint for the unaided ear, specialized microphone sensors or stethoscopes are required. The sensor to skin interface requires specific considerations for impedance matching, pressure application and exclusion of background noise. Furthermore, even after amplification of the emanated noise, coronary turbulence is buried in the competing sounds of the cardiac and thoracic structures. Performance of all AD tests requires a quiet environment to minimize interference. An effective AD method requires data-filtering algorithms and analytics to isolate the specific target signals used for diagnosis.

The cardiac sonospectrographic analyzer (CSA) consists of a stethoscope-like transducer attached to an amplifier and a portable computer. The system is designed to detect microbruits, characteristic of abnormal blood flow in atherosclerotic arteries. A computer algorithm helps generate a microbruit score of 0 (low probability of clinically significant disease) or 1 (high probability of clinically significant disease). Makaryus et al. [51] tested the accuracy of CSA electronic stethoscope and found that the overall sensitivity of the CSA to identify >50% stenosis in any major coronary artery as determined by CT imaging was 89.5%. However, the success rate was much lower when detecting stenosis severities

below 50%. Therefore, this technology can not be used for prevention and early detection. Moreover, these stethoscopes are very sensitive to electronic and ambient noises which may dirt the murmurs radiated because of stenosis [52].

CADence [53] and CADScor [54] are two recent commercialized examples of AD systems. CADence system is composed of a sensor that incorporates a microphone sensor, ambient noise management and data pre-filtering. The handheld device uses wireless technology to transfer acoustic data to a cloud-based analytic engine. Data is collected at four chest wall sites seen in Figure 1.3. with each reading taking 30 s. After upload and analysis, the results are electronically returned to the clinician in under 10 min. The diagnostic conclusions are classified as either negative, positive or inconclusive for turbulence associated with obstructive CAD [55]. CADence system is tested by Azimpour et al. [56] on 123 subjects with CAD prevalence of 52%. A success rate of 70% is obtained in diagnosing CAD with ≥50% severity when compared with angiography results.

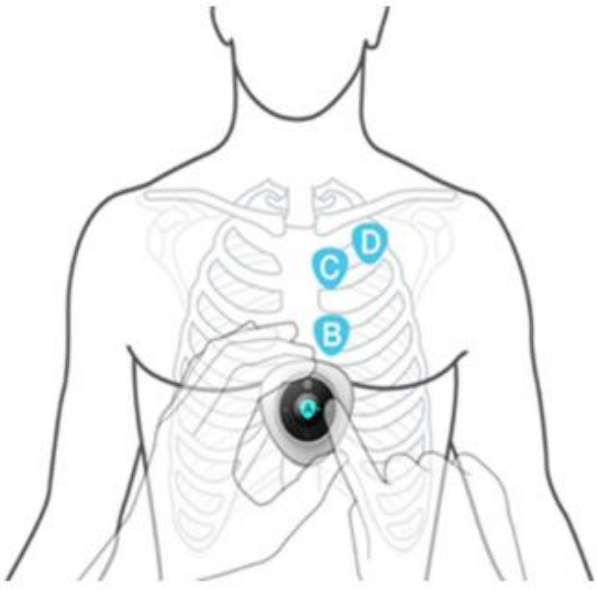


Figure 1.3. CADence handheld device and testing sequence [55]

The CADScore system is comprised of a palm-sized acoustic analyzer with a flexible connection to an adhesive sensor that is applied to the chest wall at the fourth left inter-costal space seen in Figure 1.4. There is a separate base console that recharges and calibrates the analyzer. A 3 min recording is performed on the supine patient with 4 separate breath holds to reduce acoustic interference [55]. Findings are reported numerically along a range from 0 to 100 CADScore points: low (<20), inter- mediate (20–30), and high (>30). The performance of CADScore is being evaluated by Winther et al. [57] on 228 subjects and obstructive CAD was diagnosed in 63 patients (28 %). Obstructive CAD was defined as more than 50 % diameter stenosis diagnosed by quantitative analysis of the invasive angiography. Diagnostic accuracy was 72 % for the CADScore system.

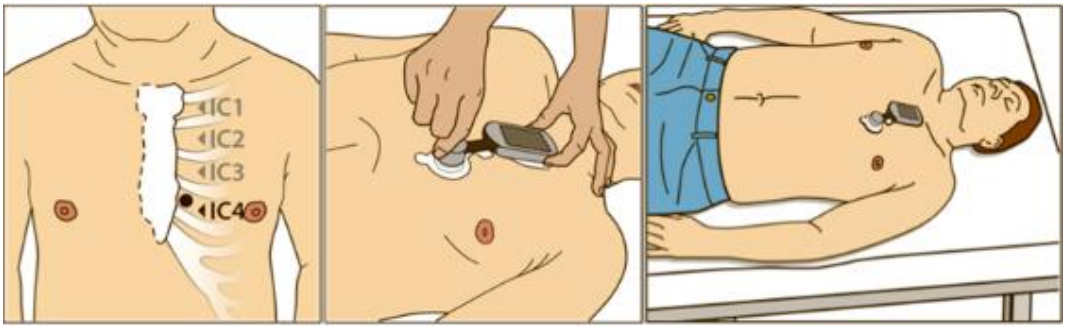


Figure 1.4. Schematic drawing of the placement and recording procedure of CADScore system [54]

There are significant potential limitations inherent to these systems. Although, CSA and CADence systems record signals from multiple chest wall sites, the AD technologies can not localize the anatomic origin of coronary turbulence or specify individual diseased vessels. Therefore, the impact of single- versus multi-vessel disease on AD accuracy is unknown. Furthermore, patients with noisy chests due to valvular murmurs or lung conditions have generally been excluded from the initial studies so the applicability of AD in these populations is another point that

is not fully understood. These issues require clarification in large numbers of subjects with angiographic validation. [55]

Table 1.1. Summary of literature survey about clinical - experimental studies

| **Title of the Study** | **Author(s)** | **Year** | **Flow Profile** | **Stenosis Severity** | **Stenosis Shape** |
|---|---|---|---|---|---|
| Phonoangiography: a new noninvasive diagnostic method for studying arterial disease [10] | Lees, R. S. & Dewey, C. F. | 1970 | Pulsatile | Random patient specific data | Random patient specific data |
| Experimental measurement of turbulence spectra distal to stenosis [18] | Kim, B. M. & Corcoran, W. H. | 1974 | Non-pulsatile | 30%, 55%, 75%, 89%, 98% | Blunt |
| Evaluation of carotid stenosis by phonoangiography [17] | Duncan, G. W. et al. | 1975 | Pulsatile | Random patient specific data | Random patient specific data |
| Turbulent velocity measurements in a model of aortic stenosis [19] | Clark, C. | 1976 | Pulsatile | 75%, 89%, %93.75 | Circular, triangular, rectangular |
| Turbulent wall pressure measurements in a model of aortic stenosis [20] | Clark, C. | 1977 | Pulsatile | 75%, 89%, %93.75 | Circular, triangular, rectangular |
| Wall pressure spectra scaling downstream of stenoses in steady tube flow [21] | Tobin, R. J. & Chang, I. | 1976 | Non-pulsatile | 75%, 85%, 90%, 95% | Blunt |
| Origin and character of vascular murmurs: Model studies [22] | Fredberg, J. J. | 1977 | Non-pulsatile | 55%, 64%, 72%, 82%, 91% | Elliptical |
| Wall vibrations induced by flow through simulated stenoses in models and arteries [23] | Kirkeeide, R. L. et al. | 1977 | Non-pulsatile | 57.7%, 61.1%, 73.5%, 75.8%, 89.5%, 90.3% | Blunt |

| | | | | | |
|---|---|---|---|---|---|
| The bruit of carotid stenosis versus radiated basal heart murmurs [24] | Kistler, J. P. et al. | 1977 | Pulsatile | Random patient specific data | Random patient specific data |
| Spectral analysis of arterial bruits (phonoangiography): Experimental validation [25] | Miller, A. et al. | 1980 | Pulsatile | Classified as least, mild, most severe without numerical values | Blunt |
| Intravascular pressure and velocity fluctuations in pulmonic arterial stenosis [27] | Lu, P. C. et al. | 1980 | Pulsatile | 40%, 60%, 77.5% | Blunt |
| Quantitative carotid phonoangiography [26] | Knox, R. | 1981 | Pulsatile | Random patient specific data | Random patient specific data |
| A model investigation of the velocity and pressure spectra in vascular murmurs [28] | Lu, P. C. et al. | 1983 | Non-pulsatile | 89% | Converging nozzle |
| Analysis of break frequencies downstream of a constriction in a cylindrical tube [29] | Jones, S. A. & Fronek, A. | 1987 | Non-pulsatile | 56%, 66%, 75%, 83%, 89% | Trapezoidal |
| Modeling of noise generation by a vascular stenosis [31] | Borisyuk, A. O. | 2002 | Non-pulsatile | 34%, 61% | Blunt |
| Experimental study of wall pressure fluctuations in a pipe behind a stenosis [32] | Borisyuk, A. O. | 2003 | Non-pulsatile | 56%, 75%, 89% | Blunt |
| Experimental study of wall pressure fluctuations in a pipe behind a cylindrical insertion with eccentricity [33] | Borisyuk, A. O. | 2004 | Non-pulsatile | 69%, 75% | Axisymmetric and eccentric blunt |

| | | | | | |
|---|---|---|---|---|---|
| Acoustic radiation from a fluid-filled, subsurface vascular tube with internal turbulent flow due to a constriction [35] | Yazıcıoğlu Y. | 2005 | Non-pulsatile | 87% | Blunt |

Table 1.2. Summary of literature survey about numerical studies

| Title of the Study | Author(s) | Year | Flow Profile | Stenosis Severity | Stenosis Shape |
|---|---|---|---|---|---|
| Application of large-eddy simulation to the study of pulsatile flow in a modeled arterial stenosis [36] | Mittal, R. et al. | 2001 | Pulsatile | 50% | Circular |
| Numerical study of pulsatile flow in a constricted channel [37] | Mittal, R. et al. | 2003 | Pulsatile | 50% | Circular |
| Direct numerical simulation of stenotic flows. Part 1. Steady flow [39] | Varghese, S. S. et al. | 2007 | Non-pulsatile | 75% | Axisymmetric and eccentric elliptical |
| Direct numerical simulation of stenotic flows. Part 2. Pulsatile flow [40] | Varghese, S. S. et al. | 2007 | Pulsatile | 75% | Axisymmetric and eccentric elliptical |
| Large–Eddy simulation of pulsatile blood flow [41] | Paul, M. C. et al. | 2009 | Pulsatile | 50% | Elliptical |
| LES of additive and non-additive pulsatile flows in a model arterial stenosis [58] | Molla, M. M. et al. | 2010 | Pulsatile | 50% | Elliptical |
| Direct numerical simulation ofphysiological pulsatile flow through a stenotic channel [42] | Khair, A. et al. | 2011 | Pulsatile | 60%, 70% | Elliptical |
| Investigation of physiological pulsatile flow in a model arterial stenosis using large-eddy and direct numerical simulations [59] | Paul M. C. & Molla, M. M. | 2012 | Pulsatile | 50% | Elliptical |

| | | | | | |
|---|---|---|---|---|---|
| A coupled flow-acoustic computational study of bruits from a modeled stenosed artery [44] | Seo, J. H. & Mittal R. | 2012 | Non-pulsatile | 50%, 75% | Elliptical |
| Computational analysis of high frequency fluid–structure interactions in constricted flow [47] | Salman, H. E. et al. | 2013 | Non-pulsatile | 87% | Blunt |
| Investigation of on skin surface response due to acoustic radiation from stenosed blood vessels [48] | Salman, H. E. & Yazıcıoğlu, Y. | 2015 | Non-pulsatile | 50%, 70%, 90%, 95% | Blunt |
| Large Eddy Simulation of pulsatile flow through a channel with double constriction [49] | Molla, M. M. & Paul, M. C. | 2017 | Pulsatile | 50% | Consecutive |
| A computational method for analyzing the biomechanics of arterial bruits [45] | Zhu, S. et al. | 2017 | Non-pulsatile | 75% | Elliptical |
| A method for the computational modeling of the physics of heart murmurs [46] | Seo, J. H. et al. | 2017 | Non-pulsatile | 75% | Low slope |
| Flow-induced vibration analysis of constricted artery models with surrounding soft tissue [49] | Salman, H. E. & Yazıcıoğlu, Y. | 2017 | Non-pulsatile | 50%, 70%, 90%, 95% | Blunt |
| Numerical investigation of wall pressure fluctuations downstream of ideal and realistic stenosed vessel models [50] | Özden, K. et al. | 2018 | Pulsatile | 87% | Axisymmetric and eccentric elliptical |

## 1.4 Motivation and Outline

As mentioned in the previous sections, there are several disadvantages of the techniques used to diagnose stenosed vessels such as: being invasive, expensive and time-consuming, not to be applied to people with certain diseases, being prone to misleading results due to dependency of physician or technician skills. In order to overcome this deficiency, phonoangiography studies have been carried out. However, this method is especially ineffective in detecting the stenoses that cause low frequency murmurs. Moreover, clinical efficacy data has not yet been published using the latest AD systems. For these reasons, further studies are needed at the point of developing acoustic based non-invasive diagnostic methods. Main motivation of this study is to gain a better insight about the acoustic emission caused by turbulent pressure fluctuations at the post-stenotic region. Although there are many theoretical, numerical and experimental studies related to this topic in the literature, a deficiency has been identified at the point of examining the effect of the severity of stenosis and various morphological parameters related to stenosis on the sound emerging from stenosed arteries. This numerical study is conducted with the motivation of making a contribution to the non-invasive diagnosis in this aspect. For this purpose, flow field, turbulent wall pressure fluctuations and associated acoustic emission in the post-stenosis region are investigated by means of simulations performed with the LES model.

Outline of the thesis is as follows:

In Chapter 2, after a summary of computational fluid dynamics (CFD) applications in the field of cardiovascular biomechanics, modeling of blood flow in stenotic vessels is briefly explained. Later, details of space and time discretization schemes and pimpleFoam solver of OpenFOAM open source code employed in the simulations are given.

In Chapter 3, simulations are carried out under constant flow conditions by using axisymmetric and eccentric blunt stenosis geometries. Wall pressure fluctuations

after stenosis are investigated and the results obtained are compared with the theoretical and experimental results in the literature.

In Chapter 4, simulations are performed at physiological pulsatile flow conditions using axisymmetric and elliptic stenosis models with 5 different stenosis severities in a range of 50% and 95%. By this way, the effect of stenosis severity and eccentricity on the characteristics of the sound emerging from the stenosed vessel is examined.

In Chapter 5, the effect of different stenosis shapes on the wall pressure fluctuations and the emitted sound from stenosed vessels is investigated under physiological pulsatile flow conditions.

In Chapter 6, the results and interpretations of the present study are summarized and future work recommendations that can be realized by improving this study are presented.

# CHAPTER 2

# NUMERICAL METHODS

## 2.1 Applications of CFD in Cardiovascular Biomechanics

CFD is an area of mechanical engineering used to analyze fluid flow, heat transfer and related phenomena with computer-based simulations. The CFD technique, initially used in a limited number of high-tech fields, is now being used to solve complex problems in many modern engineering fields such as: lift and drag calculation in aerodynamics of aircrafts, combustion in internal combustion engines and gas turbines, cooling of equipment including microcircuits, heating/ventilation, flows in rivers and oceans, weather prediction and blood flow through arteries [58, 59].

CFD is still emerging in the field of biomechanics. The reason why the use of CFD in the biomechanical field is behind other fields is that the anatomy of the human body and behaviour of the fluids in the body are extremely complex. CFD has become a popular method for understanding the fluid flow phenomena in the cardiovascular system of the human body. Nowadays there are software packages like SimVascular [60] and CRIMSON [61] providing a complete pipeline from medical image data segmentation to patient specific blood flow simulation and analysis. This is because of the four main benefits of numerical simulations of circulatory functions. CFD:

- delivers a good understanding of the causes and consequences of the pathologies developing in the cardiovascular system (e.g. heart failure, atherosclerosis and aneurysm)
- assists to develop patient specific surgical planning
- predicts post-operative complications and reduces the risks associated with these undesirable conditions
- assists in more effective development of medical devices and prostheses related to the cardiovascular system (e.g. ventricular assist device, artificial heart valve and stent).

Despite its many advantages, the inherent limitations of applying CFD should be considered:

- Numerical errors occur during computations; therefore, there will be differences between the computed results and reality.
- The results of the simulations conducted in cardiovascular biomechanics need to be interpreted carefully with specialists in order to make the findings reliable and applicable by the clinical community. To this end, medical educations should be promoted to integrate simulation results into the tools clinicians use in decision making stage [62].
- For CFD applications it is unclear how detailed the clinical data needs to be in terms of geometry (segmented from medical images) and parameterisation (variability described by the model and the tuning of patient-specific boundary conditions). Continuing improvements in imaging, image-registration and segmentation algorithms will augment accuracy [63].
- Further understanding of the relative importance of physiological parameters is required to determine those which are most influential, and those which can be assumed or averaged during CFD simulations [64].

## 2.2 Modeling of Blood Flow in Stenosed Arteries

It is required to understand the physics of blood flow in stenosed arteries in order to deal with wall pressure fluctuations and sound generation due to post-stenotic turbulence. In this section, first physics of flow in stenosed arteries will be explained and then the governing equations to solve this flow will be given. Finally, computational method chosen to deal with this problem will be presented.

### 2.2.1 Flow in Stenosed Arteries

During systole phase, blood undergoes rapid convective acceleration as it passes from the unstenosed portion of the artery through converging section of the stenosis. The flow passing through the diverging section of the stenosis separates from the walls due to its inability to overcome the adverse pressure gradient. At the boundary between the high-velocity-separated jet and the slower moving fluid in the recirculating separation zone, a shear layer is created which is susceptible to fluid-dynamical instabilities. The shear layer provides a source from which these instabilities extract energy from the mean flow.

This energy extraction process proceeds at a sufficiently rapid rate that before systole has ended the instabilities break down into fully turbulent motion if the jet $Re$ is high enough, $Re_{jet} = u_{jet}d/\nu$ where $u_{jet}$ is the jet velocity, $d$ is the diameter of the stenosis throat and $\nu$ is the kinematic viscosity of blood. The turbulence continues to extract energy from the mean flow as the jet expands to fill the artery. Once the jet fills the artery, the turbulence is no longer able to sustain itself by extraction of energy from the mean flow. Because the unobstructed arterial Reynolds number, $Re = Re_{jet}(d/D)$ where $D$ is the unstenosed vessel diameter, is typically below the critical Re necessary to achieve sustained turbulent flow in a straight pipe. At this point processes for dissipation predominate over those for production of turbulent energy.

Between the stenosis and the region where turbulence has significantly decayed, the turbulent intensities can be quite large, and the wall of the artery can be subjected to pressure fluctuations imposed by the turbulent flow. These fluctuations interact with the vessel wall and result in murmurs that radiate outwards through the surrounding tissue. This emission can be evaluated as a sign of stenosis. Schematic representation of the mechanism showing the production of sound by post-stenotic turbulence is given in Figure 2.1.

The main descriptor of turbulent wall pressure fluctuation is the root mean square (RMS) of pressure fluctuations, $p'_{RMS}$. The frequency analysis of pressure fluctuations at the post-stenotic region is used to determine the transformation of acoustic energy from a turbulent flow. The frequency spectrum of the pressure fluctuations, $E_{pp}(f)$, represents the contributions from each eddy sizes to the total energy.

$$p'_{RMS} = \langle p'^2(t) \rangle^{1/2} = \left( \frac{1}{T} \int_0^T p'^2(t)\, dt \right)^{1/2} \tag{2.1}$$

$$E_{pp}(f) = \frac{{p'_{RMS}}^2}{\Delta f} \tag{2.2}$$

where $T$ is the averaging time, $f$ is the frequency and $\Delta f$ is the unit frequency interval.

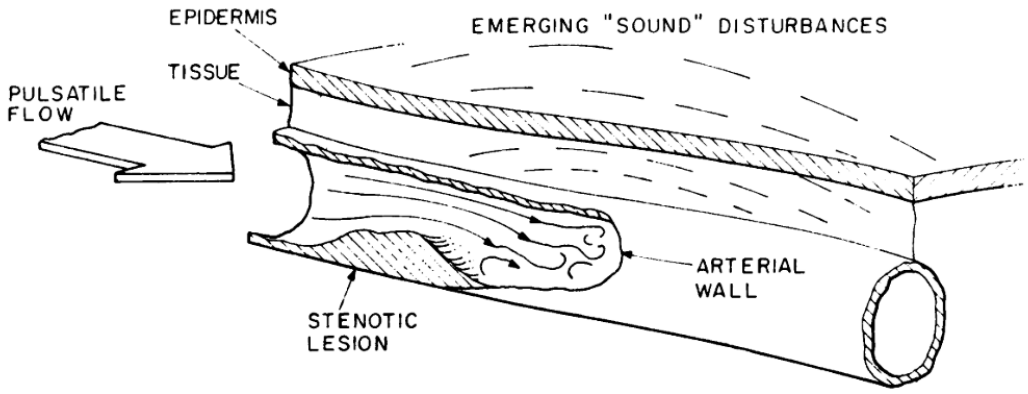


Figure 2.1. Schematic representation of sound generation due to post-stenotic turbulence in a stenosed artery and emission of the sound to the skin surface [10]

### 2.2.1 Governing Equations

Blood flow through the arteries can be modelled entirely using Navier-Stokes equation of motion [65]. Therefore, the governing equations for blood flow can be written as the continuity equation,

$$\frac{\partial u_j}{\partial x_j} = 0 \tag{2.3}$$

and the momentum equations,

$$\frac{\partial u_i}{\partial t} + \frac{\partial u_i u_j}{\partial x_j} = -\frac{1}{\rho}\frac{\partial p}{\partial x_i} + \frac{\partial t_{ij}}{\partial x_j} \tag{2.4}$$

where $x_j$ is the coordinate system and $u_j$ are the corresponding velocity components, $p$ is the pressure, $\rho$ is the density and $t_{ij}$ is the viscous stress tensor. It should be noted that these equations are used to define both incompressible laminar and turbulent flows. Whereas laminar flows are stable, turbulent flows are chaotic, diffusive, time-dependent, and involve rapid mixing with 3D vorticity fluctuations with a broad range of time and length scales [66]. The instable nature

of turbulence is caused by the amplification of the perturbations due to the highly non-linear inertial terms. Several approaches are used for numerical analysis of turbulent flows. These methodologies can be classified as: Reynolds averaged Navier-Stokes (RANS) based turbulence models (e.g. $k-\omega$ and $k-\varepsilon$ models), LES models (e.g. Smagorinsky-Lilly and dynamic SGS model), detached eddy simulation (DES) and DNS.

### 2.2.2 Evaluation of Simulation Approaches for Turbulent Flows

The performance of approaches used for the solution of turbulent flows in stenotic vessels has been evaluated in many studies in the literature. Varghese and Frankel [67], Lee et al. [68, 69] and Li et al. [70] studied 2D laminar-turbulent transitional flows passing an arterial stenosis using RANS approach based on the two-equation turbulence models. Scotti and Piomelli [71] later indicated that the RANS turbulence models have some limitations in modeling pulsatile flows where the inlet velocity profile and pressure gradient oscillate with time. They found that although the RANS models gave good predictions on the mean velocity profiles, their predictions of the key turbulence statistics such as the Reynolds shear stresses, turbulent kinetic energy and dissipation rate were unsatisfactory. Moreover, these RANS models are not capable of simulating instantaneous changes during pulsatile turbulent flows as the governing equations of the RANS approach are ensemble-averaged.

Recently, Scotti and Piomelli [72] conducted DNS and LES of a pulsatile turbulent channel flow subjected to an unsteady pressure gradient. Both techniques result in simulations that can capture unsteady scale-dependent vortex dynamics, transition, and turbulence.

Varghese et al. examined a number of two-equation turbulence modelsfor their potential to predict flow through an eccentric stenosis model by [73]. The results clearly illustrated their inadequacy to model this type of three-dimensional flow

even at non-pulsatile flow conditions. LES results has indicated that this approach may offer a more promising route toward accurately predicting transitional stenotic flows.

Tan et al. [74] investigated LES and RANS approaches to predict transitional flows in 75% stenosed axisymmetric and eccentric models. The results are compared with previously published experimental and DNS studies. This study demonstrated the power of LES methods when compared with the RANS approach. LES with dynamic Smagorinsky appeared to be close to DNS in replicating the axisymmetric experimental results. For the eccentric stenosis, LES with Smagorinsky coefficient of 0.13 gave the closest agreement with DNS despite the known shortcomings of fixed coefficients.

Pal et al. performed LES by using the axisymmetric and eccentric stenosis models of Varghese et al. [39] with non-pulsatile inflow conditions at a Reynolds number of 1000. The purpose of this study was to evaluate different subgrid-scale models for LES. It is concluded that the classical constant coefficient Smagorinsky model gives best agreement with the DNS data, whereas the Vreman and Sigma models predict an early transition to turbulence in the post-stenotic region. The most recent studies of Paul et al. [41], Molla et al. [75] and Mittal et al. [37] showed that LES could be an ideal simulation technique for studying the transition of the pulsatile flow. All these investigation showed that LES is a preferable alternative to DNS and RANS approaches in terms of accuracy and computational expense. For this reason LES is used in the simulations of the current study.

## 2.3 Large Eddy Simulation (LES)

### 2.3.1 Spatial Filtering of Governing Equations

Turbulent flows contain a wide range of eddy sizes. The large scale motions are generally much more energetic than the small scale ones; their size and strength

make them responsible for most of the turbulent fluctuations. A spatial filtering is applied to the governing equations (2.3-2.4) to separate the large (resolved) scale flow field from the smaller (sub-grid) scale.

If $g(x_j, t)$ is a generic variable, its corresponding filtered variable, also known as the resolvable component of $g$, is denoted by $\bar{g}(x_j, t)$. It is defined as the convolution of $g(x_j, t)$ with a filter function $G$, establishing the scale of the resolved eddies, as [76]

$$\bar{g}(x_j, t) = \int_Z g(x_j', t) G\left(x_j - x_j', \Delta(x_j)\right) dx_j' \tag{2.5}$$

where $Z$ is the flow domain and $\Delta(x_j)$ is the filter width. The filter width can be explained as a measure that determines which size of the eddies are classified as small and which are classified as large. Mostly, the filter width is selected to be of the same order as the mesh size. In three-dimension, the filter width is usually taken in LES practice as

$$\Delta(x_j) = \sqrt[3]{\Delta x \Delta y \Delta z} \tag{2.6}$$

where $\Delta x, \Delta y$ and $\Delta z$ are length, width and height of grid cells, respectively. The filter function, $G$, determines the size and structure of the smallest resolvable eddies. The most common filter functions used in three dimensional LES computations are as following. The top-hat or box filter,

$$G\left(x_j - x_j', \Delta(x_j)\right) = \begin{cases} \dfrac{1}{\Delta(x_j)^3} & if \quad \left|x_j - x_j'\right| \le \dfrac{\Delta(x_j)}{2} \\ 0 & otherwise \end{cases} \tag{2.7}$$

The top-hat filter is used in finite volume implementations of LES [77] because it suits naturally into finite volume formulation [78]. After the filtering operation, the Navier-Stokes equations for LES are obtained as follows

$$\frac{\partial \bar{u}_j}{\partial x_j} = 0 \tag{2.8}$$

$$\frac{\partial \bar{u}_i}{\partial t} + \frac{\partial \bar{u}_i \bar{u}_j}{\partial x_j} = -\frac{1}{\rho}\frac{\partial \bar{p}}{\partial x_i} + \frac{\partial}{\partial x_j}\left[\nu(|\dot{\gamma}|)\left(\frac{\partial \bar{u}_i}{\partial x_j} + \frac{\partial \bar{u}_j}{\partial x_i}\right)\right] - \frac{\partial \tau_{ij}}{\partial x_j} \tag{2.9}$$

where $\nu(|\dot{\gamma}|)$, the non-Newtonian blood viscosity, depends on the shear rate and $\tau_{ij}$ is the subgrid-scale stress term, used to model the effects of the small scales, as

$$\tau_{ij} = \overline{u_i u_j} - \bar{u}_i \bar{u}_j \tag{2.10}$$

During spatial filtering, information related to the smaller, filtered-out turbulent eddies is destroyed. This, and interaction effects between the larger resolved eddies and the smaller unresolved ones, gives rise to sub-grid-scale (SGS) stresses defined in equation (2.10). Their effect on the resolved flow must be described by means of an SGS model. Among these models Smagorinsky-Lilly SGS and Germano-Lilly dynamic SGS models will be discussed in the following sections.

### 2.3.2 Smagorinsky-Lilly SGS Model

The model is first proposed by Smagorinsky [79] based on the eddy viscosity assumption as

$$\tau_{ij} - \frac{1}{3}\delta_{ij}\tau_{kk} = -2\nu_{sgs}\bar{S}_{ij} \tag{2.11}$$

where $\nu_{sgs}$ is the subgrid kinematic eddy viscosity and obtained by the assumption that the turbulent dissipation is equal to the turbulent energy production with the expression

$$\nu_{sgs} = (C_s\Delta)^2|\bar{S}| \tag{2.12}$$

where $C_s$ is the Smagorinsky constant and $|\bar{S}| = \sqrt{2\bar{S}_{ij}\bar{S}_{ij}}$ is the magnitude of the rate of strain tensor defined as $\bar{S}_{ij} = {}^1\!/_2\left(\frac{\partial \bar{u}_i}{\partial x_j} + \frac{\partial \bar{u}_j}{\partial x_i}\right)$. Hence the Smagorinsky-Lilly model takes the form

$$\tau_{ij} - \frac{1}{3}\delta_{ij}\tau_{kk} = -2(C_s\Delta)^2|\bar{S}|\bar{S}_{ij} = -2{C_s}^2\beta_{ij} \tag{2.13}$$

where $\beta_{ij} = \Delta^2|\bar{S}|\bar{S}_{ij}$. The value of $C_s$ is usually taken as 0.1 in the literature. However, this approach is not suitable for transition-to-turbulent flows in which $C_s$ varies inside the flow domain. Therefore, the model needs an improvement to determine the value of $C_s$ for transitional flows which will be discussed in the next section.

### 2.3.3 Germano-Lilly Dynamic SGS Model

The dynamic subgrid-scale model is originally proposed by Germano et al. [77] in which the Smagorinsky constant is calculated as a function of time and position. According to the model, a test-filter having a larger width than the original filter, ($\widetilde{\Delta} > \Delta$), is applied to the filtered Navier-Stokes equations (2.8-2.9) leading to the subgrid scale stress tensor, $T_{ij}$, similar to $\tau_{ij}$ as

$$T_{ij} = \widetilde{\overline{u_i u_j}} - \widetilde{\bar{u}_i}\widetilde{\bar{u}_j} \tag{2.14}$$

where the two stress relations (2.10, 2.14) are in relation through the following Germano identity,

$$L_{ij} = T_{ij} - \widetilde{\tau_{ij}} \tag{2.15}$$

Assuming the same functional form as the Smagorinsky model, the deviatoric part of $T_{ij}$ gives

$$T_{ij} - \frac{1}{3}\delta_{ij}T_{kk} = -2\left(C_s\widetilde{\Delta}\right)^2|\widetilde{\bar{S}}|\widetilde{\bar{S}_{ij}} = -2{C_s}^2\alpha_{ij} \tag{2.16}$$

with the test-scale defined similarly to those for the grid scale where $\alpha_{ij} = \left(\widetilde{\Delta}\right)^2|\widetilde{\bar{S}}|\widetilde{\bar{S}_{ij}}$.

The elements of $L_{ij}$ in equation (2.15) are the resolved components of the stress tensor associated with the test and grid scales of motion. If equation (2.13) is subtracted from equation (2.16) right hand side of equation (2.15) can be calculated as

$${L_{ij}}^a = L_{ij} - \frac{1}{3}\delta_{ij}L_{kk} = 2{C_s}^2M_{ij} = 2{C_s}^2(\beta_{ij} - \alpha_{ij}) \tag{2.17}$$

where

$$M_{ij} = \beta_{ij} - \alpha_{ij} \tag{2.18}$$

By means of a least square approach proposed by Lilly, local values of Smagorinsky coefficient $C_s$ is calculated iteratively:

$${C_s}^2 = \frac{1}{2}\frac{{L_{ij}}^a M_{ij}}{{M_{ij}}^2} \tag{2.19}$$

and set to zero when it is negative.

In this thesis, dynamic SGS model [77] is used.

### 2.4 Finite Volume Discretization and OpenFOAM

The purpose of any discretization method is to transform one or more partial differential equations (PDEs) into a system of algebraic equations. The open source flow solver OpenFOAM uses finite volume method (FVM) for the discretization of PDEs. FVM is based on the division of the computational domain into many

small non-intersecting control volumes (CVs) called cells. In OpenFOAM all the necessary variables about flow field are stored at the center of these cells and the value of the variable at the centroid represents the whole cell.

### 2.4.1 Finite Volume Discretization

The procedure of finite volume discretization can be illustrated by using convection-diffusion form of the standard transport equation for a scalar property $\varphi$:

$$\underbrace{\frac{\partial \varphi}{\partial t}}_{\substack{temporal \\ derivative}} + \underbrace{\nabla.(\boldsymbol{u}\varphi)}_{\substack{convection \\ term}} - \underbrace{\nabla.(\Gamma \nabla \varphi)}_{\substack{diffusion \\ term}} = 0 \tag{2.20}$$

where Γ is the diffusion coefficient. If this equation is integrated over a cell and the Gauss theorem is used to convert volume integrals into surface integrals where applicable one gets

$$\int_t^{t+\Delta t} \left( \frac{\partial}{\partial t} \int_{CV} \varphi d\forall + \oint_{S_{CV}} \varphi \boldsymbol{u} \cdot \boldsymbol{n} \, dS - \oint_{S_{CV}} \Gamma \nabla \varphi \cdot \boldsymbol{n} \, dS \right) dt = 0 \tag{2.21}$$

If equation (2.21) is summed over all the CVs, a conservation of quantity $\varphi$ for the whole domain is satisfied. Consequently, FVM is intrinsically conservative and this is an important reason for preferring FVM in CFD simulations.

In order to get the algebraic equations spatial and temporal discretization should be applied to equation (2.21). It should be noted that the choice of these discretization schemes should be made such that there is a good balance between the accuracy and stability of the results. Before discretization, surface integration parts of the equation is approximated as a sum over the faces of the CV:

$$\oint_{S_{CV}} \varphi \boldsymbol{u} \cdot \boldsymbol{n} \, dS \approx \sum_j (\boldsymbol{u}_j \cdot \boldsymbol{n}) S_j \varphi_j \tag{2.22}$$

$$\oint_{S_{CV}} \Gamma \nabla\varphi \cdot \boldsymbol{n}\, \mathrm{d}S \approx \sum_{j} \left(\nabla_j \varphi \cdot \boldsymbol{n}\right) S_j \Gamma_j \tag{2.23}$$

where index $j$ represents for the value in the centroid of the face of the cell. Note that the values at the face centres are not known which requires the interpolation of values from cell centres to face centres. For this spatial discretization, second order central differencing is applied in this study. This scheme, defined with *linear* keyword in OpenFOAM, is suggested to get improved accuracy for LES calculations even on unstructured meshes [80]. For temporal discretization, second order backward differencing scheme is used in the simulations as

$$\left(\frac{\partial \varphi}{\partial t}\right)^n = \frac{\frac{3}{2}\varphi^n - 2\varphi^{n-1} + \frac{1}{2}\varphi^{n-2}}{\Delta t} \tag{2.24}$$

The scheme uses the unknown values of $\varphi$ from the current time step, $\varphi^n$, and two preceding time steps, $\varphi^{n-1}$ and $\varphi^{n-2}$ where $\Delta t$ is the time step value. This temporal discretization scheme is fully implicit because time integrals of the convective and diffusive terms in equation (2.21) are calculated by the (to be determined) values at the current time-step. The keyword in OpenFOAM used for this scheme is *backward*.

### 2.4.2 pimpleFoam Solver Algorithm

OpenFOAM offers three different pressure-velocity coupling algorithms to solve the governing equations: PISO (Pressure-Implicit with Splitting of Operators); SIMPLE (Semi-Implicit Method for Pressure-Linked Equations); and PIMPLE which is a merged PISO and SIMPLE. In this study the pimpleFOAM solver, the steps of which is shown in Figure 2.2, is used.

At the beginning of each time step, the algorithm increases the current simulation time by the time step value. It should be noted that PIMPLE solver allows automatic time step adjustment to maintain a user provided maximum Courant number ($Co$):

$$Co = \frac{\sum_{i=1}^{n} |\phi_i| \, \Delta t}{\forall} \tag{2.25}$$

where $\Delta t$ is the time step, $\forall$ is the cell volume and $\phi$ is the face volumetric flux which is summed over all cell faces.

Then the pressure-velocity coupling loop is executed. Inside that loop, the momentum equation is solved first named as momentum predictor step, after which the corrector loop is performed. Inside this loop, the Poisson equation for pressure, obtained by combining the divergence of the momentum equation and the continuity equation, is solved. This step is called as the pressure corrector step. In the momentum corrector step, the velocity field is corrected, based on corrected pressure, ensuring it is converged. It is possible to regulate how many times the pressure-velocity coupling cycle will be executed. If this loop is executed only once, then the algorithm works like the PISO method. Similarly, the number of corrector loops can be controlled, and if this loop is performed only once, pimpleFOAM behaves as a transient SIMPLE algorithm. During this study pressure-velocity coupling and corrector loops are executed 2 and 3 times per time step, respectively.

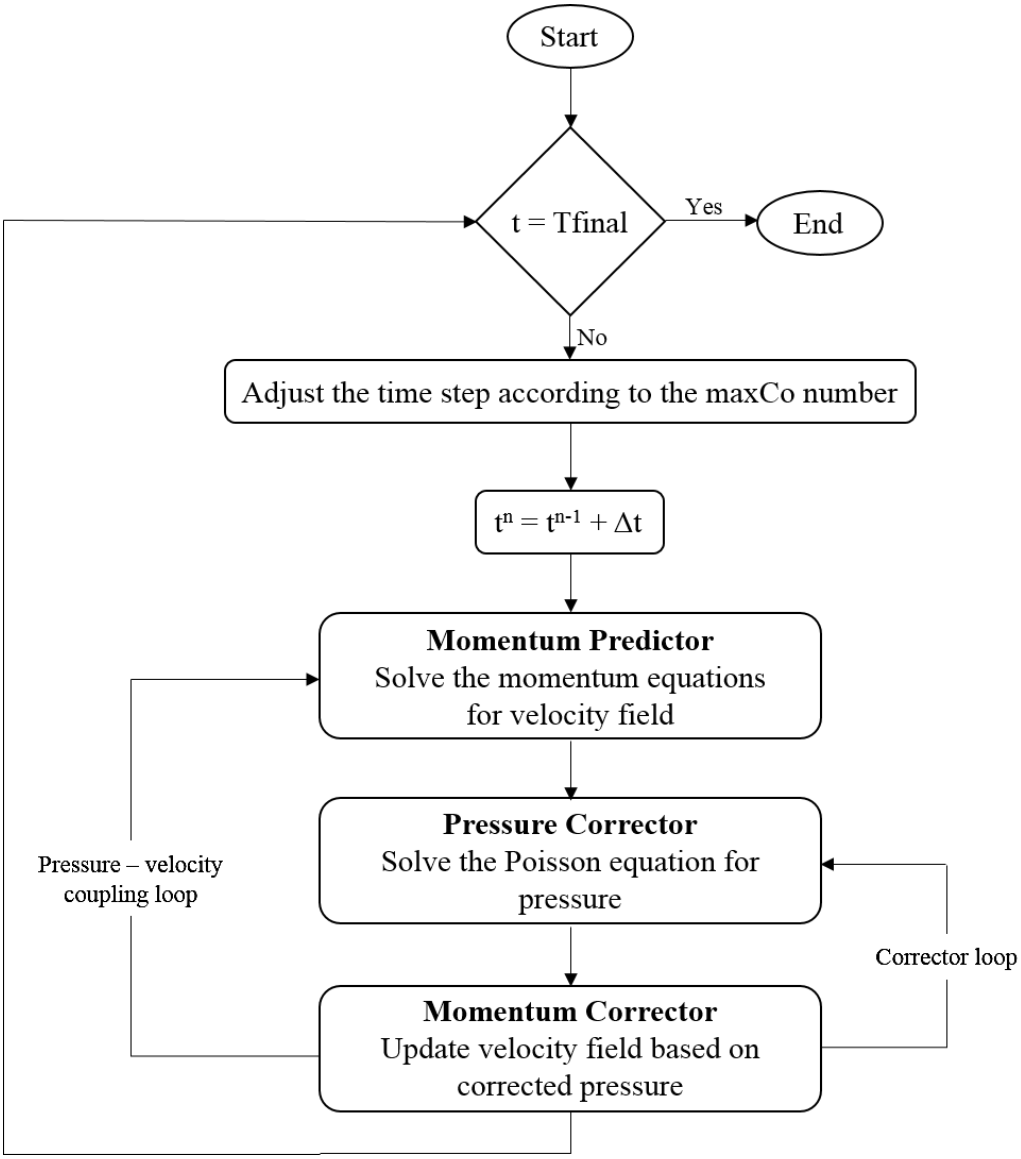


Figure 2.2. Flowchart of the PIMPLE algorithm used in OpenFOAM

# CHAPTER 3

# WALL PRESSURE FLUCTUATIONS DOWNSTREAM OF AXISYMMETRIC AND ECCENTRIC BLUNT STENOSIS MODELS

## 3.1 Introduction

From the beginning of the 1970s to the present day, many studies investigated the flow regime in stenosed blood vessels from different perspectives as can be understood from the literature review. The studies of Yazıcıoğlu et al. [35] and Salman et al. [47] form the basis of this chapter. Yazıcıoğlu et al. studied the vibration of a thin-walled cylindrical, compliant viscoelastic tube with a blunt axisymmetric stenosis [35]. Experimental measurements are compared with empirical correlations of Tobin and Chang [21] with similar trends in terms of amplitude and spatial-spectral distribution of acoustic radiation. As a follow up study, Salman et al. considered the same problem numerically [47]. Although their findings showed good agreement with the reference results in terms of spectral characteristics of wall pressure fluctuations, there was a significant difference in amplitudes. In this chapter of the thesis, flow through an axisymmetric blunt stenosis at $Re$ of 1000 is taken as the basis, and the effects of $Re$ and radial eccentricity are investigated. The main focus here is on the turbulent pressure fluctuations at the post-stenotic region and the acoustic pressure distribution created on the vessel wall.

### 3.2 Computational Model

Three idealized blunt stenoses used in this chapter are given in Figure 3.1. Axisymmetric one is identical with the one used by Yazıcıoğlu et al. [35] and Salman et al. [47]. Eccentric geometries are defined by the following percent eccentricity formula

$$e = \frac{\delta}{D} \times 100 \tag{3.1}$$

where $\delta$ is the vertical shift of the axis of the stenosed section from the main vessel axis and $D$ is the diameter of the non-stenosed vessel. The flow domain has a total length of 150 mm. In all three geometries, the blunt stenosis represents a severe stenosis with a reduction of 87% in flow area.

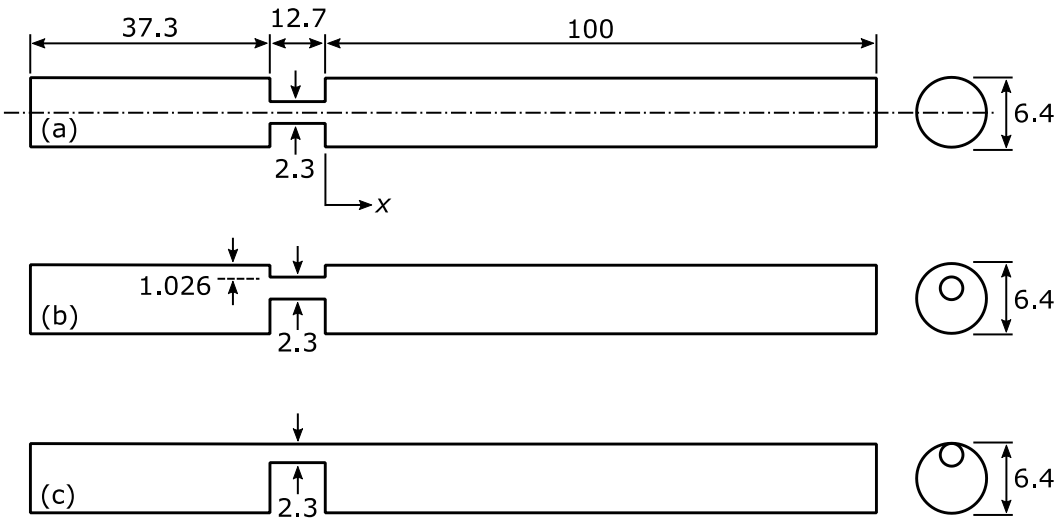


Figure 3.1. Sectional views of flow domains (a) axisymmetric (b) 16% eccentric (c) 32% eccentric. Flow is from left to right. Figure is out of scale and dimensions are in mm.

A typical blood substitute used in in-vitro experiments is water, which is also the working fluid used in this chapter. Density and kinematic viscosity of water are taken as 1000 kg/m$^3$ and $10^{-6}$ m$^2$/s, respectively. In previous studies investigating turbulent pressure fluctuations, $Re$ values are typically used in a range of 500 - 4000. In the current study simulations are performed at $Re$ values of 1000 and 2000, based on the average inlet speed and the vessel diameter. Flow is considered to be non-pulsatile, based on the fact that the frequency of the cardiac cycle is in the order of 1 Hz, whereas the frequencies of the post-stenotic fluctuations are usually in the range of 20 - 1000 Hz. Uniform velocity of 0.15625 m/s for $Re$ = 1000 and 0.3125 m/s for $Re$ = 2000 are specified at the inlet. Low and high $Re$ flows become fully developed at about 2.5$D$ and 5$D$ distance from the inlet, respectively, which shows that the length of the domain from the inlet to the stenosis is enough to get fully developed profiles. Reference pressure at the outlet is set to zero and the no slip boundary condition is used at the wall boundaries, which are taken to be rigid.

Dynamic Smagorinsky model is used for LES simulations and governing equations are discretized in space and time using aforementioned schemes. As stated before, selection of pimpleFOAM solver leads to the ability of automatic time step control according to the maximum $Co$. To understand the dependency of the solutions on the time step, preliminary simulations are done with three different maximum $Co$ values of 0.25, 0.5 and 1. Results are compared in terms of mean and fluctuating wall pressures and limiting $Co$ at 1 is found to be satisfactory. With this selection, maximum time step is kept below 2.5x10$^{-6}$ s throughout the simulations.

Four different meshes, details of which are given in Table 3.1, are used to select a suitable mesh. They are obtained by specifying different maximum cell size limits in 5 different regions shown in Figure 3.2. In all these meshes 13 layers of structured prism cells are used close to the walls with a first layer height of 0.003 mm and a growth rate of 1.3. These values are selected after a series of preliminary runs to ensure $y^+ < 1$ at the walls. Tetrahedral cells are used away from the walls.

Mesh independence is checked with the mean wall pressure variation shown in Figure 3.3, as well as the acoustic pressure distribution obtained by using wall pressure fluctuations in Figure 3.4 and frequency contents of the acoustic pressures at $x$ = 10 mm in Figure 3.5. After all these checks, Mesh 3 is evaluated to be suitable and used to obtain the final results.

Table 3.1. Maximum cell size limits specified in different regions and the total number of cells used ($y^+$ < 1 for all meshes)

| | **$R_1$** | **$R_2$** | **$R_3$** | **$R_4$** | **$R_5$** | **# of Cells** |
|---|---|---|---|---|---|---|
| **Mesh 1** | 1.2 mm | 0.6 mm | 0.8 mm | 1.2 mm | 1.6 mm | 171204 |
| **Mesh 2** | 0.6 mm | 0.3 mm | 0.4 mm | 0.6 mm | 0.8 mm | 775369 |
| **Mesh 3** | 0.45 mm | 0.225 mm | 0.3 mm | 0.45 mm | 0.6 mm | 1501082 |
| **Mesh 4** | 0.3 mm | 0.15 mm | 0.2 mm | 0.3 mm | 0.4 mm | 3906271 |

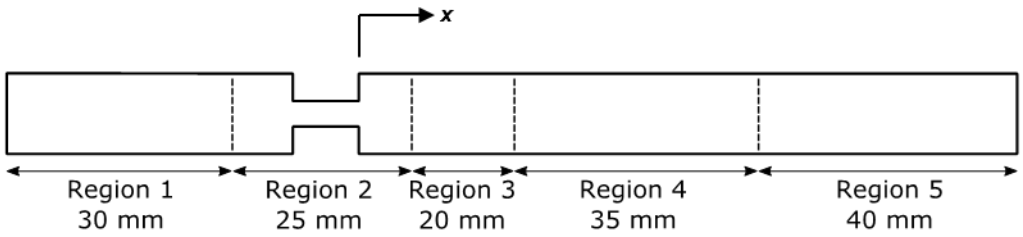


Figure 3.2. Five regions used for mesh generation

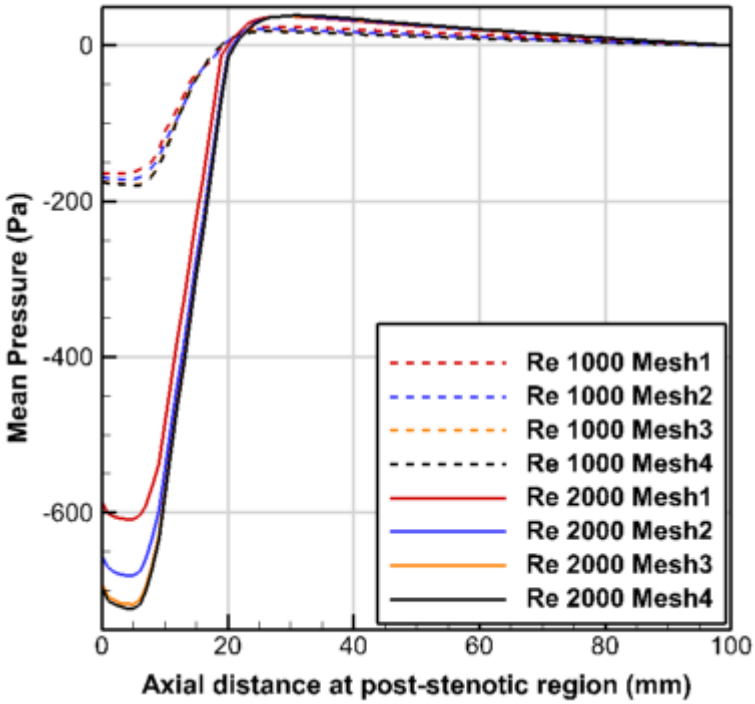


Figure 3.3. Mean wall pressures for axisymmetric models obtained with four different meshes

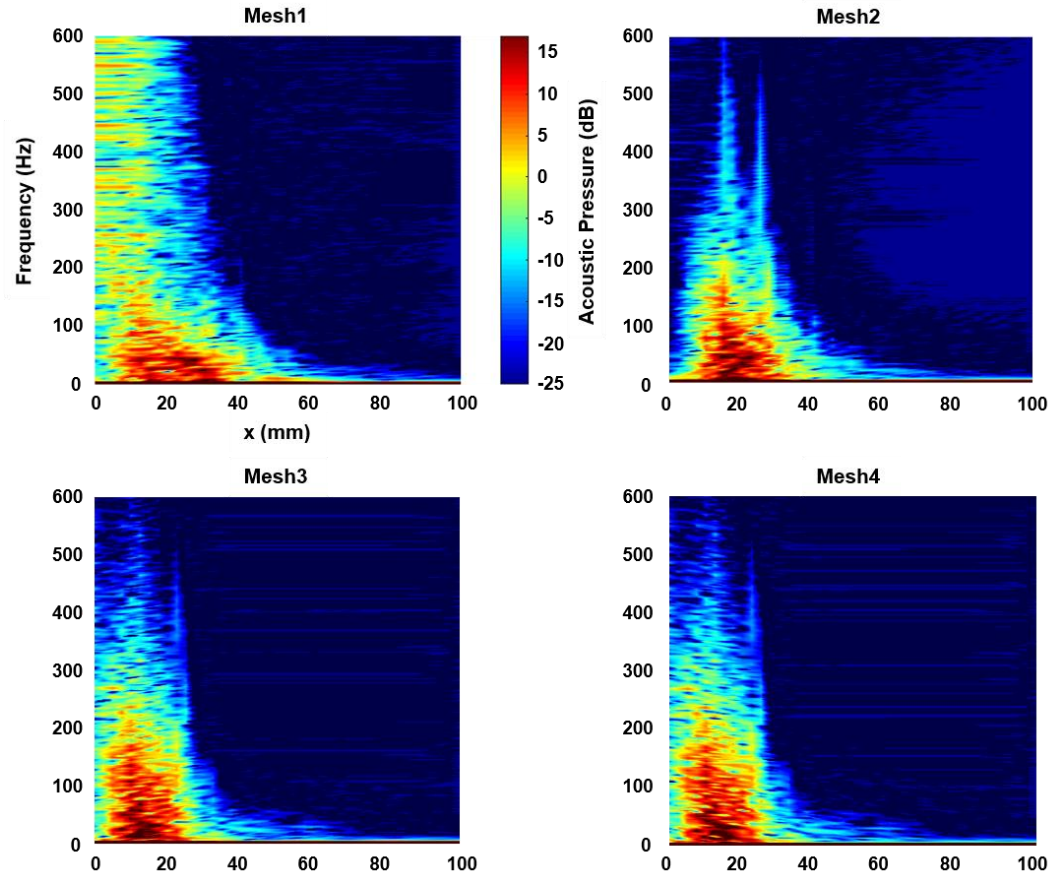


Figure 3.4. Acoustic pressure contours for the axisymmetric model obtained with four different meshes at $Re$ = 1000

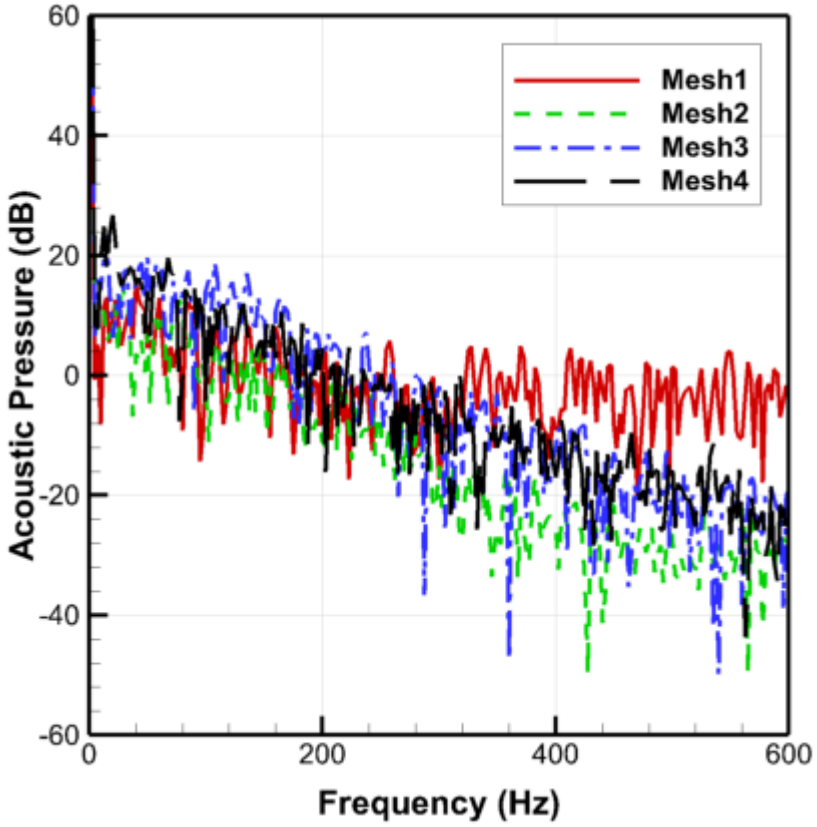


Figure 3.5. Frequency contents of the acoustic pressures for the axisymmetric model at $x$ = 10 mm obtained with four different meshes at $Re$ = 1000

The suitability of this selected mesh for the LES simulations is further checked by calculating the ratio of the cell sizes to the Kolmogorov length scale

$$\eta = \left(\frac{\nu^3}{\varepsilon}\right)^{1/4} \tag{3.2}$$

where $\varepsilon$ is the average rate of dissipation of turbulence kinetic energy per unit mass and $\nu$ is the kinematic viscosity of the fluid. The minimum Kolmogorov length scale is calculated in the simulations conducted with Mesh 3 as 0.0194 mm, 0.00957 mm, 0.0128 mm and 0.0104 mm for the axisymmetric $Re$ = 1000 and 2000, and eccentric 16% and 32% cases, respectively. In all these simulations, the

minimum Kolmogorov length scale is obtained in zone 3 of the mesh, for which the maximum cell size is 0.225 mm. Therefore, the ratio of cell size to the Kolmogorov length scale is kept below 22 in all simulations. This value agrees with the maximum allowable values of 20 and 40 given by Çelik et al. for fine grids and coarse grids, respectively [81].

There are two other metrics for the evaluation of the suitability of computational meshes to perform LES. The first one is expressed as the ratio of the subgrid scale turbulent kinetic energy to the total kinetic energy and called as $LES\_M$. It is determined that all the energy in the kinetic energy spectrum is modelled if this value is 1 and in case of 0, the energy be resolved with LES [82].

$$LES\_M = \frac{TKE_{sgs}}{TKE_{sgs} + TKE_{res}} \tag{3.3}$$

where $TKE_{sgs}$ is the subgrid scale turbulent kinetic energy and $TKE_{res}$ is the resolved kinetic energy. The highest $LES\_M$ value at the post-stenotic region is found as 0.095, which is reasonable for LES, for the axisymmetric Re = 2000 case which has the most intense TKE activity among the models examined in this chapter.

Another metric used in the literature to check the LES resolution is the $LES\_IQ$ proposed by Çelik et al. [83] as follows

$$LES\_IQ = \frac{1}{1 + \alpha_\upsilon \left(\frac{\upsilon_{eff}}{\upsilon}\right)^n} \tag{3.4}$$

where $\upsilon_{eff}$ is the effective kinematic viscosity, $\alpha_\upsilon = 0.05$ and $n = 0.53$. An $LES\_IQ$ value greater than 0.80 is considered as a good LES and that above 0.95 is considered as DNS. The lowest $LES\_IQ$ value at the post-stenotic region of the examined models is found as 0.844, which corresponds to a good LES solution according to the aforementioned scale.

The simulations conducted with this mesh took almost 12, 25, 15 and 17 wall clock days to reach steady-state in terms of mean flow parameters on 24 cores of the TRUBA HPC system of TÜBİTAK ULAKBİM High Performance and Grid Computing Center.

### 3.3 Results and Discussion

To get an overall initial view of the solutions performed in this chapter, instantaneous pressure, axial velocity and vorticity magnitude distributions at the major cross section of the flow domain for axisymmetric and eccentric models are presented in Figure 3.6 and Figure 3.7, respectively. These are the solutions obtained after the mean flow reaches steady state. As seen, stenosis causes a severe pressure drop, which is roughly four times higher for $Re$ = 2000, compared to axisymmetric and eccentric $Re$ = 1000 cases. The axial velocity increases inside the stenosis, forming a jet at the exit and recirculation zones. The maximum velocity magnitude in the flow domain is about 12, 13, 11 and 14 times of the inlet speed for axisymmetric $Re$ = 1000, axisymmetric $Re$ = 2000, 16% eccentric and 32% eccentric cases, respectively. The shear layer around the jet becomes unstable and rolls into vortices at around $x = D$ for the axisymmetric $Re$ = 1000 and $Re$ = 2000 cases, whereas this length extends to $x = 2D$ and $3D$ for 16% and 32% eccentric cases, respectively. Then, these vortices interact with the wall and with each other, breaking into smaller eddies. This interaction is seen as the main source of generation of wall pressure fluctuations [46].

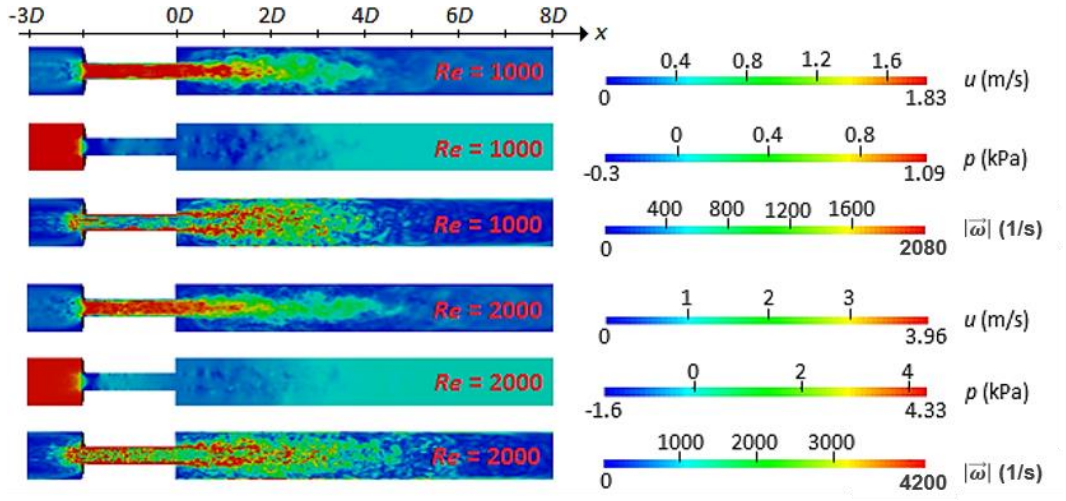


Figure 3.6. Instantaneous axial velocity, pressure and vorticity magnitude contours for axisymmetric model (only a part of the problem domain is shown).

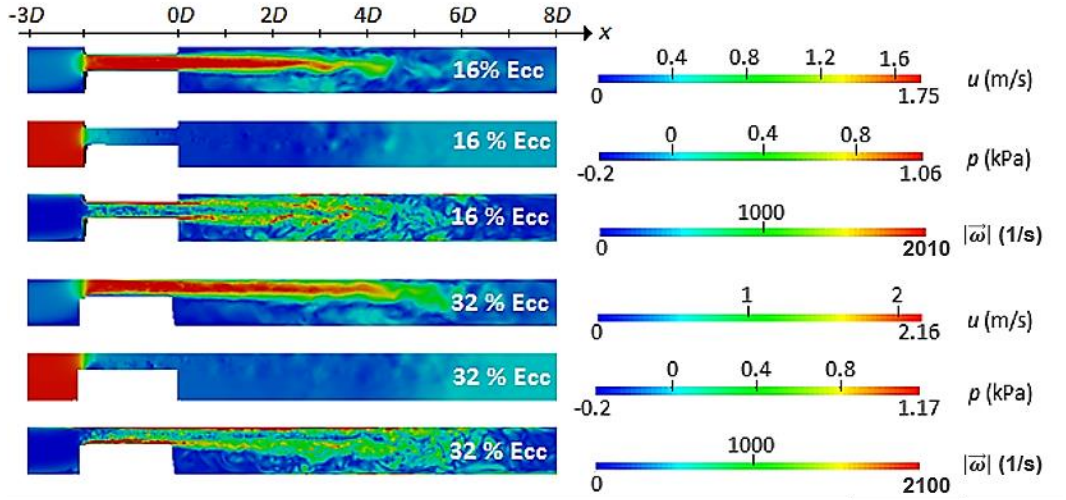


Figure 3.7. Instantaneous axial velocity, pressure and vorticity magnitude contours for eccentric models (only a part of the problem domain is shown).

Vortical structures lose their strength at around $x = 4D$ and $x = 5D$ for the axisymmetric $Re = 1000$ and $Re = 2000$ cases, whereas this length extends to

$x$ = 6$D$ and $x$ = 7$D$ for 16% and 32% eccentric cases, respectively. Therefore, eccentricity is more decisive than Re on the length of the region where vortical structures are effective, which is also the acoustically active region.

Length of the recirculation region is determined to be around 3$D$ for both axisymmetric cases. This is consistent with the measurements of Back and Roschke [84], which were performed on similar blunt stenoses. With eccentricity, lengths of the recirculation regions rise to 4$D$ and 5$D$ for 16% and 32% cases, respectively. According to Figure 3.8, which shows the mean axial velocity profiles, the jet created by the stenosis affects the downstream flow up to a distance of roughly 4$D$, 5$D$, 6$D$ and 7$D$ for axisymmetric $Re$ = 1000 and 2000, and eccentric 16% and 32% cases, respectively. After these lengths, fully developed conditions are observed and the mean axial velocities of all $Re$ = 1000 cases fit on the same curve.

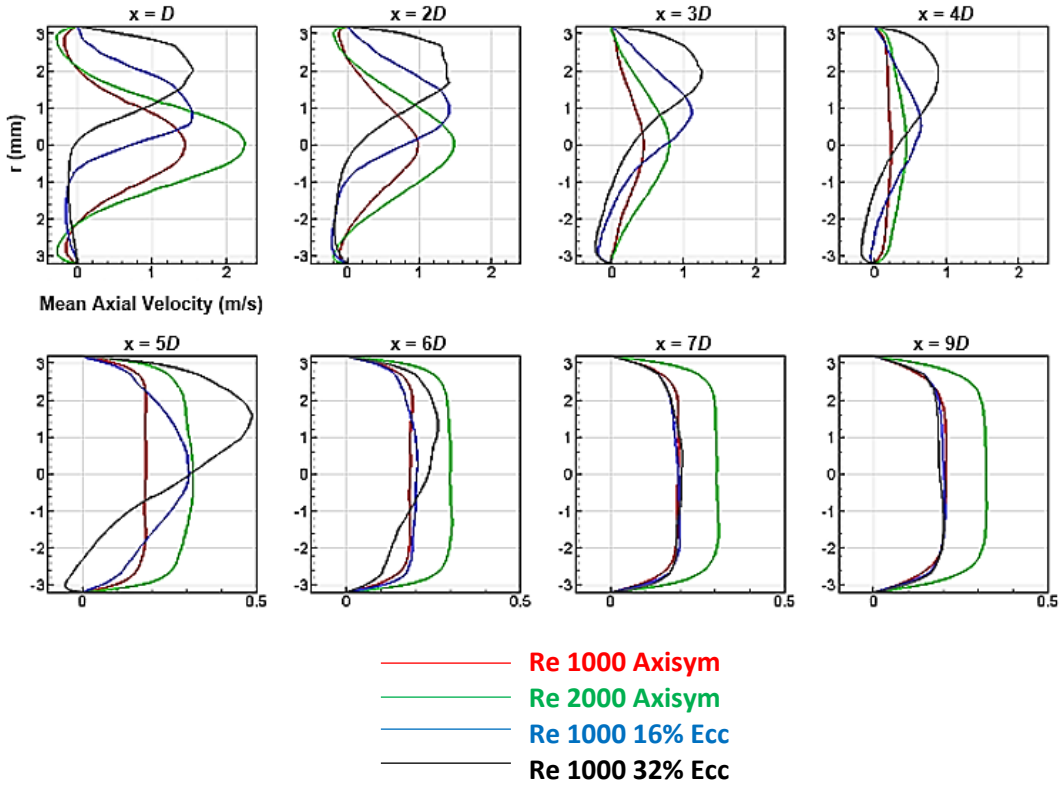


Figure 3.8. Mean axial velocity profiles at different locations downstream of the stenosis

Figure 3.9 shows the variation of the mean pressure along the vessel wall after the stenosis. Note that for eccentric models this data is gathered from the region of the wall where the flow jet is deflected. The drop of wall pressure between the stenosis exit and the exit of the flow domain is around 180 Pa for axisymmetric $Re$ = 1000 and eccentric cases, and 700 Pa for axisymmetric $Re$ = 2000 case. For axisymmetric cases, mean wall pressure reaches its maximum value at about 25 mm (~ 4$D$), whereas this value is about 35 mm (~ 5.5$D$) and 45 mm (~ 7$D$) for 16% and 32% eccentric cases, respectively, after which it drops almost linearly up to the exit.

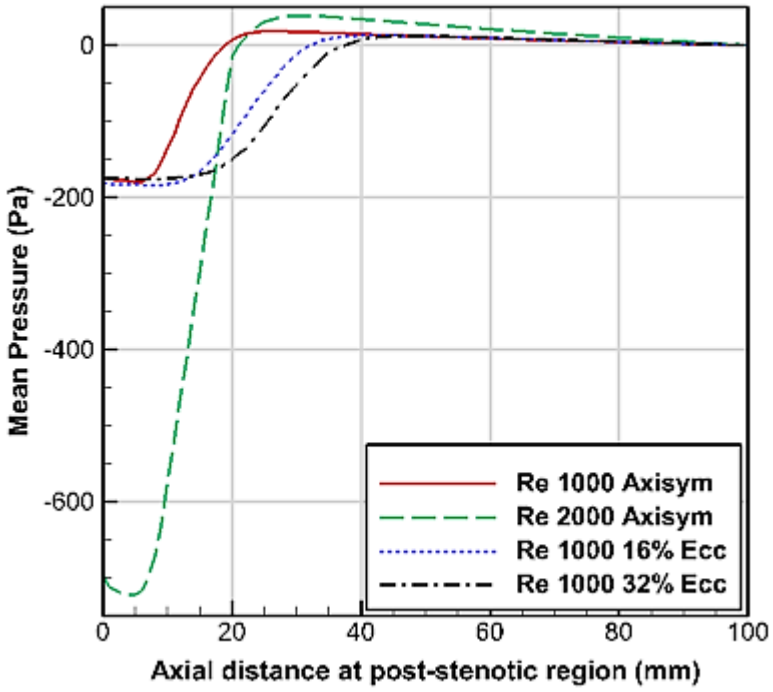


Figure 3.9. Mean wall pressures after the stenosis exit. For eccentric models this data is gathered from the region of the wall where the flow jet is deflected to

Figure 3.10 shows the TKE along the stenosis centreline as an indicator of the turbulent activity. TKE increases from the exit of the stenosis and the highest level of TKE is seen at about 10-12.5 mm (~ 2*D*) for axisymmetric cases and 25 mm (~ 4*D*) for eccentric ones. Then TKE decays gradually as the flow is re-laminarized. The effect of Re on TKE level is also clearly seen. Increasing *Re* from 1000 to 2000 for the axisymmetric model leads to a TKE rise of 2.5 times at the highest levels. Eccentricity also causes a rise in the TKE level, but the effect is not as severe as that of the flow rate.

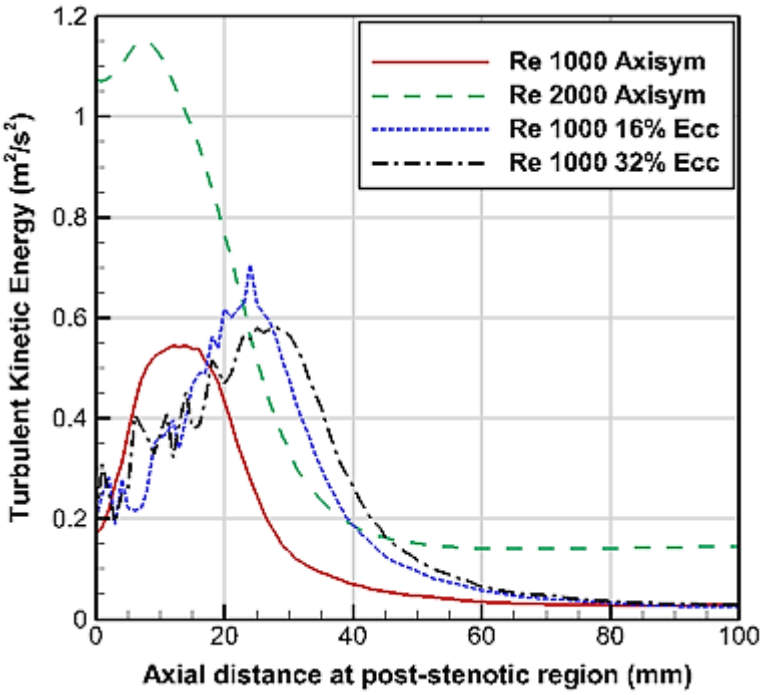


Figure 3.10. Turbulent kinetic energy after the stenosis exit calculated at the centreline of the stenosis

While listening cardiovascular sounds with a stethoscope, a doctor's ear captures pressure fluctuations from the ambient, known as acoustic pressure. By considering only the fluid region without the vessel wall or the tissues over it, the acoustic pressure generated at the inner vessel wall is calculated in this study. For such a calculation, first a simulation is continued until the mean wall pressures reach steady state. Then the time history of fluctuating wall pressure is recorded at 41 nodes, each separated 2.5 mm apart, for a duration of 0.4 s. For the eccentric models data is recorded along three different lines on the wall as shown in Figure 3.11. It is known that the cardiovascular system in human body generates acoustic waves in a frequency range of 20-1000 Hz [31]. Pressure data at the vessel wall is collected with a sampling frequency of 5000 Hz, which is enough to capture a frequency level up to 2500 Hz. During the 0.4 s data collection duration 2000 pressure values

are gathered from each of the 41 wall nodes. Figure 3.12 shows a sample of fluctuating pressures calculated at four different axial locations during a 0.4 s time interval. According to this figure both the magnitude and fluctuation frequency of the wall pressure are high at the stenosis exit, and they reduce gradually towards the exit.

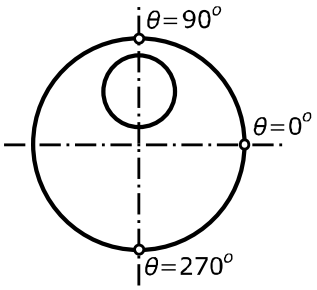


Figure 3.11. Three lines along which pressure data is collected for eccentric models

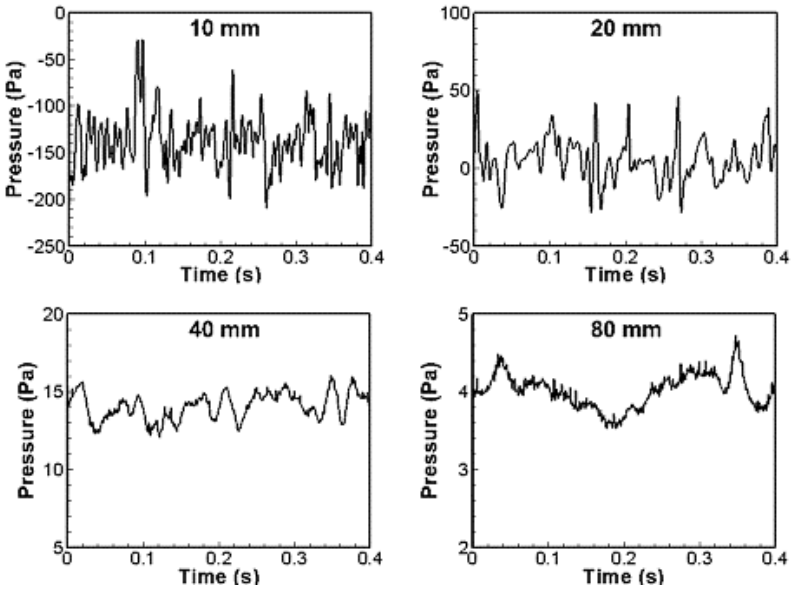


Figure 3.12. Sample pressure fluctuations recorded at four different axial locations on the vessel wall for an axisymmetric case

The pressure data collected at 41 wall nodes is post-processed by performing Hanning window filtering, followed by fast Fourier transform to provide contour plots seen in Figure 3.13 and Figure 3.14. Acoustic pressure amplitudes are converted to logarithmic scale using

$$p(\mathrm{dB}) = 20 \log_{10}\left(\frac{p(\mathrm{Pa})}{p(\mathrm{Ref})}\right) \tag{3.5}$$

where $p(\mathrm{Pa})$ is the pressure amplitude calculated by the simulations in pascals, $p(\mathrm{dB})$ is the acoustic pressure amplitude converted into decibels, and $p(\mathrm{Ref})$ is the reference pressure taken as 1 Pa to be compatible with the previous studies. Figure 3.13 compares numerical results of the current study, experimental results of Yazıcıoğlu et al. [35] and empirical results of Tobin and Chang [21] for the axisymmetric model. These plots show not only the axial variation of acoustic pressure on the vessel wall but also its frequency content. As seen in the figure, the general trends show good agreement both in terms of amplitude and spatial-spectral

distribution. This is an improvement over the numerical study of Salman et. al. [47] that had a significant difference in acoustic pressure amplitudes.

According to Figure 3.13 acoustic pressure amplitudes for Re = 2000 are generally higher than those of Re = 1000. For both flow rates acoustic pressure amplitudes are higher at the stenosis exit than those at the rest of the downstream region. The most active location is around 10 - 20 mm (1.5$D$ – 3$D$) downstream of the stenosis. Here it is worth to remember that for both flow rates the recirculation region length is around 20 mm (~ 3$D$). The recirculation region is clearly highly disturbed with a wide range of excited frequencies. Amplitudes decrease gradually with increasing frequency. The bands that can only be seen in the experimental results around 250 -300 Hz are explained by the authors of the study to be a possible consequence of a structural resonance of the rigid tube.

Figure 3.14 shows the acoustic pressure content of the eccentric models, collected along three different lines on the vessel wall. For both eccentricity ratios, acoustic pressure intensity is higher on the wall where the flow jet is directed to, which is shown as 90$^o$ in the figure. Acoustically, 180$^o$ line is the least active one. The important conclusion of this is that the region from which the measurement is taken becomes important to diagnose an eccentric stenosis properly. Acoustic pressure intensity obtained along the most active 90$^o$ line is higher than that obtained for the axisymmetric $Re$ = 1000 model. Location of the highest acoustic pressure magnitude is at around 20-30 mm, which is higher than the value obtained for the axisymmetric case.

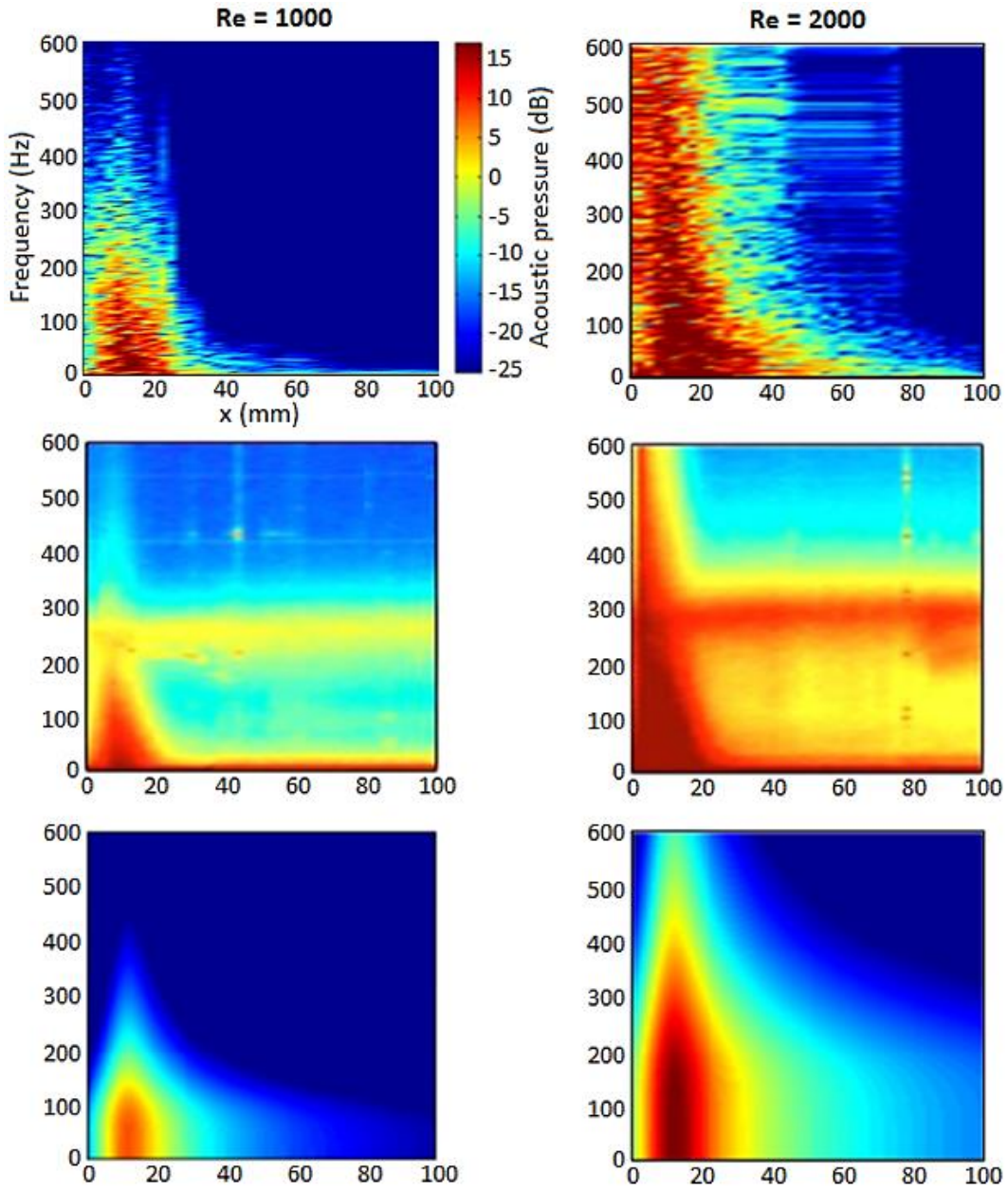


Figure 3.13. Acoustic pressure content for $Re$ = 1000 (left) and $Re$ = 2000 (right) for the axisymmetric model. Top: Numerical results obtained in the current study, Middle: Experimental results of Yazicioglu et al. [35], Bottom: Empirical curve fit of Tobin & Chang [21]

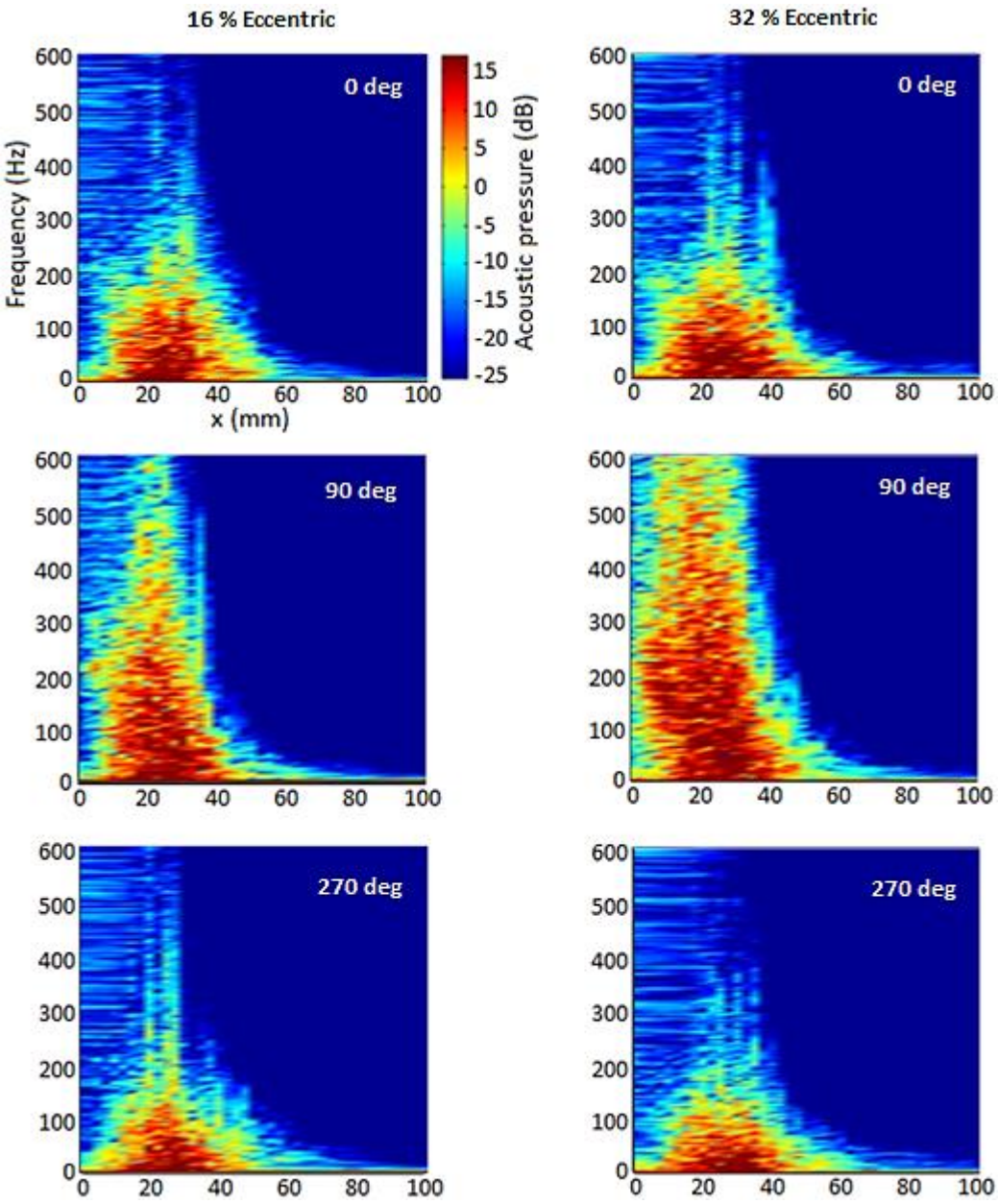


Figure 3.14. Acoustic pressure content for $Re$ = 1000 obtained along 3 different lines on the vessel wall. Left: 16% eccentric model, Right: 32% eccentric model

To study the maximum excitation location of different models, Figure 3.15 shows the axial variation of the RMS wall pressure fluctuations ($p'_{RMS}$). Pressure data of 90$^o$ line is used for the eccentric models. $p'_{RMS}$ increases to a maximum value at

12.5 mm (~ 2$D$) after the stenosis for both axisymmetric cases. These values are consistent with the range 1.5$D$ - 2.5$D$ given by Tobin and Chang [21]. After its peak, $p'_{RMS}$ decreases rapidly to zero at about 30 mm. Moreover, $p'_{RMS}$ value shows an increase of almost 4 times when $Re$ number increases from 1000 to 2000. This suggests that it may be easier to detect stenoses of patients under elevated flow conditions such as in an effort test, compared to normal flow conditions such as at rest. On the other hand, $p'_{RMS}$ increases to a maximum value at 25 mm (~ 4$D$) and 27.5 mm (~4.3$D$) after the stenosis for 16% and 32% eccentric cases, respectively. These results show that eccentricity is a more important parameter than the $Re$ in determining the maximum acoustic activity region. It is also found that as the eccentricity increases, the maximum activity point gets farther away from the stenosis. These results have practical significance as far as acoustic based diagnosis of stenotic blood vessels is concerned.

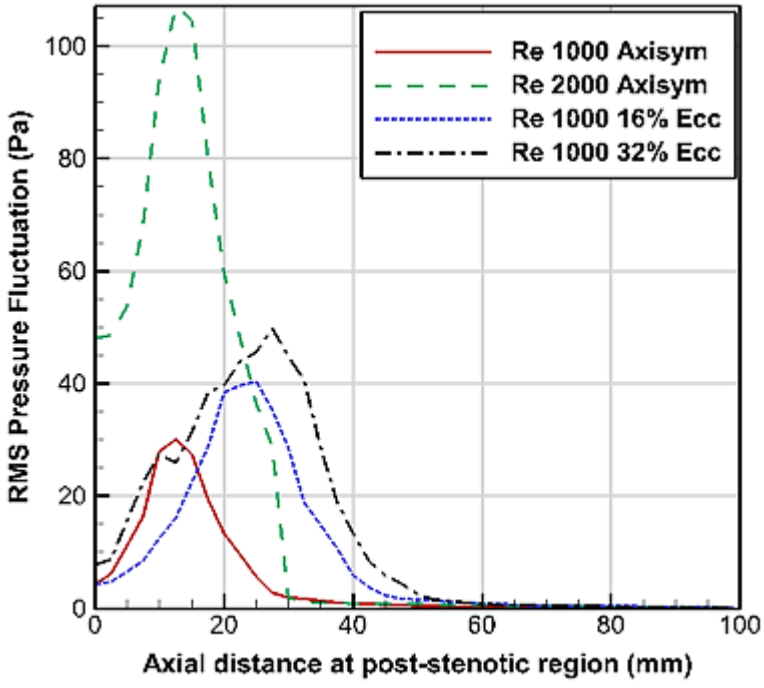


Figure 3.15. Axial variation of the RMS wall pressure fluctuation. For all models this data is gathered from 90$^o$ position on the wall.

Figure 3.16 shows a comparison of acoustic pressure at the maximum activity locations of flows at two different $Re$ of the axisymmetric model. The figure contains numerical result of this study, experimental findings of Yazıcıoğlu et al. [35], and empirical relations of Tobin and Chang [21]. Results are in good agreement especially at lower frequencies. As seen, the change in $Re$ does not significantly affect the shape of the spectrum, but it results in a noticeable increase in the amplitudes. Note the smoothing effect of the curve fitting process used by Tobin and Chang when presenting their experimental findings. The experimental results of Yazicioglu et al. are also noise filtered by means of 64 times RMS averaging during the data recording. On the other hand, current numerical results have a variable sampling rate around 1000 kHz due to the variable time step (around $10^{-6}$ s) used by the flow solver. The extracted data in the form of a time series of wall pressure is resampled at 5 kHz and transformed into spectral domain to be able to compare with the reference results.

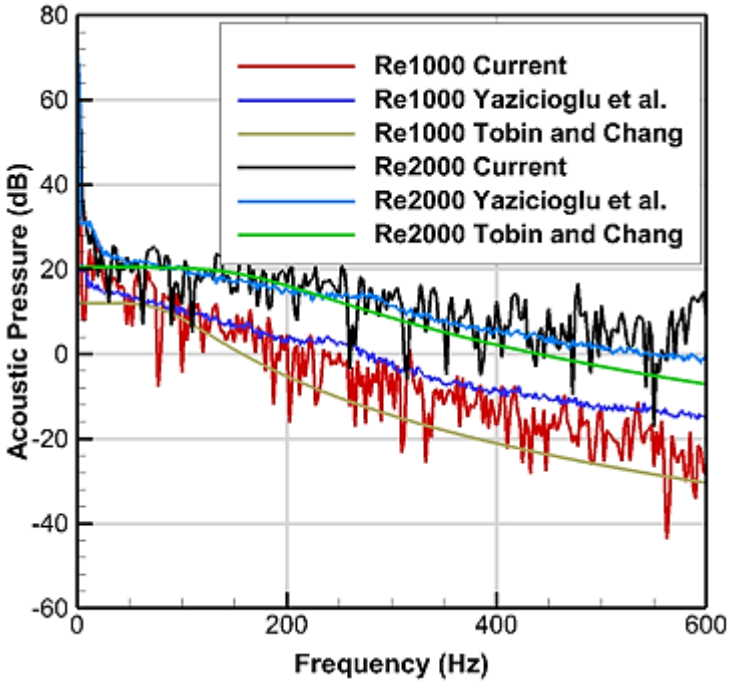


Figure 3.16. Frequency contents of the acoustic pressures for the axisymmetric model at $x$ = 12.5 mm.

Figure 3.17 shows the variation of frequency spectrum of wall pressure fluctuations, $E_{pp}$, with the non-dimensional frequency of fluctuations which is called as Strouhal number, $St = fD/U$ for axisymmetric models. These plots are obtained at the maximum excitation points. The solid lines drawn on each plot are intended to show the slope of the spectrum. The frequency at which the slope changes, usually called the 'break frequency', indicates the frequency at which the energy of the pressure fluctuations turns into noise [85]. Lu, Gross and Hwang explained this slope change to be not due to viscous dissipation of eddy energy into heat, but because of an energy transfer from turbulent flow to acoustic fluctuations [27]. Break frequency is important for the non-invasive diagnosis of stenosis using the sound emitted from a blood vessel. The higher the energy level of pressure fluctuations at break frequency at which these sounds are generated, the more the potential of them being transmitted through the arterial wall and being detectable

by means of non-invasive means [36]. At the point of maximum excitation, which is around $x$ = 12.5 mm, energy level of wall pressure fluctuations is higher than the other points considered.

Figure 3.18 compares the frequency spectrum of wall pressure fluctuations at maximum excitation locations for all models tested. For the eccentric models, data is gathered along the 90$^{o}$ line. Increasing Re from 1000 to 2000 leads to an almost 15-fold increase in the energy level, which is consistent with the 3.6 times difference seen earlier in Figure 3.15. Moreover, eccentricity also leads to an increase in the energy level which means that it may be easier to diagnose a stenotic blood vessel with a higher percentage of eccentricity at the same flow rate.

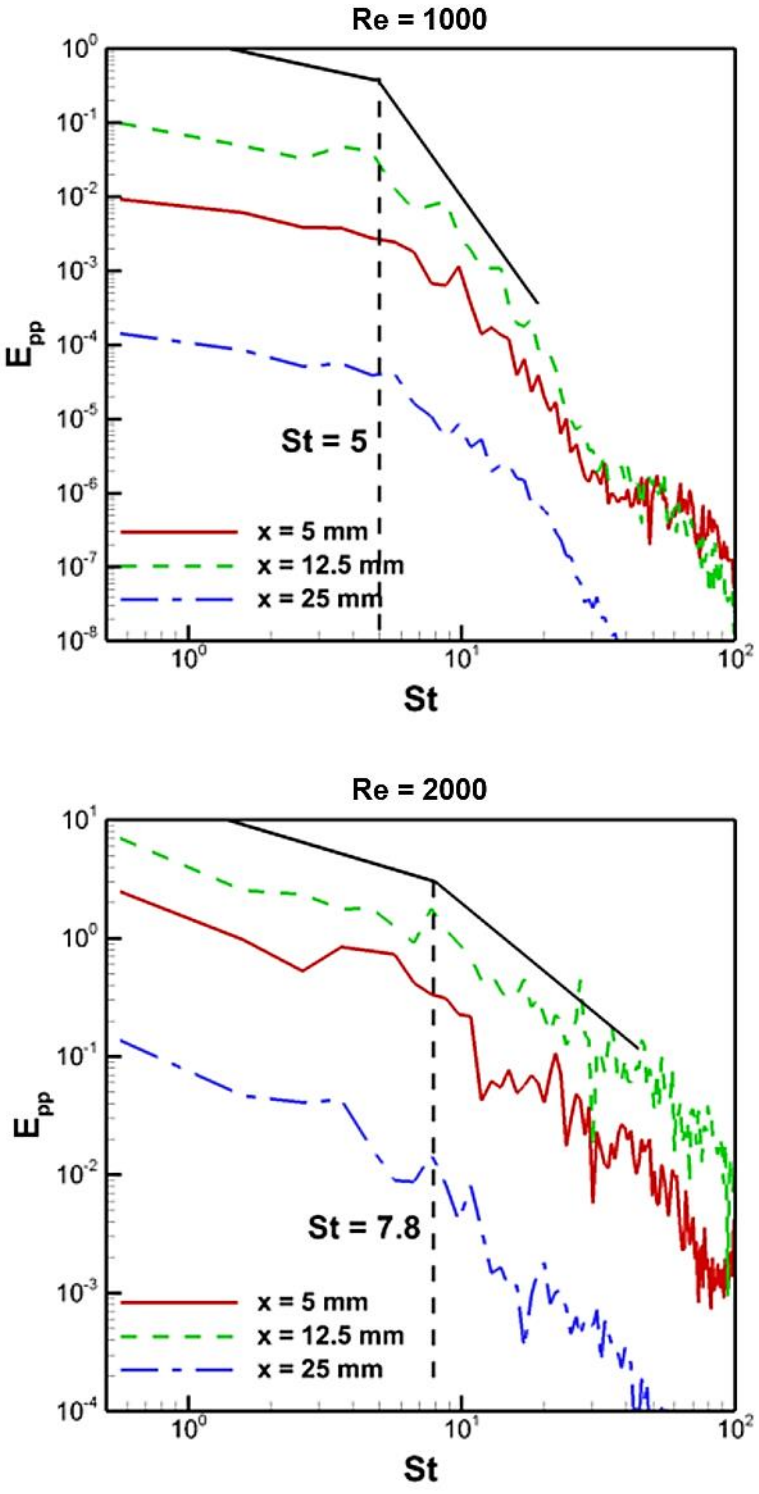


Figure 3.17. Frequency spectrum of pressure fluctuations for the axisymmetric model

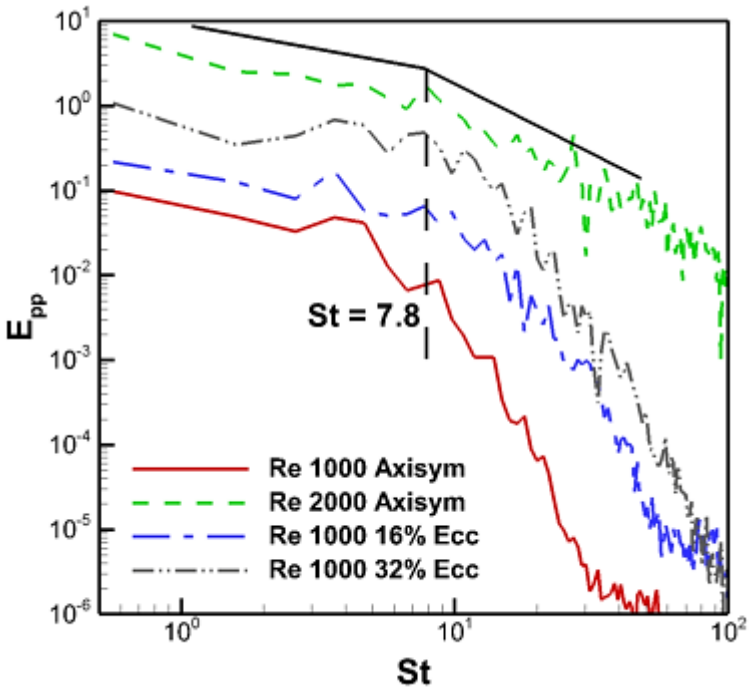


Figure 3.18. Comparison of energy spectrum of pressure fluctuations at the maximum excitation locations

### 3.4 Conclusion

In this chapter of the thesis, flow inside an idealized vessel with an axisymmetric blunt stenosis is considered and large eddy simulations are performed at two different $Re$. Furthermore, effect of eccentricity level on pressure fluctuations is studied using modified models. The focus was on the wall pressure fluctuations downstream of the stenosis exit.

Results of simulations conducted with axisymmetric stenosis geometry are compared with the previous experimental and theoretical studies, with good agreement in terms of both the magnitude and the frequency content of the acoustic pressure. It is seen that increasing $Re$ from 1000 to 2000 leads to 3.6 times increase in the RMS pressure fluctuation level, 2.5 times increase in the turbulent kinetic energy level and 15 times increase in the energy spectrum level, all calculated at

the maximum excitation point. The recirculation region extends up to 3 times the vessel diameter for the axisymmetric models for both $Re$.

For the eccentric cases, the location where the pressure data is collected becomes important. Acoustic pressure amplitudes at the vessel wall where the flow jet is directed to are considerably higher than that of axisymmetric models for the same $Re$. This difference increases as eccentricity increases. Acoustic pressures showed that, at the exit of the stenosis, there is a highly disturbed recirculation region with a wide range of excited frequencies, which elongates with increasing eccentricity. Maximum TKE levels of the eccentric models are slightly higher than that of the axisymmetric model. When compared with the axisymmetric models, the recirculation region elongates and extends up to 4 and 5 times of the vessel diameter for the 16% and 32% eccentric models, respectively. RMS of fluctuating wall pressures indicated that the axial distance where the maximum range of frequencies are excited are same for both $Re$ of axisymmetric model simulations, whereas this distance is larger for eccentric models. Furthermore, eccentricity also increases the level of energy spectrum level considerably.

# CHAPTER 4

# EFFECT OF STENOSIS SEVERITY AND ECCENTRICITY ON THE SOUND EMITTED FROM A STENOSED BLOOD VESSEL

## 4.1 Introduction

One of the most important parameters that medical doctors take into consideration for the clinical evaluation of atherosclerosis is the severity of stenosis. When the severity of the stenosis is above a certain level, it can lead to severe functional anomalies in the body and even death. Severity is also an important factor in determining how to treat atherosclerosis. Clinicians may choose one of the treatment options among lifestyle changes, medical treatment or surgical operation according to the degree of stenosis. As depicted in chapter 1, various aspects of the effect of severity on stenotic flow have been examined since the beginning of the studies in this field.

All these studies contain valuable information, but it is not possible to use this information in clinical practice until recent years. During the last decade, acoustic based systems and devices have been developed. These technologies have begun to be used especially in the diagnosis the severity of coronary artery disease. Unfortunately, these AD methods are used as a pre-diagnosis tool and mostly needed to be verified by an invasive method such as FFR or angiography. This suggests that further studies are needed to develop methods that can be used clinically to diagnose vascular stenosis without the need for invasive procedures.

Even if the stenosis severity is the same, the lumen geometry may vary for each plaque developing within the blood vessel. This lesion may be equally distributed

on the vessel wall resulting in an axisymmetric structure, as well as concentrating on one side of the vessel wall, causing an eccentric stenosis. There is a great tendency in human body for eccentric stenosis development as seen in Figure 4.1 [86]. In some studies in the literature, the effect of eccentricity on the influence length of stenosis [87], the flow pattern after stenosis [88], the intensity of turbulence and pressure drop [89, 90], the risk of plaque rupture [91] have been investigated. However, there is a serious lack of studies in the literature related to the effect of eccentricity on the sounds emitted from stenosed blood vessels. The literature review showed that there are more work to be done to investigate the influence of stenosis severity and eccentricity on the murmurs generated in stenosed arteries. The studies carried out in this section are made in order to contribute to the literature in this aspect for the purpose of non-invasive diagnosis. In the following sections of this chapter, the axisymmetric and eccentric stenosis models with different severities, properties of computational grids and simulation settings are described. Results about the effect of stenosis severity and eccentricity on post-stenotic flow field and acoustic radiation are presented and discussed in the next section. This chapter is finished with a section in which the conclusions are summarized.

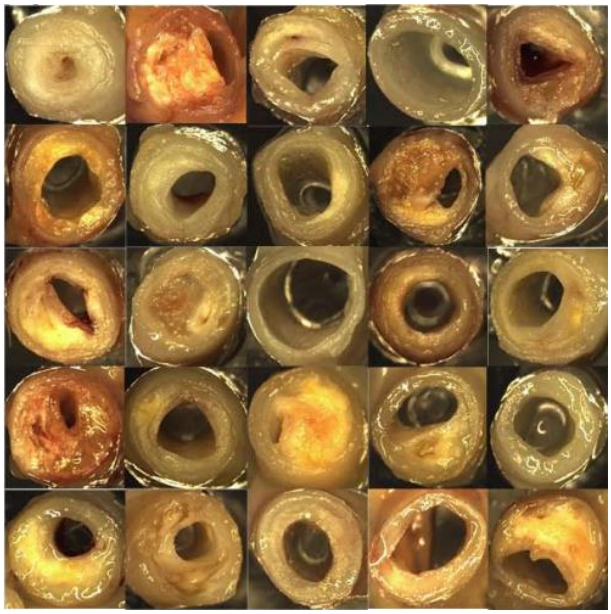

Figure 4.1. Stenosed coronary artery – autopsy data reported in [86]

### 4.2 Computational Model

Five idealized axisymmetric and eccentric stenosis models with different severities used in this chapter are given in Figure 4.2 and Figure 4.3, respectively. All of these models are based on a healthy, real femoral artery of 6.4 mm in diameter ($D$). For all models, pre- and post-stenosis vessel lengths are 37.2 mm and 100 mm, respectively. The length of the stenosis region is $2D$ for all models. One of the important parameter of these models, stenosis severity ($S$) is defined as:

$$S = \left(1 - \frac{A_{throat}}{A_{inlet}}\right) \times 100 \tag{4.1}$$

where $A_{throat}$ and $A_{inlet}$ are the cross-sectional areas at the throat of the stenosis and at the inlet of the blood vessel. The other parameter percent eccentricity ($e$) is calculated as given in equation (3.1). The stenosis severities used in this study are 50%, 60%, 75%, 87% and 95%. On the other hand, in the eccentric models, the percent eccentricity ratios for these stenosis severities are 14.6%, 18.3%, 25%,

32%, 77.6%, respectively. Stenosis shape is chosen as elliptical which is commonly used in previous studies in the literature [44, 70, 92].

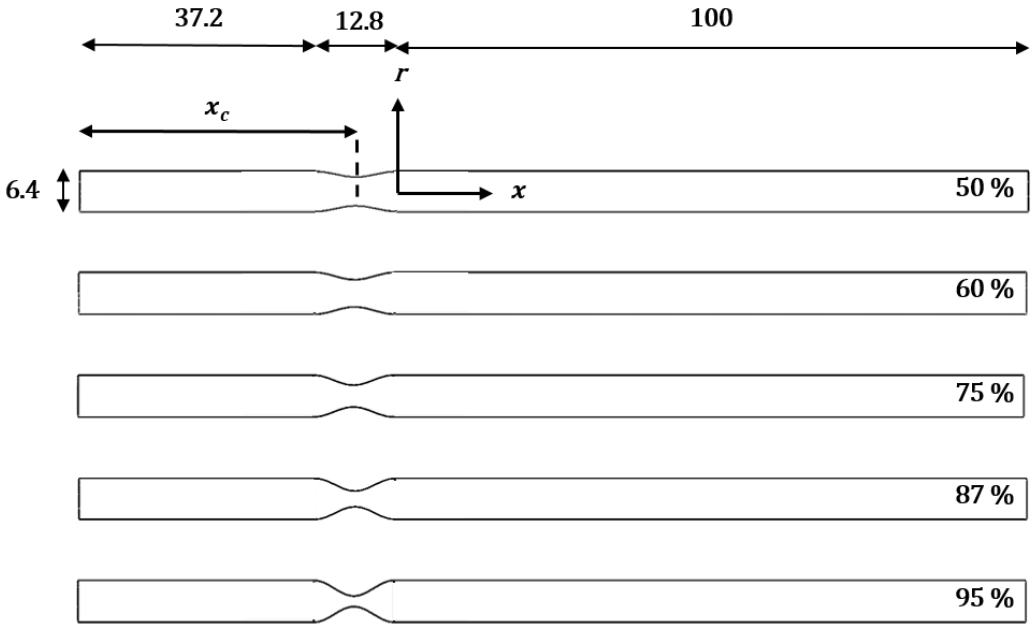


Figure 4.2. Sectional views of axisymmetric models. Flow is from left to right. Figure is out of scale and dimensions are in mm.

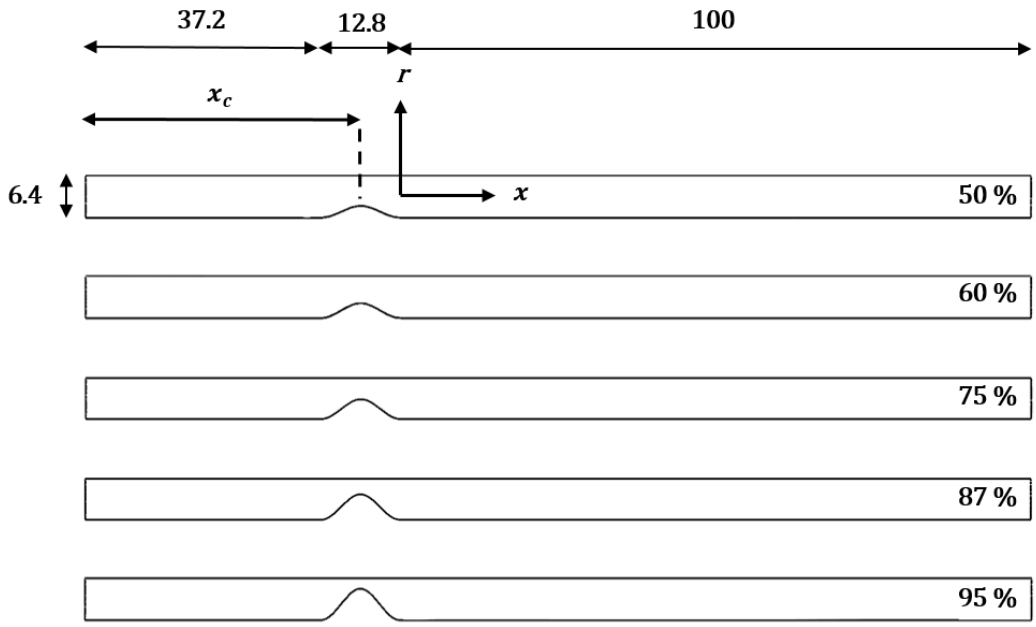


Figure 4.3. Sectional views of eccentric models. Flow is from left to right. Figure is out of scale and dimensions are in mm.

The function specifiying the elliptical shape is

$$r(x) = \frac{1}{2}D\left[1 - s_c\left(1 + \cos\left(\frac{2\pi(x - x_c)}{L}\right)\right)\right] \tag{4.2}$$

where $D$ is the diameter of the non-stenosed vessel, $L$ is the length of the stenosed region and $x_c$ is the location of the centre of the stenosis. $s_c$ = 0.14, 0.18, 0.25, 0.32 and 0.38 for the 50%, 60%, 75%, 87% and 95% stenosis severities, respectively.

Several studies in the literature states that transient nature of non-Newtonian blood models affects the flow phenomena and so the veloctiy profiles and pressure drop after stenosis under pulsatile flow conditions [92, 93, 94, 95]. For this reason, Bird-Carreau non-Newtonian blood model [96] is used, with the following effective viscosity equation

$$\mu = \mu_\infty + (\mu_0 - \mu_\infty)[1 + (A\dot{\gamma})^2]^{(n-1)/2} \quad (4.3)$$

where $\mu_\infty = 0.0035$ Pa · s, $\mu_0 = 0.056$ Pa · s, $A = 3.131$ and $n = 0.3568$. The fully developed physiological pulsatile flow profile specified at the inlet is shown in Figure 4.4. This flow profile is defined by the following equation [97]

$$u(r,t) = \frac{u(r)}{2(1-(r^2/R^2))}\left(1 + \sum_{n=1}^{5} A_n \cos(2n\pi t - B_n)\right) \quad (4.4)$$

is used, where $R$ is the radius of vessel, $u(r)$ is the Poiseuille velocity profile and constants $A_n$ and $B_n$ are listed in Table 4.1. Reference pressure at the outlet is set to zero and the no slip boundary condition is used at the wall boundaries, which are taken to be rigid.

Table 4.1. Constants ($A_n$ and $B_n$) of the pulsatile flow profile

| ***n*** | ***1*** | ***2*** | ***3*** | ***4*** | ***5*** |
|---|---|---|---|---|---|
| $\boldsymbol{A_n}$ | 0.29244 | -0.5908 | 0.2726 | 0.198 | 0.1124 |
| $\boldsymbol{B_n}$ | -4.027 | -6.509 | -1.913 | -1.461 | -0.074 |

$Re$ for blood flow in the body varies from 1 in small arterioles to approximately 4000 in the aorta, based on the peak velocity and the vessel diameter [65]. The velocity profile used in this study consists of systolic and diastolic phases of 0.5 seconds and has a mean $Re$ value of 1000, with a minimum and maximum $Re$ of 55 and 2278, based on the average inlet speed ($u_{mean}$) and the vessel diameter ($D$). The 6 points shown on Figure 4.4 represent the accelerating, peak and decelerating phases of systolic and diastolic parts of the pulsatile flow.

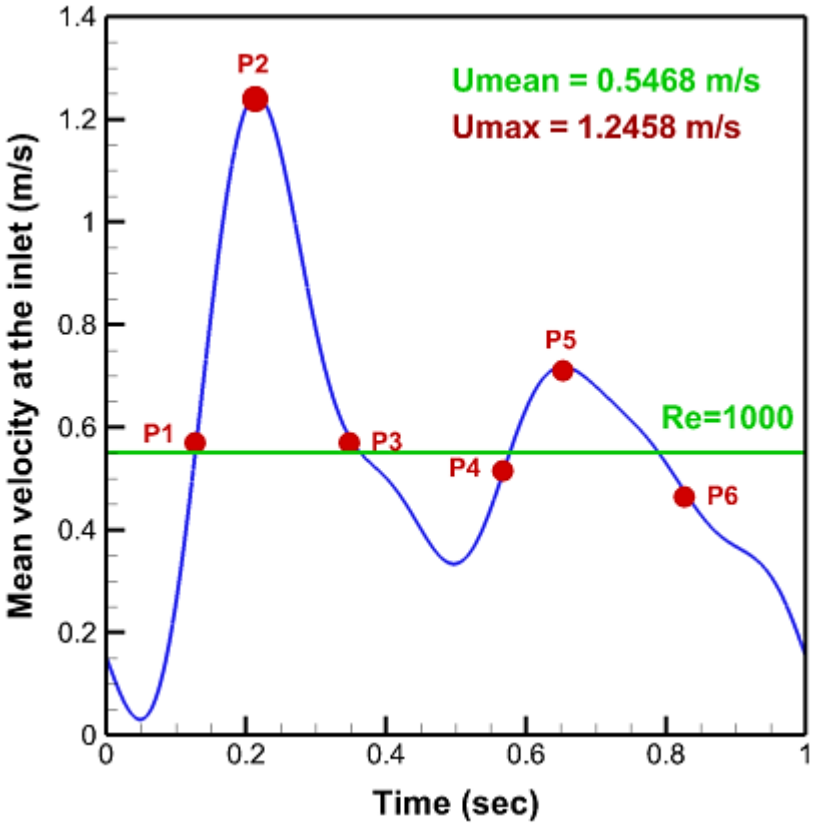


Figure 4.4. Physiological pulsatile flow profile used in the simulations

The incompressible flow solver, turbulence model and discretization schemes used in this chapter are the same as those used in the previous chapter. To understand the dependency of the solutions on the time step, preliminary simulations are conducted. Results are compared in terms of mean and fluctuating wall pressures and $\max(Co) = 1$ is found to be satisfactory. With this setting, time step varies between $5 \times 10^{-7}$ s - $1.7 \times 10^{-5}$ s and $3.9 \times 10^{-7}$ s - $1.2 \times 10^{-5}$s during the simulation of the 95% axisymmetric and eccentric models, which are the models with the most severe turbulence activity after stenosis, respectively.

Mesh independence study is performed for the 95% axisymmetric and eccentric models, due to the reason mentioned above, using the four different meshes given in Table 4.2. All meshes use the grid structure shown in Figure 4.5 and composed

of hexahedral cells. The elements at pre and post-stenosis region tighten towards the stenosis. While simulating wall bounded turbulent flows, near-wall mesh resolution becomes very critical. $y^+ < 1$ condition holds for all the meshes used in this chapter. Mesh independence is checked with the mean wall pressure variation shown in Figure 4.6, as well as the acoustic pressure distribution obtained by using wall pressure fluctuations in Figure 4.7 and frequency contents of the acoustic pressures at $x$ = 10 mm in Figure 4.8. After these mesh independence simulations, Mesh 3 is evaluated to be suitable and applied to all other severities of stenosis. At the maximum flow velocity instance in the simulation conducted with this mesh, the minimum Kolmogorov length scale is obtained as 0.0192 mm and 0.0128 mm immediately after the stenotic region. At this region maximum cell size is 0.3 mm and 0.225 mm for 95% axisymmetric and eccentric models, respectively. Therefore, the ratio of cell size to the Kolmogorov length scale is kept below 15.63 and 17.58 for these models, respectively. These values are below the maximum allowable range of 20-40 given in the literature [81]. The two other metrics, mentioned in chapter 3 are also calculated, to check the suitability of mesh resolution. The highest $LES\_M$ value at the post-stenotic region is found as 0.054 and 0.062 for the 95% axisymmetric and eccentric models, respectively. Moreover, the lowest $LES\_IQ$ values are detected as 0.845 and 0.823 at post-stenotic region of these models, respectively. These values are reasonable for LES according to the scales of these metrics defined in the literature [82, 83]. After all these checks, the simulations are conducted by using Mesh 3. It lasts approximately 2 pulses for the 50% and 60%, 3 pulses for the 75% and 87%, 4 pulses for the 95% models to reach the time periodic state in terms of mean flow parameters for both axisymmetric and eccentric forms. The wall clock time to reach time periodic state varies 2 to 21 days for axisymmetric models and 3 to 30 days for eccentric models on 24 cores of the TRUBA HPC system of TÜBİTAK ULAKBİM High Performance and Grid Computing Center.

Table 4.2. Details of meshes used in mesh independence simulations of 95% axisymmetric model

| | **95% Axisymmetric** | | **95% Eccentric** | |
|---|---|---|---|---|
| | **# of Nodes** | **# of Cells** | **# of Nodes** | **# of Cells** |
| **Mesh 1** | 199362 | 215845 | 212109 | 216227 |
| **Mesh 2** | 1419429 | 1430265 | 1561241 | 1580498 |
| **Mesh 3** | 2211840 | 2272782 | 2445604 | 2472782 |
| **Mesh 4** | 4119931 | 4166987 | 4279152 | 4303406 |

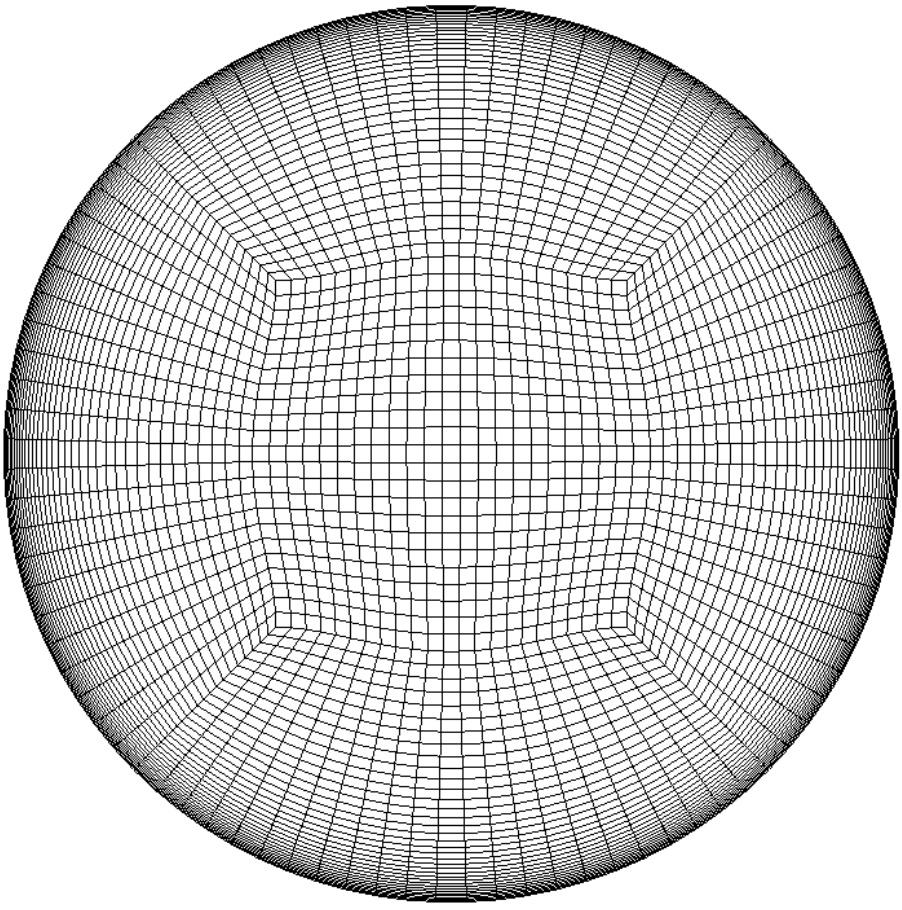

Figure 4.5. Grid structure at the vessel inlet used in all meshes

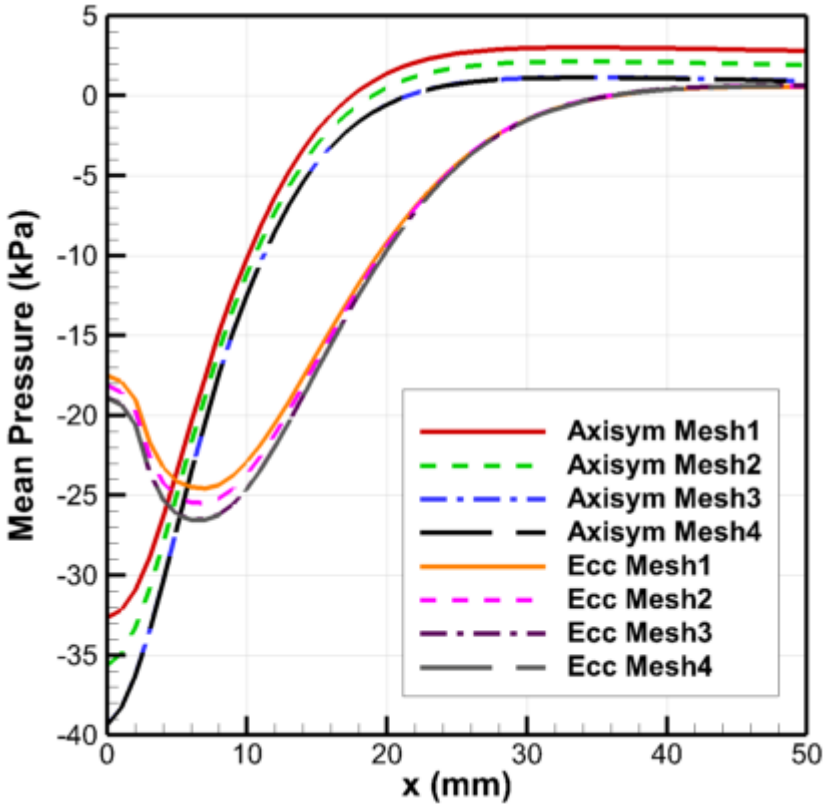


Figure 4.6. Mean wall pressures obtained with four different meshes for 95% axisymmetric and eccentric models. For the eccentric models the data is gathered from 90$^{o}$ position on the wall.

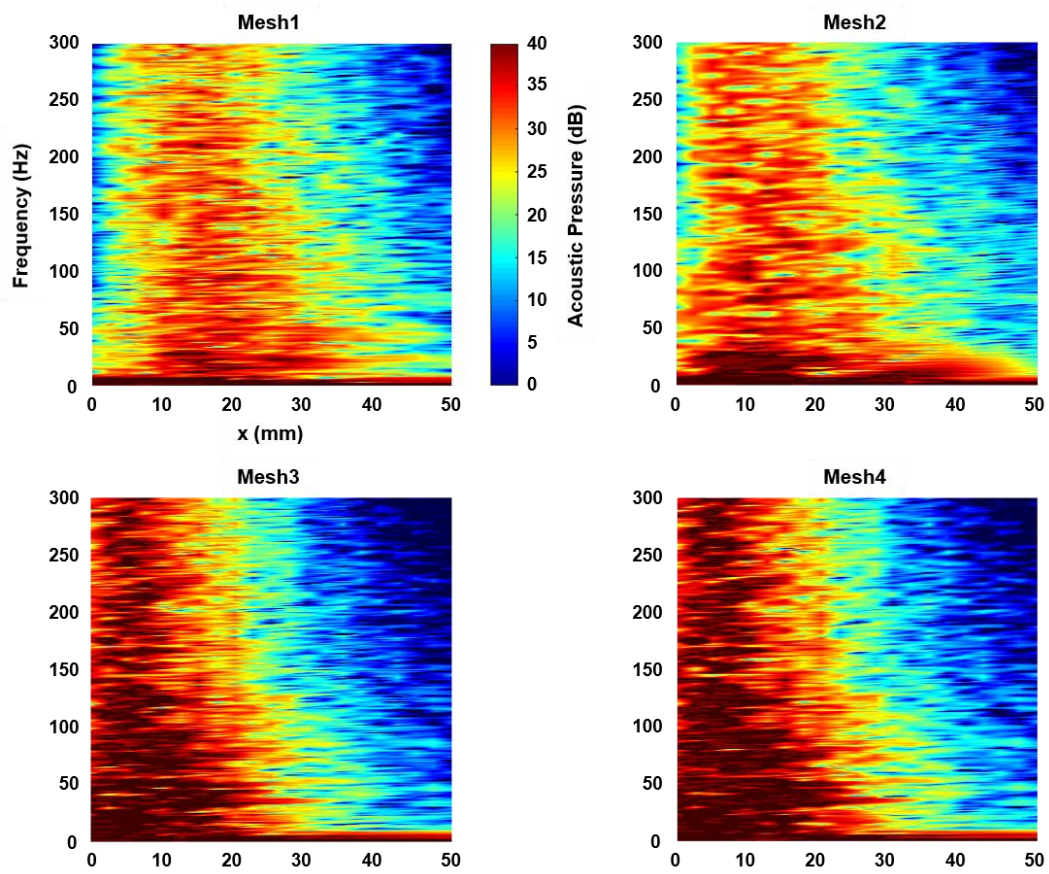


Figure 4.7. Acoustic pressure contours obtained with four different meshes for 95% axisymmetric model

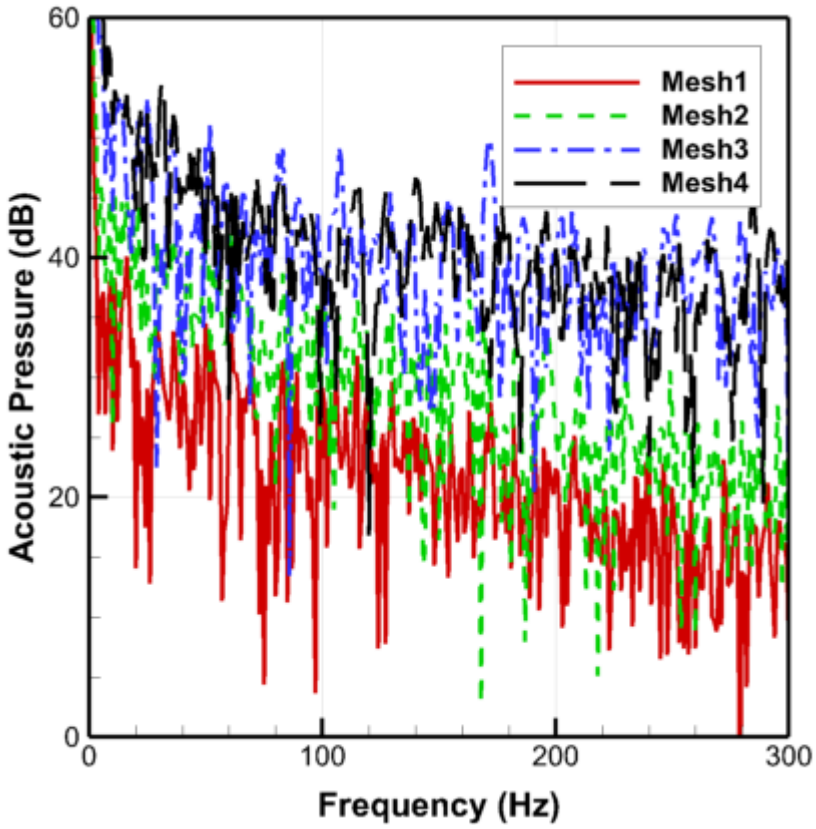


Figure 4.8. Frequency contents of the acoustic pressures for the 95% axisymmetric model at $x$ = 10 mm obtained with four different meshes

### 4.3 Results and Discussion

All the results presented in this section are obtained after the flow reaches the time periodic state in terms of mean flow parameters. Mean axial velocity profiles at the maximum flow instant (P2) are shown in Figure 4.9 and Figure 4.10 for axisymmetric and eccentric models, respectively. Note that velocity is non-dimensionalized by $U_{\max} = 1.246$ m/s, which is the maximum value of the pulsatile flow profile at the inlet.

According to Figure 4.9, the jet created by the stenosis affects the downstream flow up to a distance of roughly 7$D$ for 50% and 60% stenosis models. For the 75%,

87% and 95% stenosis severities, this distance extends to approximately 6*D*, 5*D* and 4*D*, respectively. The change of these distances with the effect of eccentricity can be seen in Figure 4.10. The distances to reach the fully developed flow for the eccentric models are found to be more than 7*D* for the 50% and 60%, 5*D* for the 75% and 6*D* for 87% and 95% stenosis models. Eccentricity also rises the length of recirculation region for all of the stenosis severities.

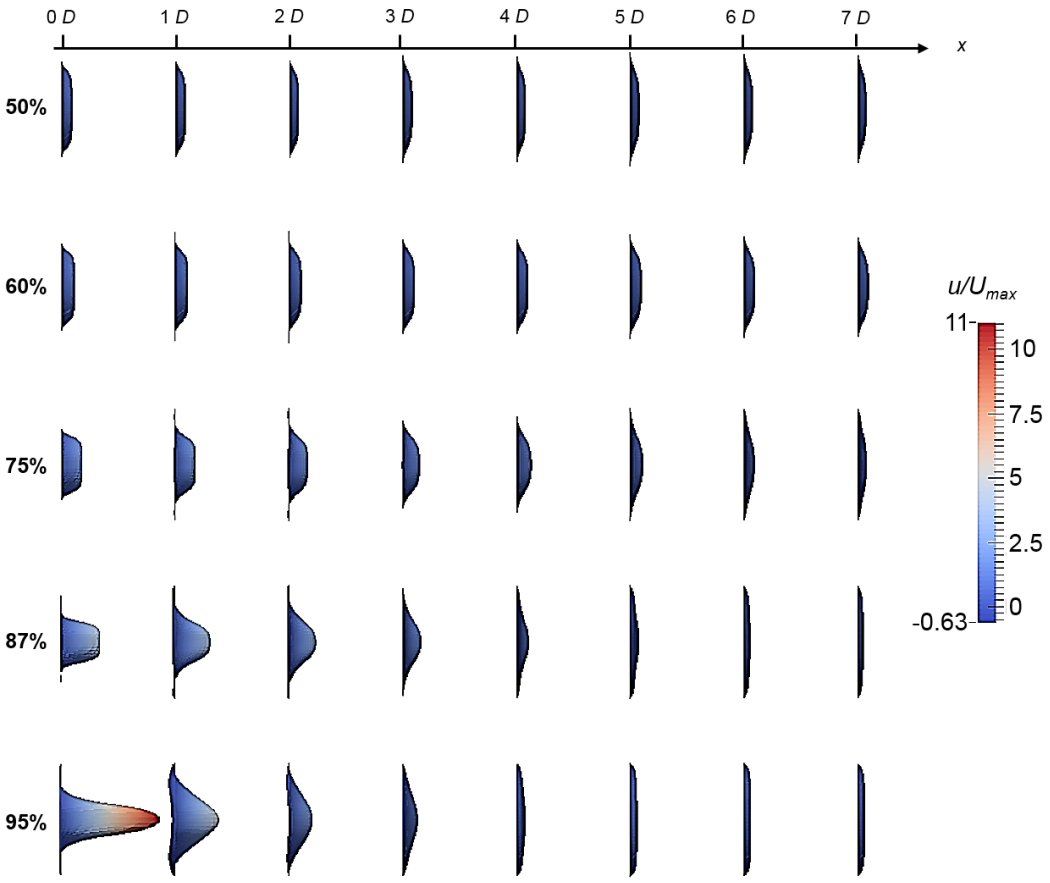


Figure 4.9. Non-dimensional mean axial velocity profiles after the stenosis exit for axisymmetric models

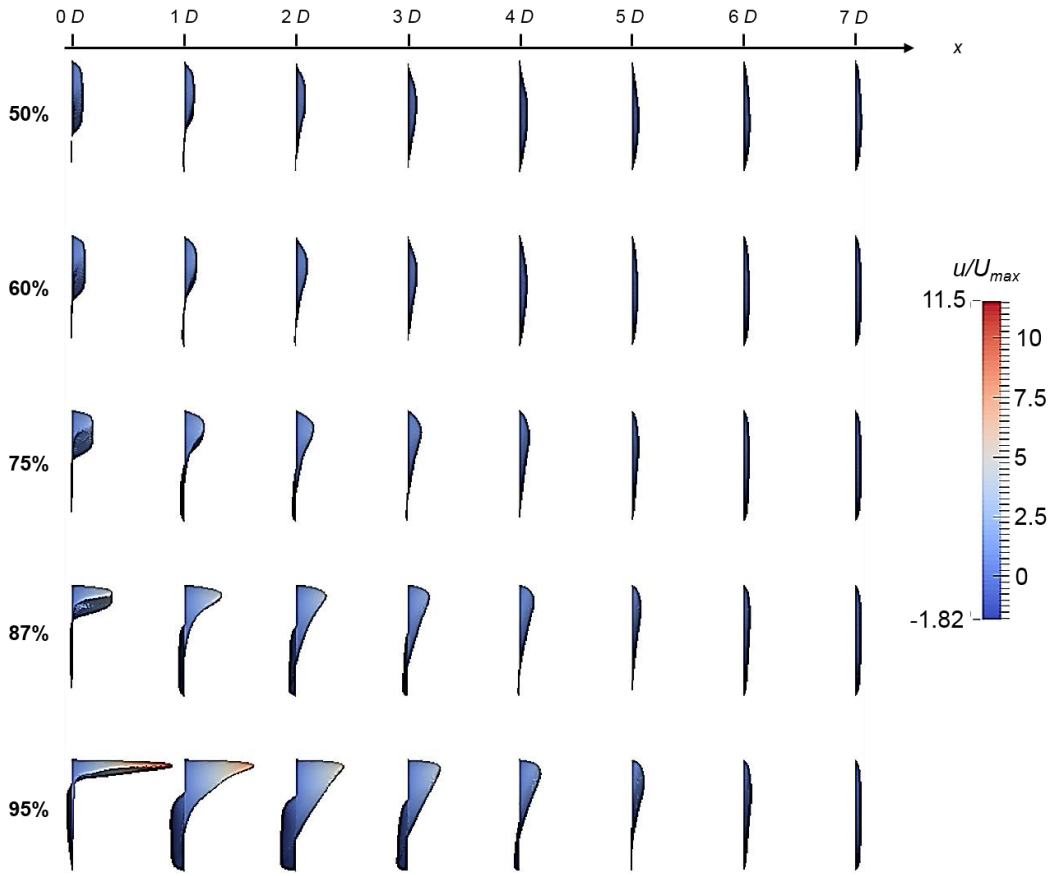


Figure 4.10. Non-dimensional mean axial velocity profiles after the stenosis exit for eccentric models

Figure 4.11 and Figure 4.12 shows the variation of the mean pressure along the vessel wall after the stenosis at the maximum flow instant (P2) for axisymmetric and eccentric models, respectively. The drop of wall pressure between stenosis exit and the exit of the flow domain of axisymmetric models is about 0 kPa for 50%, 1 kPa for 60%, 3 kPa for 75%, 8 kPa for 87% and 36 kPa for 95% stenosis severities as seen in Figure 4.11. To investigate the effect of data collection position, this data is extracted along three different lines on the wall as shown in Figure 3.11 for the 95% eccentric model and presented in Figure 4.12. It is determined that the mean pressure value at the wall position where the flow jet is deflected differs

according to the other two positions. For this reason, the data obtained from the 90$^{o}$ position of the vessel wall are presented for other stenosis severities. The wall pressure drop values for eccentric models are about 0 kPa, 1 kPa, 2.5 kPa, 6 kPa and 18 kPa for 50%, 60%, 75%, 87% and 95% eccentric stenosis models, respectively. When these two figures are jointly evaluated, it can be seen that the increase in the degree of stenosis leads to a remarkable rise in the pressure drop after the stenosis. It is also observed that the eccentricity causes a decrease in the drop of mean wall pressure values after stenosis. As the severity of stenosis increases, these facts becomes even more pronounced. It is stated in the literature that the magnitude of the mean pressure drop after shrinkage directly affects wall pressure fluctuations [98]. Thus, it is expected that the intensity of pressure fluctuations may increase as the severity of stenosis increases for both axisymmetric and eccentric models.

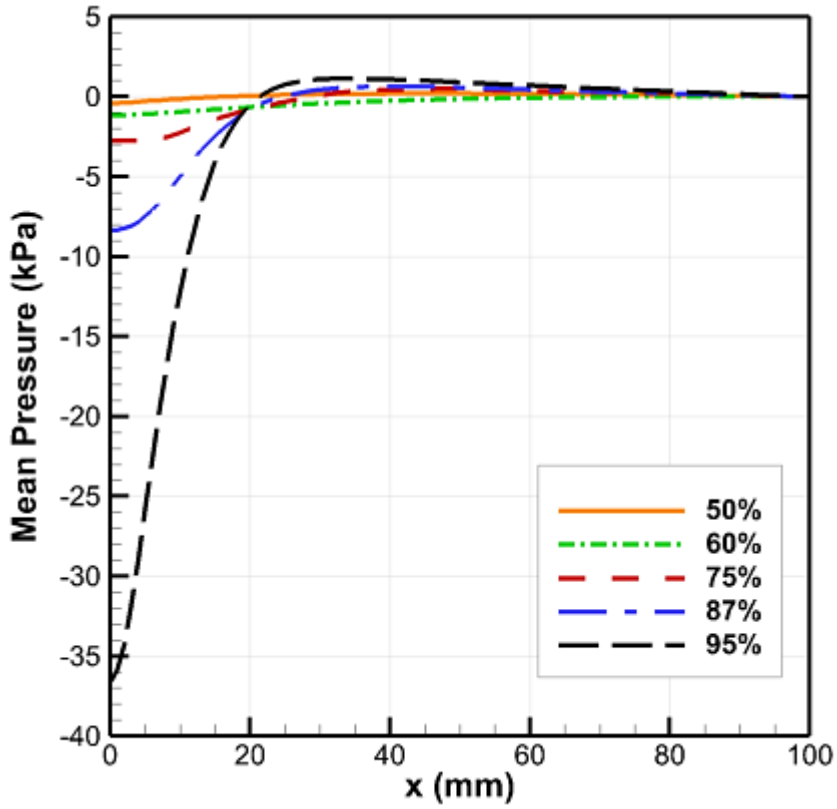


Figure 4.11. Mean wall pressures along the wall for axisymmetric models

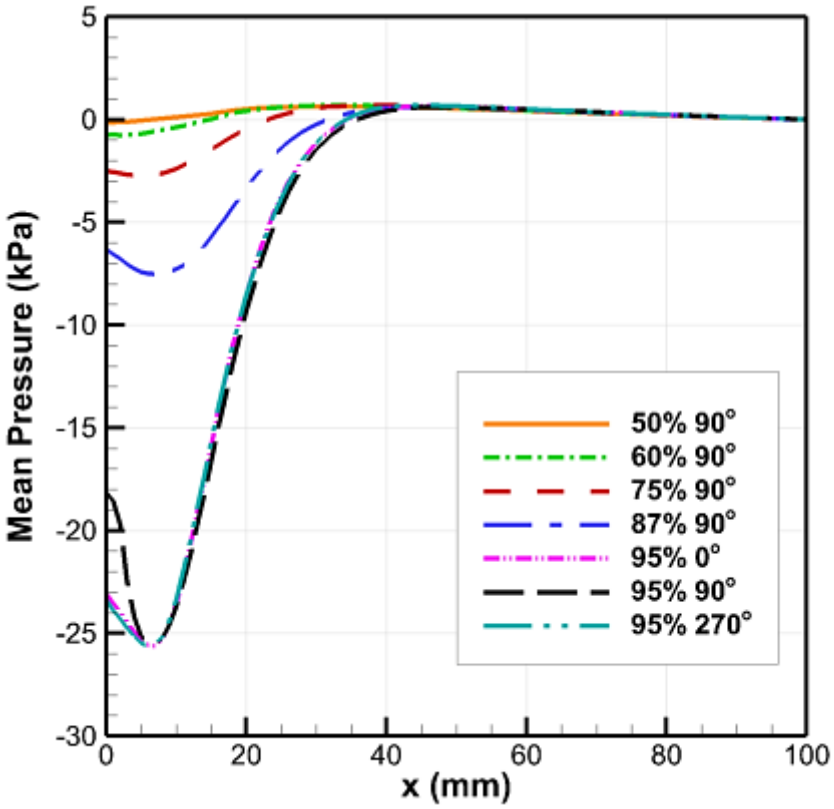


Figure 4.12. Mean wall pressures along the wall for eccentric models

TKE along the centerline of the stenosis, shown in Figure 4.13, for axisymmetric and eccentric models are presented in Figure 4.14 and Figure 4.15 respectively. It should be noted that the TKE values in both of these plots are given at phase P2 and normalized by $(U_{max})^2$.

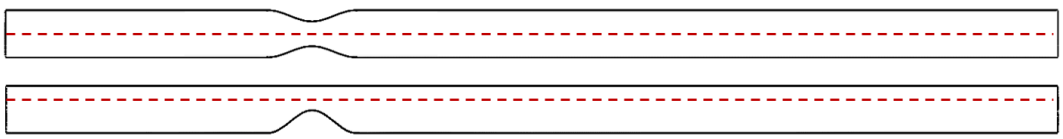

Figure 4.13. Centerline of stenosis for axisymmetric and eccentric models

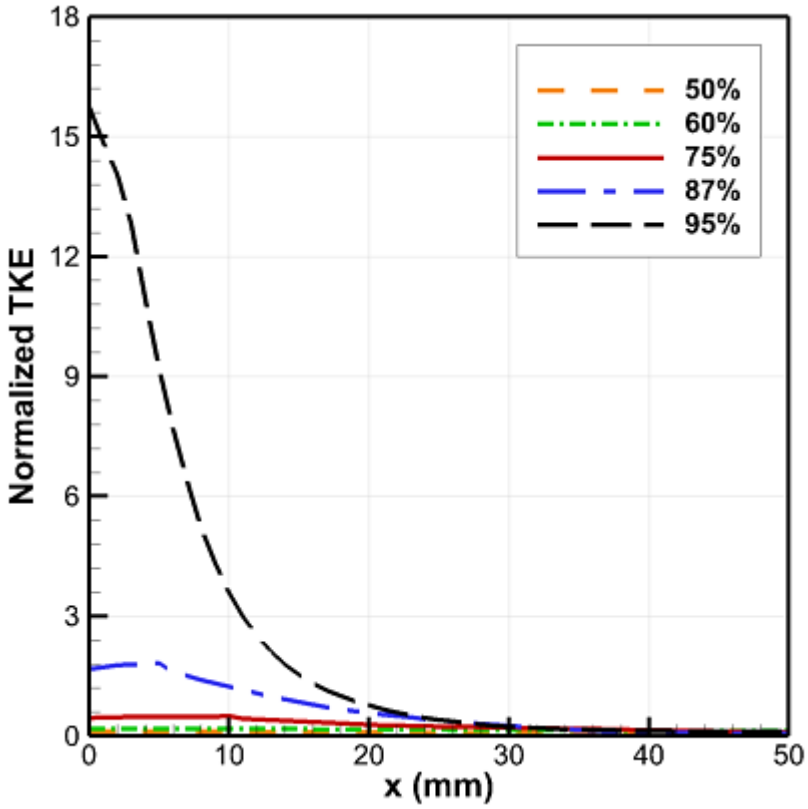


Figure 4.14. Normalized TKE along the stenosis centerline for axisymmetric models

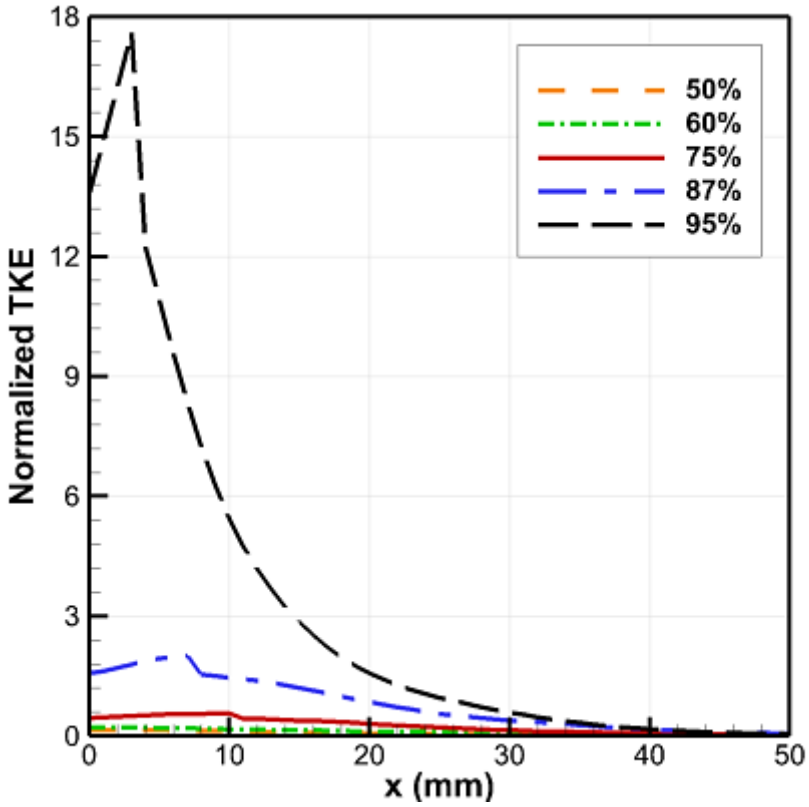


Figure 4.15. Normalized TKE along the stenosis centerline for eccentric models

Figure 4.14 and Figure 4.15 indicate that the post-stenotic turbulence activity is almost zero for both axisymmetric and eccentric forms of 50% and 60% models. For degrees of 75% and above, the intensity of TKE rises significantly with increasing stenosis severity. Turbulent activity reaches its highest level at at $x$ = 5 mm, 2.5 mm and 0 mm and $x$ = 7.5 mm, 5 mm and 2.5 mm after stenosis for 75%, 87% and 95% axisymmetric and eccentric models, respectively. 95% model leads to a TKE rise of almost 8 and 32 times at the highest levels when compared with 87% and 75% stenosis models, respectively. The effects of the stenosis severity on TKE level are clearly seen. Although eccentricity has also an enhancing effect on TKE, this effect is not as strong as that of severity of the stenosis.

Acoustic pressure contours provided in Figs. 4.16-4.18 are obtained by converting the wall pressure data into logarithmic scale as explained in chapter 3.3. These pressure data collected during a pulsatile flow cycle at 41 nodes along the vessel wall with a sampling frequency of 5000 Hz after the flow reaches time periodic state in terms of mean flow parameters. According to Figure 4.16, 50% axisymmetric model exhibits very similar characteristics with the unstenosed vessel in terms of spectral behaviour. Although the acoustic pressure intensities are slightly higher in the 0-100 Hz frequency range, a similar behaviour is seen at the 60% stenosis severity. The spectral behavior of the acoutic pressure contours differs for severities of 75% and above. It is observed that in these models, higher acoustic pressure intensity is observed within 20 mm immediately after the stenosis exit and this activity is gradually decreased at the rest of the post-stenotic region.

Figure 4.17 shows the acoustic pressure content of the 95% eccentric model, collected along three different lines on the vessel wall shown in Figure 3.11. Acoustic pressure intensity is higher on the wall where the flow jet is directed to, which is shown as $90^{o}$ in the figure. Acoustically, $270^{o}$ line is the least active one. The importance of this finding in terms of diagnostic perspective is that the region from which the measurement is taken becomes important to diagnose an eccentric stenosis properly.

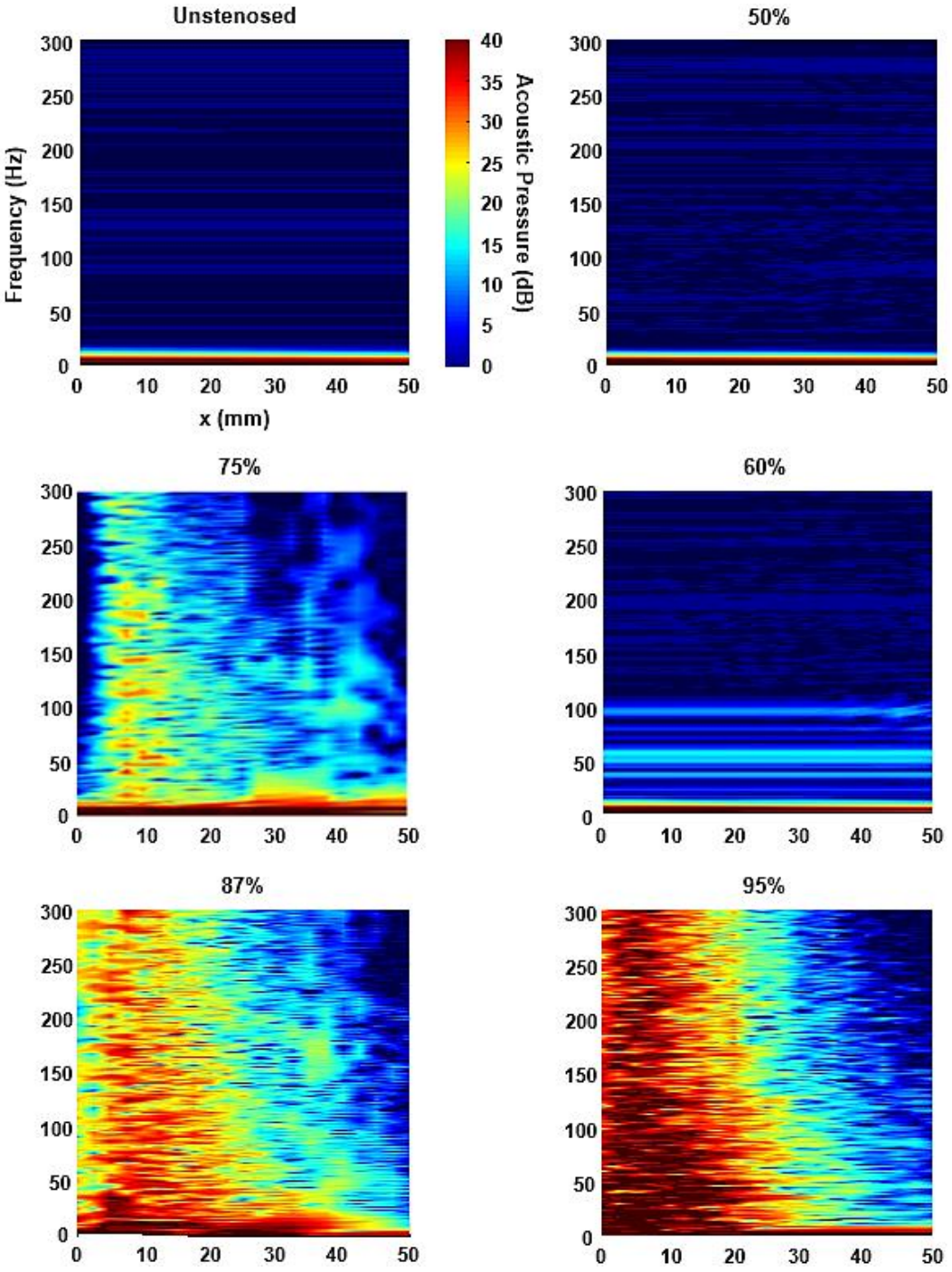


Figure 4.16. Acoustic pressure content for unstenosed and axisymmetric models

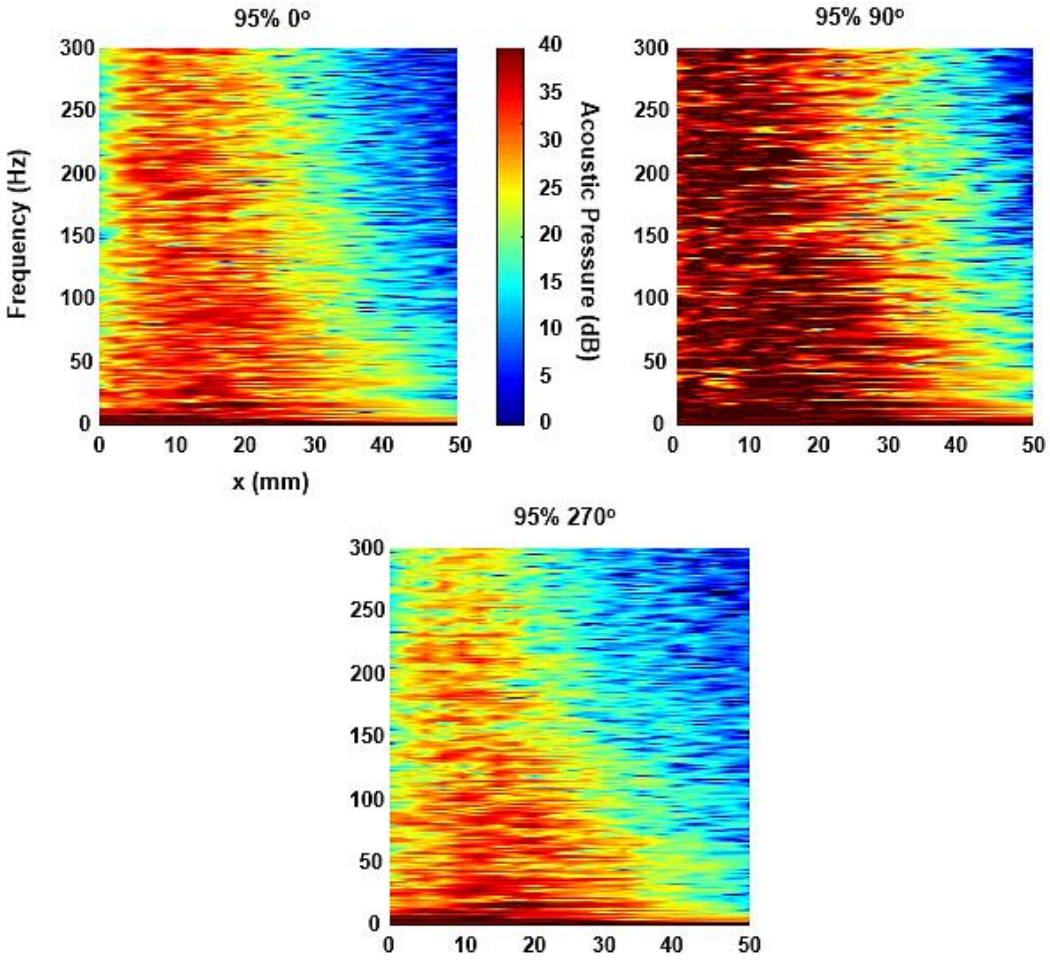


Figure 4.17. Acoustic pressure content for different positions of 95% eccentric model

Acoustic pressure contours obtained from the 90° position is presented for all eccentric models in Figure 4.18. More activity is observed in the 0-150 Hz band for the 50% and 60% models due to the effect of eccentricity. Length of the highest acoustic activity region is about 30 mm after stenosis, which is higher than the value obtained for the axisymmetric cases. Figure 4.16 and Figure 4.18 commonly indicate that acoustic pressure amplitudes rise with increasing stenosis severity.

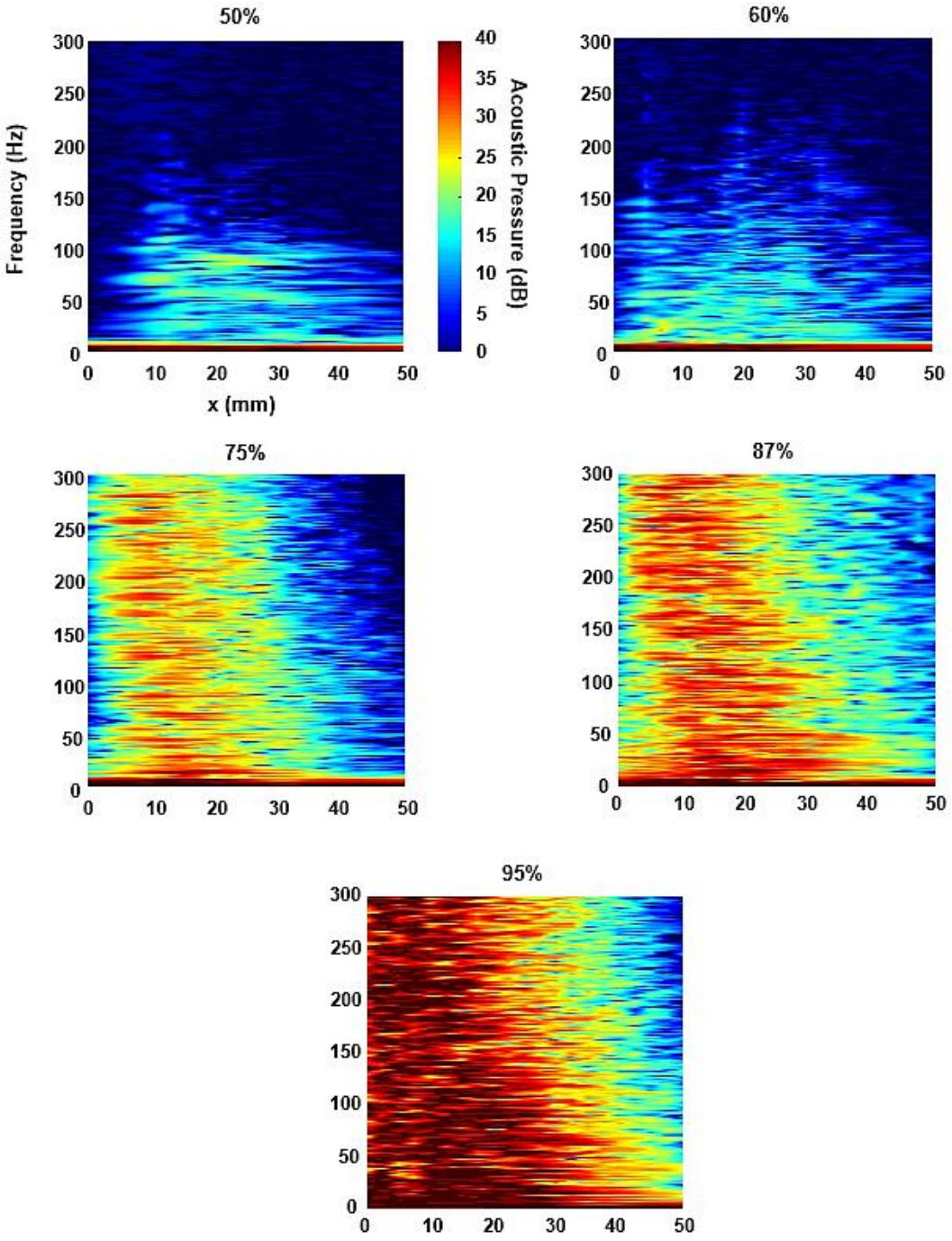


Figure 4.18. Acoustic pressure content for eccentric models. For all models this data is gathered from 90$^{o}$ position on the wall.

In addition, to study the maximum excitation location of different models, axial variation of the RMS of wall pressure fluctuations, $p'_{RMS}$, is plotted in Figure 4.19 and Figure 4.20. Pressure data of 90º line is used for the eccentric models. $p'_{RMS}$ values of 50% and 60% severities can be treated as negligible for both axisymmetric and eccentric stenosis forms. $p'_{RMS}$ has the maximum value at $x$ = 5 mm, 2.5 mm and 0 mm and $x$ = 7.5 mm, 5 mm and 2.5 mm after stenosis for 75%, 87% and 95% axisymmetric and eccentric models, respectively. These results show that eccentricity is an important parameter in determining the maximum acoustic activity region. Moreover, $p'_{RMS}$ value shows an increase of almost 6 and 3 times when stenosis severity is increased to 95% from 75% and 87%, respectively for axisymmetric cases. Whereas these values are determined as 8 and 3.5 for eccentric models, respectively.

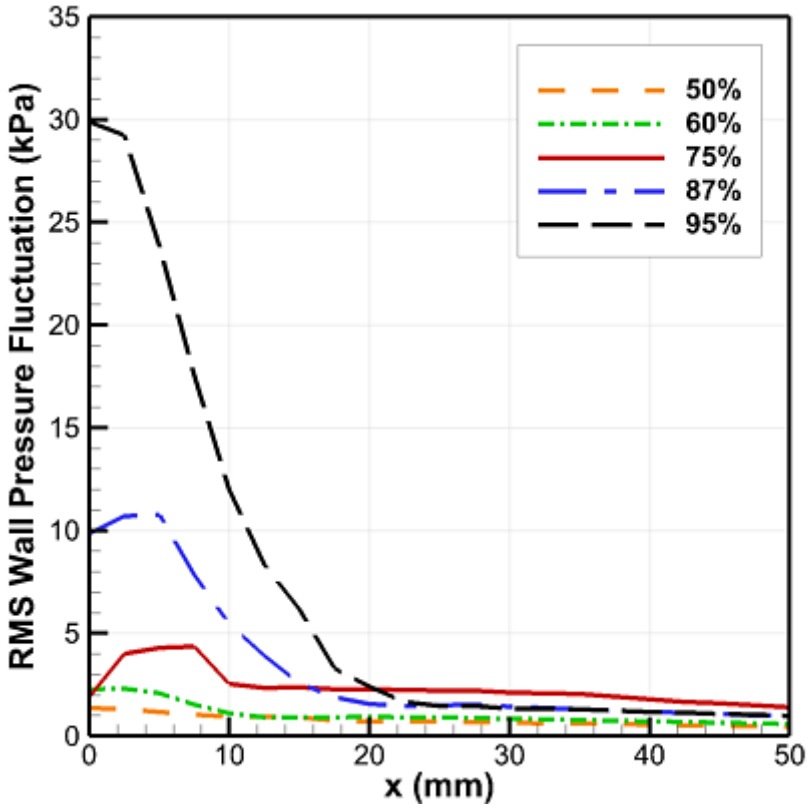


Figure 4.19. Axial variation of the RMS wall pressure fluctuation for axisymmetric models.

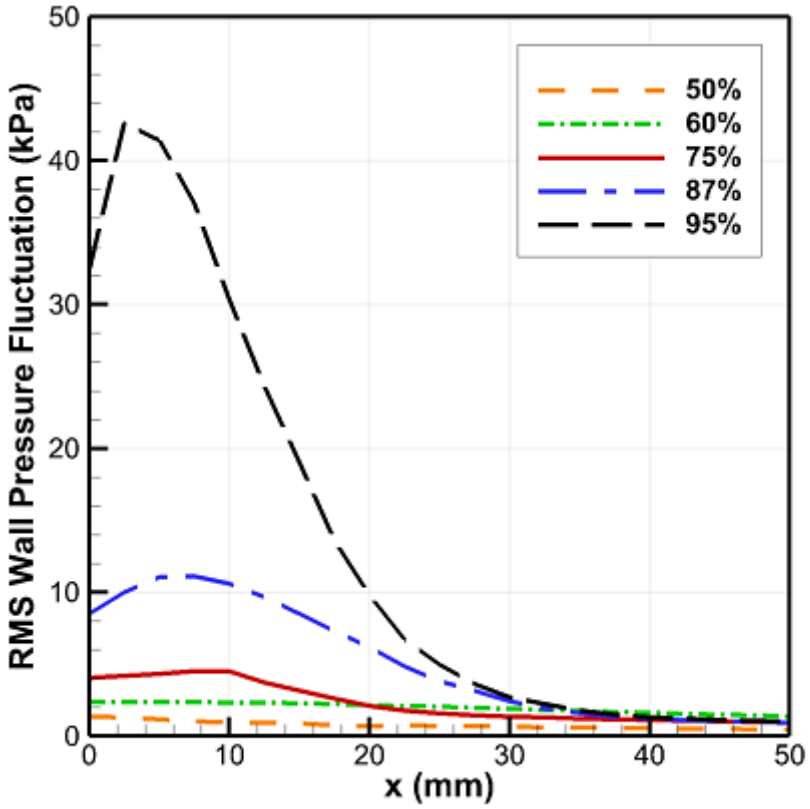


Figure 4.20. Axial variation of the RMS wall pressure fluctuation for eccentric models. For all models this data is gathered from 90$^{o}$ position on the wall.

Figure 4.21 and Figure 4.22 show the time history of wall pressure fluctuations obtained for the axisymmetric and eccentric models at the maximum excitation points. For the eccentric models, only the result of the vessel wall region where the flow jet directed is presented. The pressure obtained from the wall of the unstenosed vessel does not contain any fluctuations because the flow remains in the laminar regime. Although slight pressure fluctuations around the P2 phase are seen in eccentric models, the situation is almost the same as the unstenosed model for 50% and 60% stenosis severities. The activity intensity associated with pressure fluctuations begins to increase with 75% stenosis severity for both symmetric and eccentric models. It is seen that both the fluctuation frequency and the magnitude becomes higher as the stenosis severity increases. Changing the morphology of the

stenosis from axisymmetric to eccentric exhibits an effect in the same direction. It is seen that for all the models with stenosis severity of 75% and above, the most intense pressure fluctuations are detected close to the maximum velocity instance. Clinically, this shows that it is easier to detect acoustic signals due to pressure fluctuations during heart contraction. It is important to note that these findings can only be obtained with pulsatile simulations. In addition to these figures zoomed view of wall pressure fluctuations at a certain time interval for the 75% axisymmetric model is shown in Figure 4.23. This figure is presented to give an idea about the magnitude of pressure fluctuations that can be captured during the simulations.

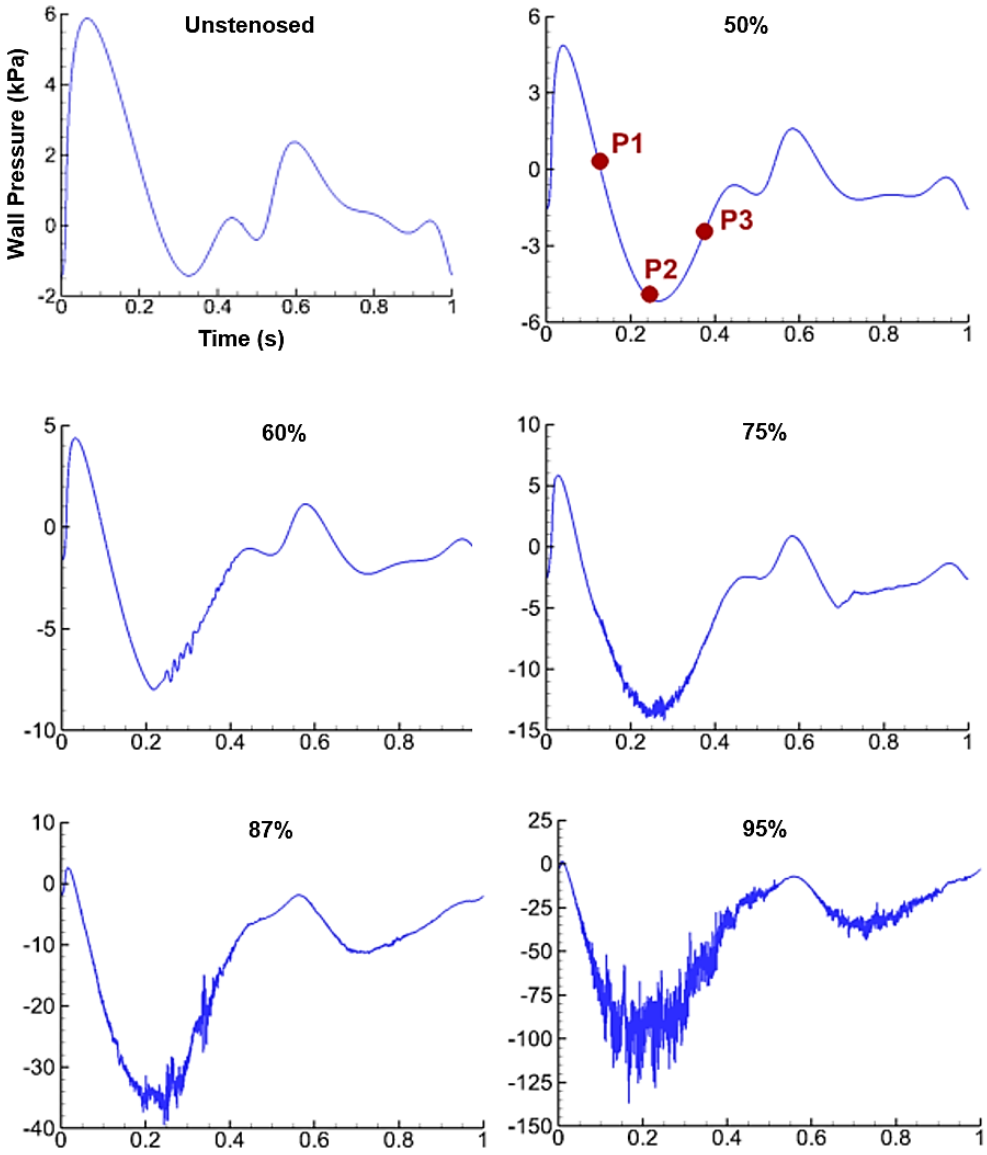


Figure 4.21. Time history of wall pressure fluctuations during one cycle for the unstenosed and axisymmetric models

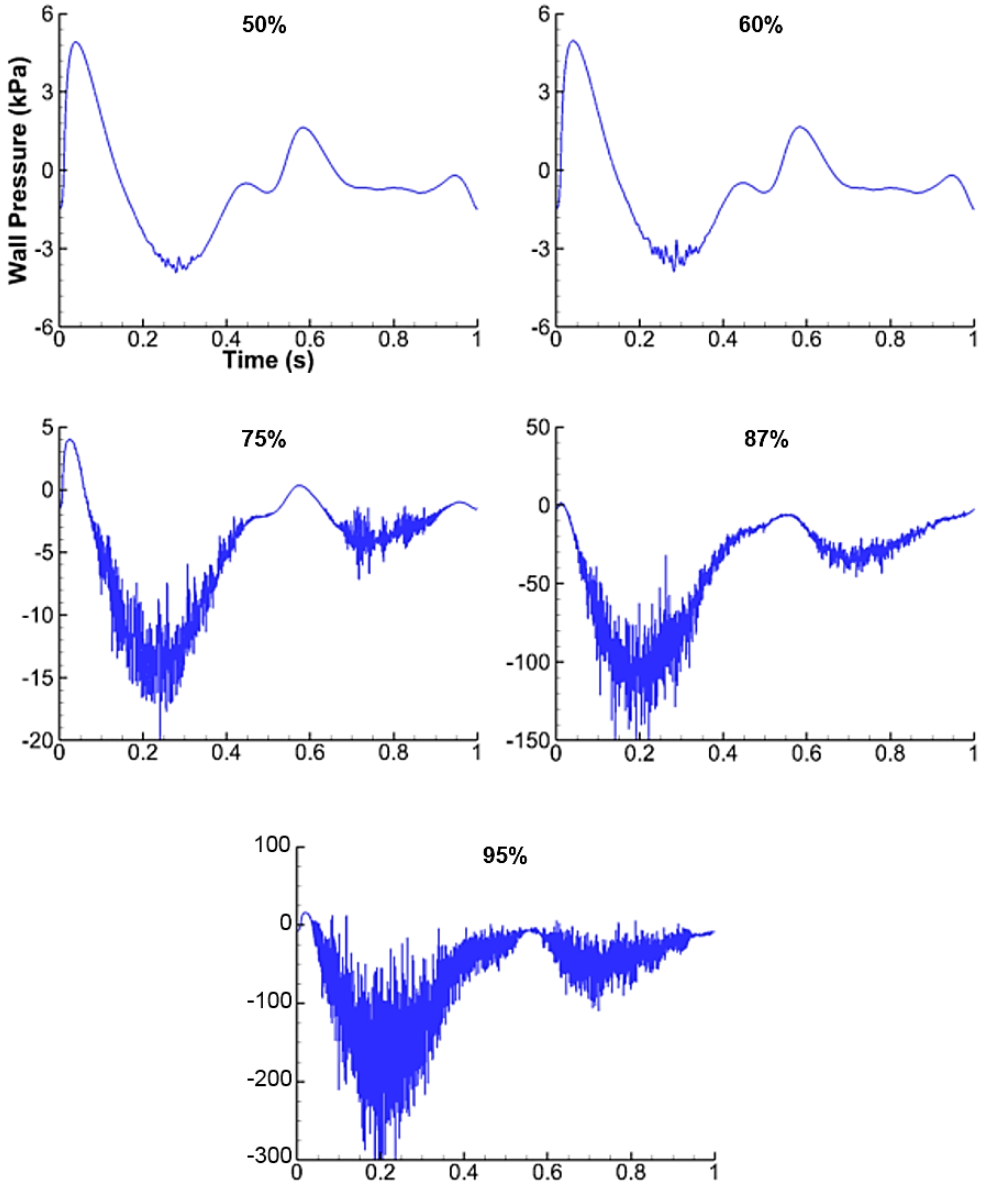


Figure 4.22. Time history of wall pressure fluctuations during one cycle for the eccentric models. The data is gathered from 90$^{o}$ position on the wall.

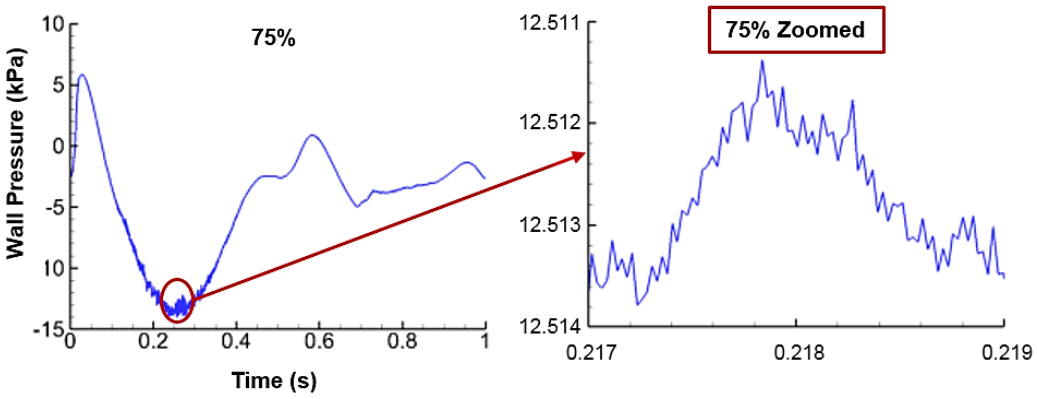


Figure 4.23. Zoomed view of wall pressure fluctuations at a certain time interval for the 75% axisymmetric model

Figure 4.24 and Figure 4.25 shows the variation of the frequency spectrum of wall pressure fluctuations, $E_{pp}$, with the Strouhal number, $St = fD/U$ for axisymmetric and eccentric models for a complete flow cycle. These plots are obtained at the maximum excitation points. The solid lines drawn on each plot are intended to show the slope of the spectrum. The frequency at which the slope changes, usually called the 'break frequency', indicates the frequency at which the energy of the pressure fluctuations turns into noise [85]. Break frequency has been identified as an important metric in auscultation-based determination of the degree of stenosis [17]. The vertical dashed lines indicate the break frequency where the slope of the energy spectrum plot changes. There is no change in the slope of the energy spectrum for the unstenosed model. This suggests that there is no turbulence activity in the healthy vascular flow and therefore no energy cascade occurs from large to small eddies. This is also valid for 50% and 60% axisymmetric cases. All other axisymmetric and eccentric cases exhibits a slope change in the spectrum which has been observed in previous experimental [21] and numerical [44] studies. In these models, the break frequency increases as the severity of stenosis increases which confirms the previous studies [17, 21, 27]. Break frequency is important for

the non-invasive diagnosis of stenosis using the sound emitted from a vessel. The higher the energy level of pressure fluctuations at break frequency at which these sounds are generated, the more the potential of them being transmitted through the arterial wall and being detectable by means of non-invasive means [36]. Based on this fact, it can be said that stenosis with higher severity emits stronger and more detectable signals. It is also seen that eccentric stenosis causes pressure fluctuations with higher energy at the breaking frequency point compared to axisymmetric cases. This suggests that eccentric stenoses generates stronger and more detectable signals than axisymmetric ones. Another important detail identified in the spectrum plots of eccentric models is the distinct peaks seen at stenosis severities of 75%, 87% and 95% which is also seen in previous numeric studies in the literature [36, 37, 99]. These peaks indicate the characteristic frequency at which the stenosis-induced murmurs are most likely to be detected.

Time-frequency spectrograms of wall pressure fluctuations at the maximum excitation points for axisymmetric and eccentric models can be seen in Figure 4.26 and Figure 4.27. These figures clearly shows that the signal intensity is higher in the systolic part of the flow than in the diastolic part. It is understood that higher stenosis severity leads to higher signal intensity and eccentricity also increases the signal level. This shows that the sound emitted from the 95% axisymmetric and eccentric models are more audible, which is consistent with the results obtained from the energy spectrum plots.

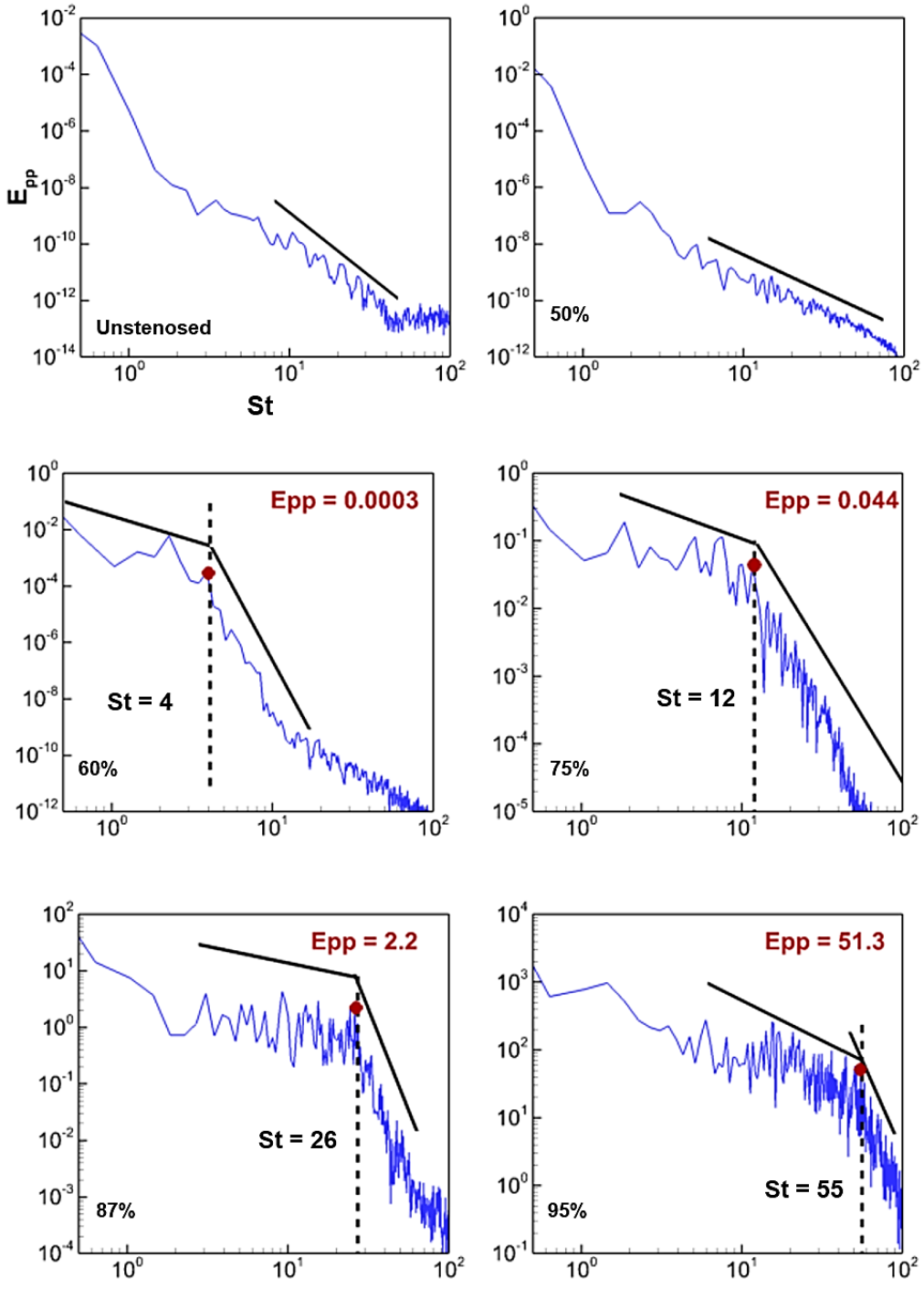


Figure 4.24. Frequency spectrum of wall pressure fluctuations for unstenosed and axisymmetric models

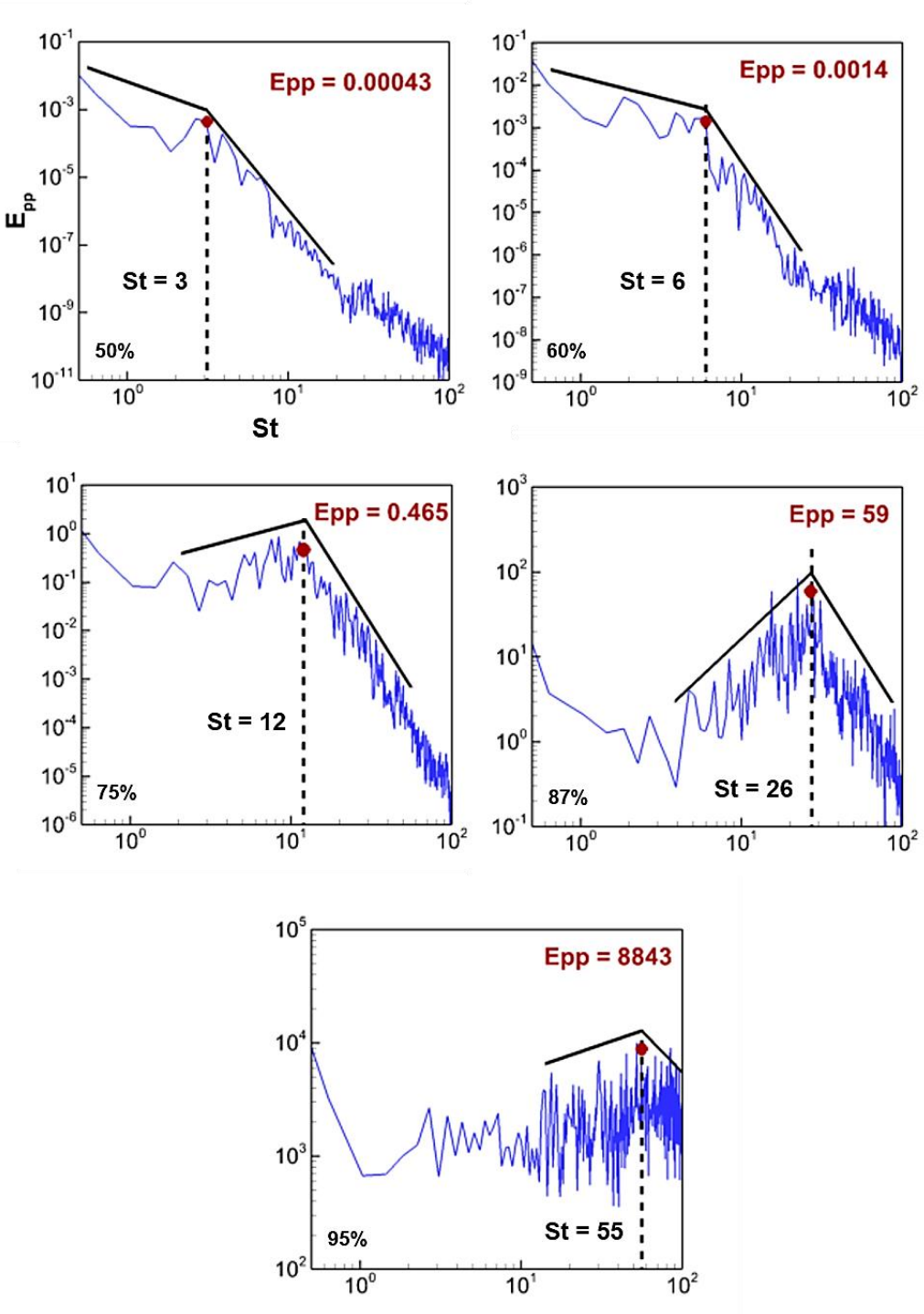


Figure 4.25. Frequency spectrum of wall pressure fluctuations for eccentric models

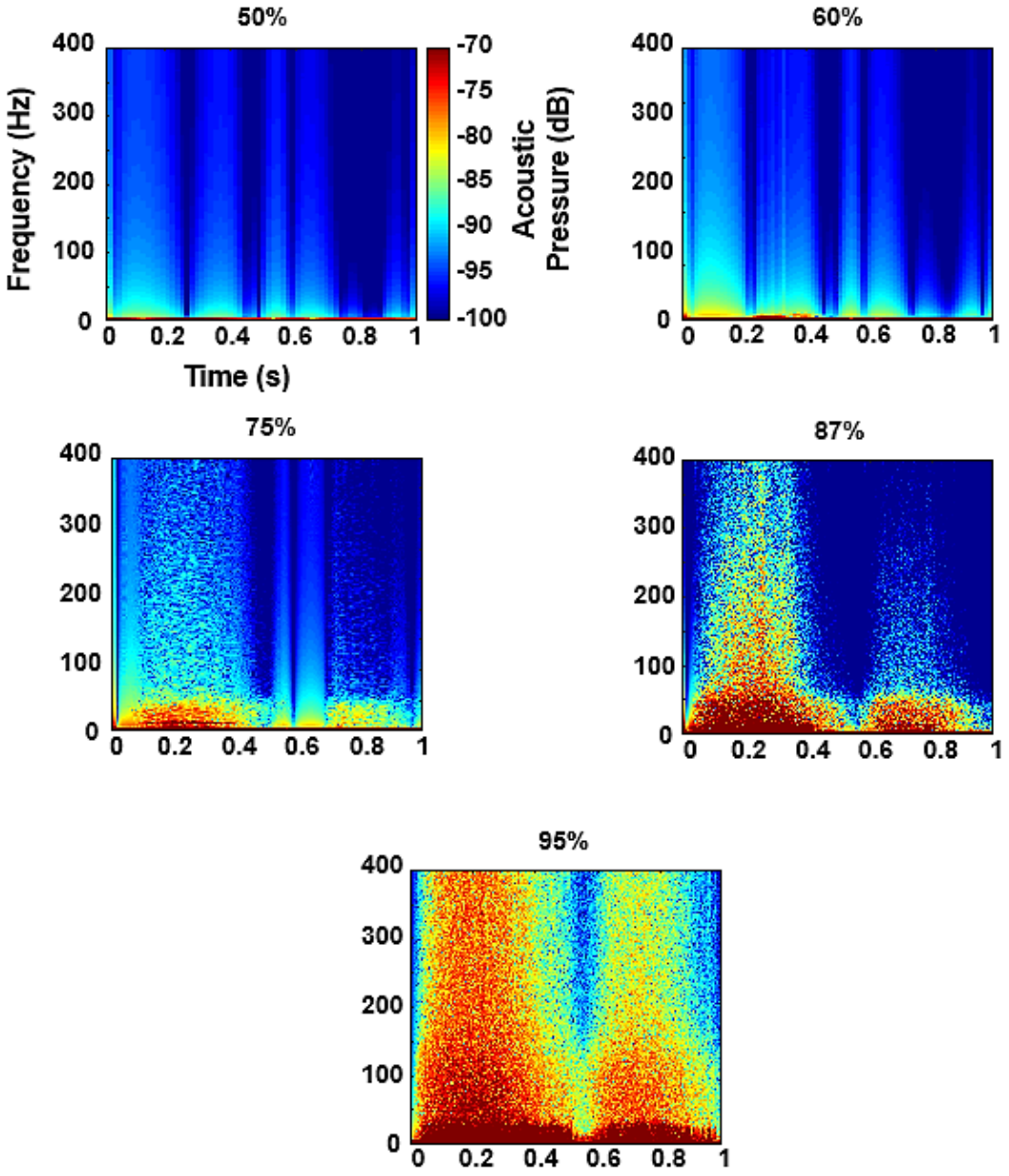


Figure 4.26. Spectrograms of wall pressure fluctuation for axisymmetric models

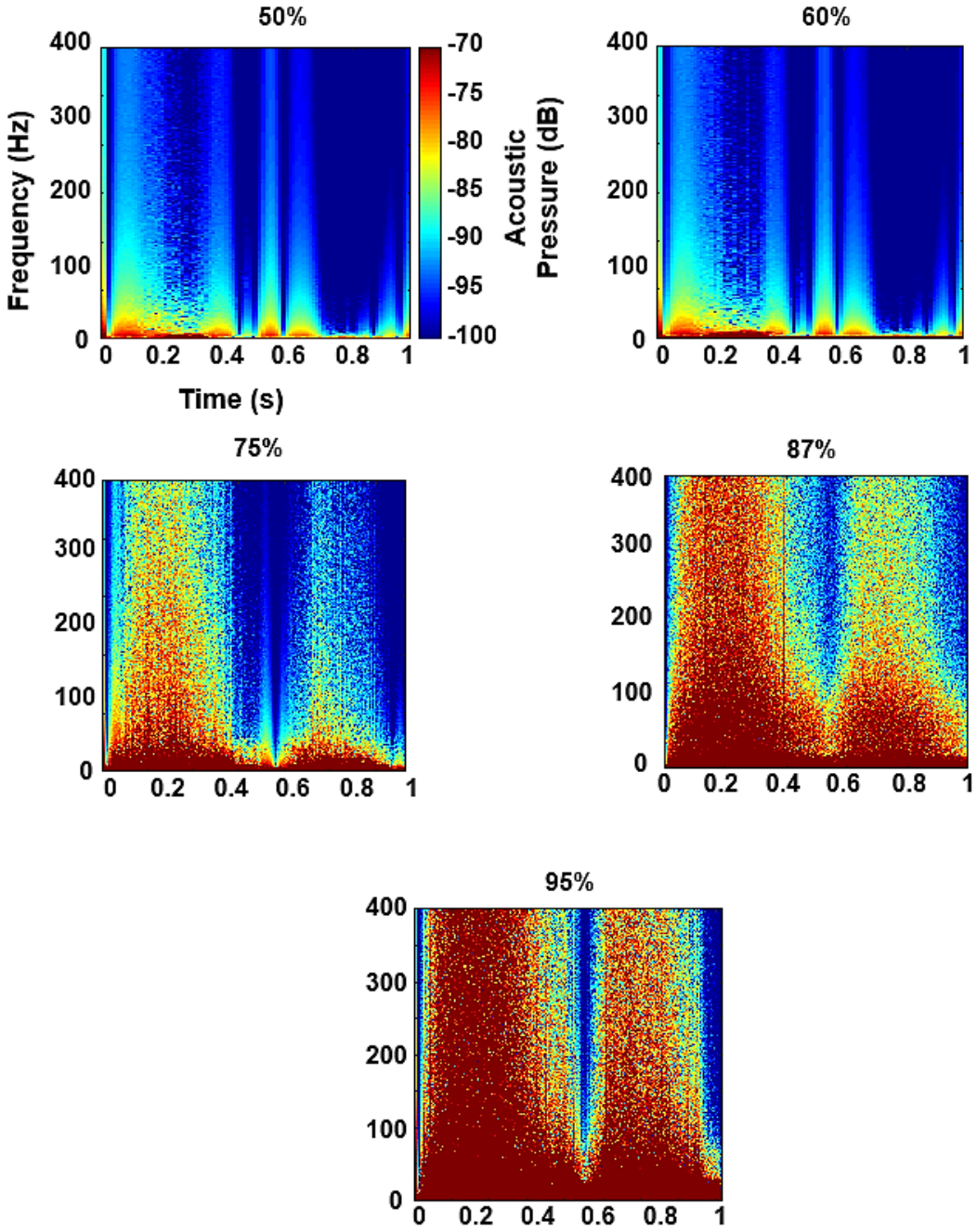


Figure 4.27. Spectrograms of wall pressure fluctuation for eccentric models

The wall pressure data obtained from the unstenosed vessel and the maximum excitation points of stenosed models are converted into sound by using `soundsc`

function of MATLAB. These sounds are different from the murmurs auscultated by a medical doctor through the skin with devices such as a stethoscope. The murmurs heard by the doctors are weakened as they spread from the vessel to the surrounding soft tissue. In addition, they become polluted by mixing with sounds generated during heartbeat and breathing. However, the sounds presented in this study are not exposed to such effects that distort their quality because they are directly obtained from inside the stenosed vessel. If a sensor technology can be developed to detect these murmurs from within the vessel, the obtained sounds can be used by the medical doctors for non-invasive diagnosis of the vascular stenosis. Generated sound files are attached to this thesis.

It is seen that the intensity of the sound emitted from the stenosed models is directly related to the fluctuation magnitude of the wall pressure. Accordingly, sounds generated by 50% and 60% are almost same with that of unstenosed vessel. Sounds that are called murmurs by the clinicians which are considered to be signs of vascular stenosis have obtained from models with severity of 75% and above. This is consistent with the studies in the literature showing that the critical degree of stenosis for considerable turbulence effects is 75% [65]. The sound levels are the highest for the 95% axisymmetric and eccentric models. It is known that the actual sound patterns obtained by Doppler ultrasonography, which is used to detect stenosed vessels, transform from triphasic configuration, heard in healthy vessels, to biphasic or monophasic configurations according to the severity of the stenosis [55]. This is actually the case for the sounds obtained from the current simulations. Once again it is important to note that these results can only be obtained with pulsatile simulations.

When the findings obtained are evaluated from a diagnostic point of view, it is seen that if the sounds emitted from stenosed vessels can be listened from inside the artery, these sounds can give important information about the severity and eccentricity of the stenosed region. These information can be used clinically to

detect the presence and severity of stenosis non-invasively. In this sense, this study aims to provide a valuable contribution to the literature.

### 4.4 Conclusion

Numerical and experimental studies in the literature investigating the flow through a stenotic vessel include studies (although few in number) that examine the effect of stenosis severity and eccentricity on the post-stenosis flow regime. Among these studies, there are methods developed to determine the risk factor related with severity of stenosis by acoustic based techniques. However, these methods have only been used as a pre-diagnosis tool for conventional invasive diagnostic operations. Therefore, there are studies that need to be done for the detection of stenosed vessels by non-invasive diagnostic methods. The present study is conducted to make a valuable contribution to the literature from this aspect by investigating the effect of different stenosis severities and eccentric morphology on the sound emitting from stenosed vessels. For this purpose, numerical simulations are conducted by using axisymmetric and eccentric forms of five different stenosis severities. In these simulations, physiological pulsatile flow as the inlet flow condition and non-Newtonian blood model as the fluid are used.

According to the mean axial velocity profiles at the maximum velocity instant of the pulsatile flow the length of the region where the flow is fully developed decreases with increasing severity of stenosis for axisymmetric cases. Eccentricity, leads to an increase in this length for each stenosis severity. Increased stenosis severity leads to a higher mean wall pressure drop at the post-stenotic region. These values are lower for eccentric models than axisymmetric models. On the other hand, increasing stenosis severity has increased turbulence activity and acoustic pressure intensities in the post-stenotic region. Eccentricity carries the position of maximum excitation point at post stenotic region further away when compared with axisymmetric cases.

The wall pressure data obtained for a pulsatile flow cycle from the maximum activity points showed that higher stenosis severity means higher pressure fluctuation intensity, break frequency, acoustic signal strength and sound level of the murmurs. For the eccentric cases, the location where the pressure data is collected becomes important. Amplitude of pressure fluctuation intensity, acoustic signal strength and sound level of the murmurs at the vessel wall where the flow jet is directed to are considerably higher than that of axisymmetric models for the same stenosis severity.

The sounds emitted from the stenosed vessels can provide important information about the severity and morphology of the stenosed region. For this purpose, a sensor technology may be developed to measure these sounds from within the stenosed artery. These murmurs can be listened by the doctors and used for the purpose of non-invasive diagnosis of stenosis.

# CHAPTER 5

# EFFECT OF STENOSIS SHAPE ON THE SOUND EMITTED FROM A STENOSED BLOOD VESSEL

## 5.1 Introduction

Studies that examine the effect of different severities on stenotic flow using a single stenosis shape constitute the majority of this area as can be understood from the literature review in chapter 1. However, the shape of the plaque causing the stenosis in the blood vessel wall is not in a single form. Stenosis shape is also considered as an important parameter that affect the blood flow [100, 101] and the studies in this chapter are focused on this parameter.

As stated in the previous chapters early diagnosis of vascular stenosis is of great importance and one of the methods that can be used for this purpose is to record and analyze the sound emerging from the stenosed blood vessel. However, the studies conducted for acoustic-based diagnosis of vascular stenosis mostly performed using a single stenosis shape and one or more severity ratios as mentioned in chapter 1. Along with that, there are studies in the literature that consider the effect of stenosis shape on the characteristics of blood flow from different aspects.

Existing literature has shown that the emerging sound contains valuable information about the stenotic region. However, more work needs to be done for investigating the effect of the stenosis shape on the sound emerging from the blood vessel. The study in this chapter is carried out to contribute in this aspect for the purpose of non-invasive diagnosis of atherosclerosis. In the following section, the

geometrical models with different stenosis shapes, computational grids and simulation settings are described. Results about the effect of stenosis shapes on the post-stenotic flow field and acoustic radiation are presented and discussed in the next section.

## 5.2 Computational Model

Vascular stenoses may have many different shapes, as seen in Figure 5.1 [102, 103, 104, 105]. Based on these and other similar images, six idealized stenosed vessel models, shown in Figure 5.2, are created. They are all based on a real healthy femoral artery of 6.4 mm diameter ($D$). For all models, pre- and post-stenosis vessel lengths are 37.2 mm and 100 mm, respectively. The length of the stenosis region is $1D$ for the short model and $2D$ for all others. The severity of the stenosis is taken as 87% throughout the study. Elliptical stenosis is commonly used in previous numerical studies [37, 67, 85], and taken as the base case here. Short stenosis is used to study the effect of the stenosis length. High and low slope models are used to understand the role of the distance of the throat to the exit of the stenosis. The existence of double throats and the irregularity it brings is studied by the overlapping model and finally the asymmetric model is used to understand the effect of radial asymmetry.

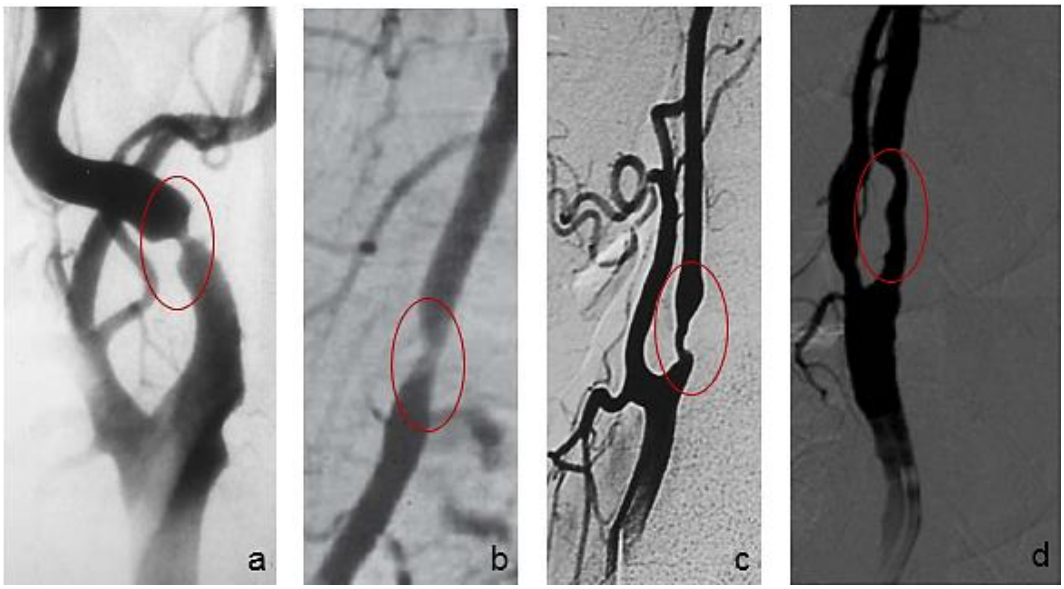


Figure 5.1. Examples of realistic stenosis geometries (a) [102] (b) [103] (c) [104] (d) [105]

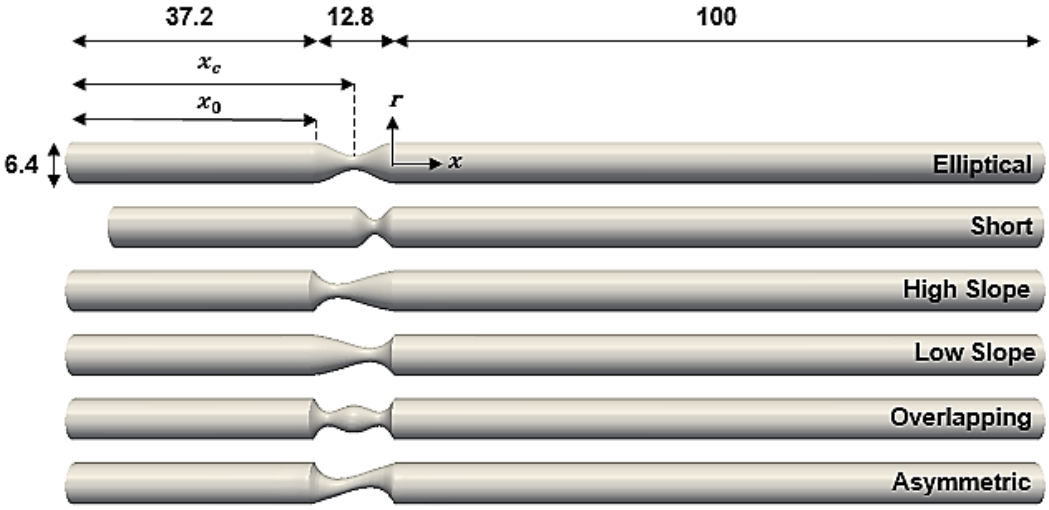


Figure 5.2. Vessel models with different stenosis shapes. Flow is from left to right. Figure is out of scale and dimensions are in mm.

Elliptical and short stenoses are defined as follows [39]

$$r(x) = \frac{1}{2}D\left[1 - s_c\left(1 + \cos\left(\frac{2\pi(x - x_c)}{L}\right)\right)\right] \tag{5.1}$$

where $D$ is the diameter of the non-stenosed vessel, $s_c$ = 0.32 for the 87% stenosis, $L$ is the length of the stenotic region and $x_c$ is the location of the centre of the stenosis. High and low slope stenoses are defined by [106]

$$r(x) = \frac{1}{2}D\left[1 - A\left(L^{(m-1)}(x - x_0) - (x - x_0)^m\right)\right] \tag{5.2}$$

where $x_0$ is the location of starting point of the stenosis, $m$ is the shape parameter which is taken as 1.5 and 6 for the high and low slope models, respectively, and parameter $A$ is given by

$$A = \frac{2\delta}{DL^m}\frac{m^{m/(m-1)}}{(m-1)} \tag{5.3}$$

where $\delta$ denotes the maximum height of stenosis at $x = x_0 + L/m^{1/(m-1)}$ and equal to $\delta = 3.2 - 1.15 = 2.05\,mm$ for 87% stenosis. Overlapping stenosis is defined as [107]

$$\begin{aligned} r(x) = \frac{1}{2}D\Big[1 - \frac{3}{2}\frac{2\delta}{DL^4}(11(x - x_0)L^3 - 47(x - x_0)^2L^2 \\ + 72(x - x_0)^3L - 36(x - x_0)^4)\Big] \end{aligned} \tag{5.4}$$

and the asymmetric model is a combination of high and low slope models.

Bird-Carreau non-Newtonian blood model [96] defined by equation (4.3) is used as fluid in simulations. The fully developed physiological pulsatile flow profile details of which are specified in chapter 4.2 is used at the inlet. Reference pressure at the outlet is set to zero and the no slip boundary condition is used at the wall boundaries, which are taken to be rigid.

The incompressible flow solver, turbulence model and discretization schemes used in this chapter are the same as those used in the previous chapters. To understand the dependency of the solutions on the time step, preliminary simulations are conducted. Results are compared in terms of mean and fluctuating wall pressures and $\max(Co) = 1$ is found to be satisfactory. With this setting, time step varies between $4.6 \times 10^{-6}$ s and $2.2 \times 10^{-5}$ s during the simulation of the elliptical stenosis model.

Mesh independence study is performed for the elliptical model using the four different meshes given in Table 5.1. All meshes use a similar grid structure to that used in chapter 4. $y^+ < 1$ condition holds for all the meshes used in this chapter. Mesh independence is checked with the mean wall pressure variation shown in Figure 5.3, as well as the acoustic pressure distribution obtained by using wall pressure fluctuations in Figure 5.4 and frequency contents of the acoustic pressures at $x$ = 10 mm in Figure 5.5. After these comparisons, Mesh 3 is evaluated to be suitable and applied to all other models to obtain the results presented in this chapter. In the simulation conducted with this mesh and the elliptical model, the minimum Kolmogorov length scale is obtained as 0.0205 mm immediately after the stenotic region where the maximum cell size is around 0.3 mm. Therefore, the ratio of cell size to the Kolmogorov length scale is kept below below 14.65, which is below the maximum allowable range of 20-40 given in the literature [81]. The two other metrics are also calculated to check the suitability of mesh resolution. The highest $LES\_M$ value at the post-stenotic region is found as 0.041 for the elliptical model. Moreover, the lowest $LES\_IQ$ value is detected as 0.888 at post-stenotic region of the elliptical model. The simulations conducted by using Mesh 3 lasts approximately 4 pulses for the overlapping and high slope models and 3 pulses for the others to reach the time periodic state in terms of mean flow parameters. As the base case, the wall clock time to reach time periodic state is almost 14 days for elliptical model on 24 cores of the TRUBA HPC system of TÜBİTAK ULAKBİM High Performance and Grid Computing Center.

Table 5.1. Details of meshes used in mesh independence simulations of elliptical model

| | # of Nodes | # of Cells |
|---|---|---|
| **Mesh 1** | 163560 | 172846 |
| **Mesh 2** | 1100712 | 1121618 |
| **Mesh 3** | 2038452 | 2066734 |
| **Mesh 4** | 4099376 | 4147262 |

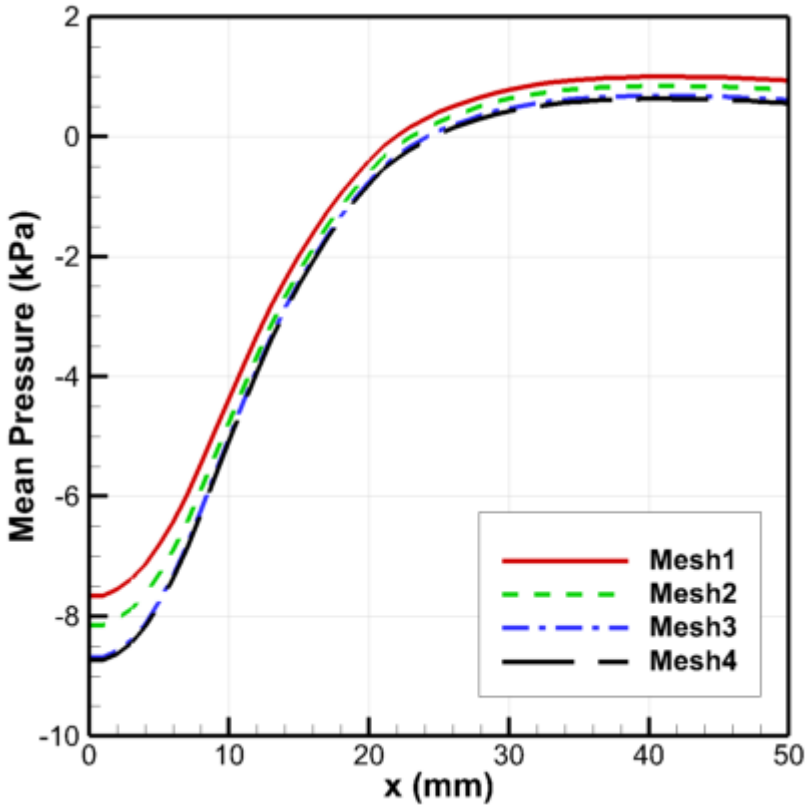


Figure 5.3. Mean wall pressures obtained with four different meshes for the elliptical model

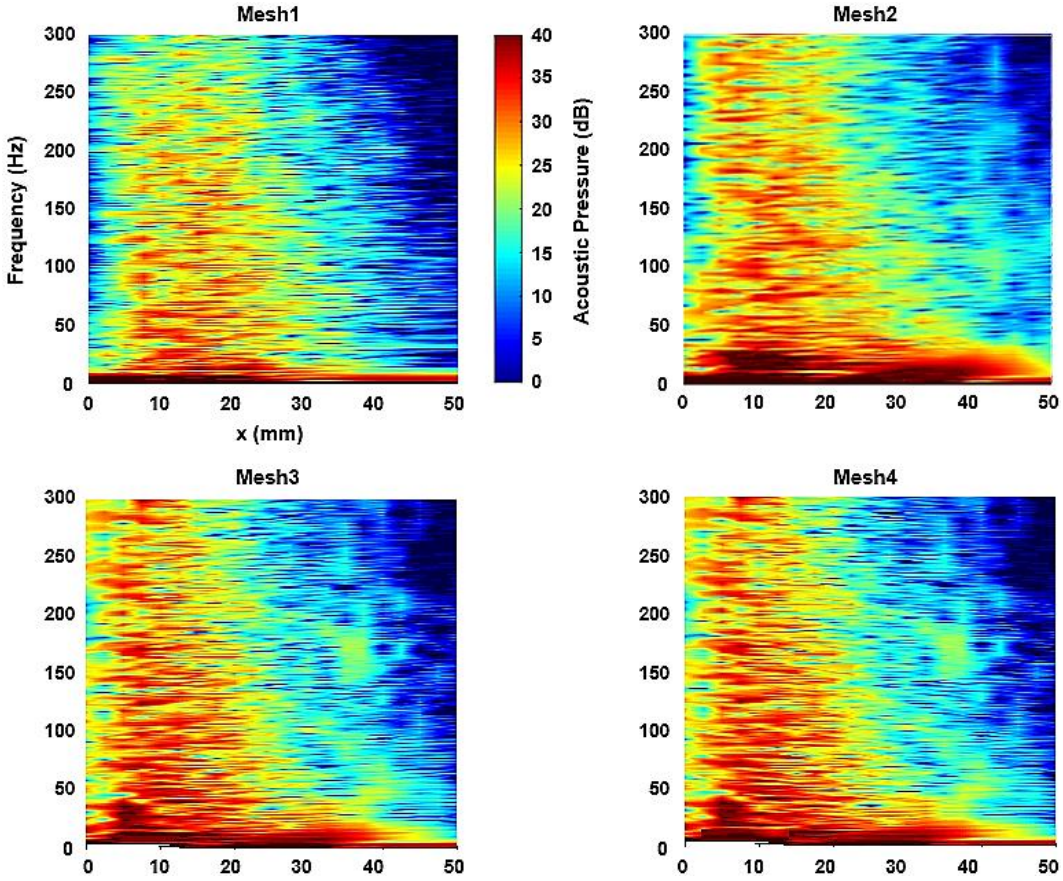


Figure 5.4. Acoustic pressure contours obtained with four different meshes for the elliptical model

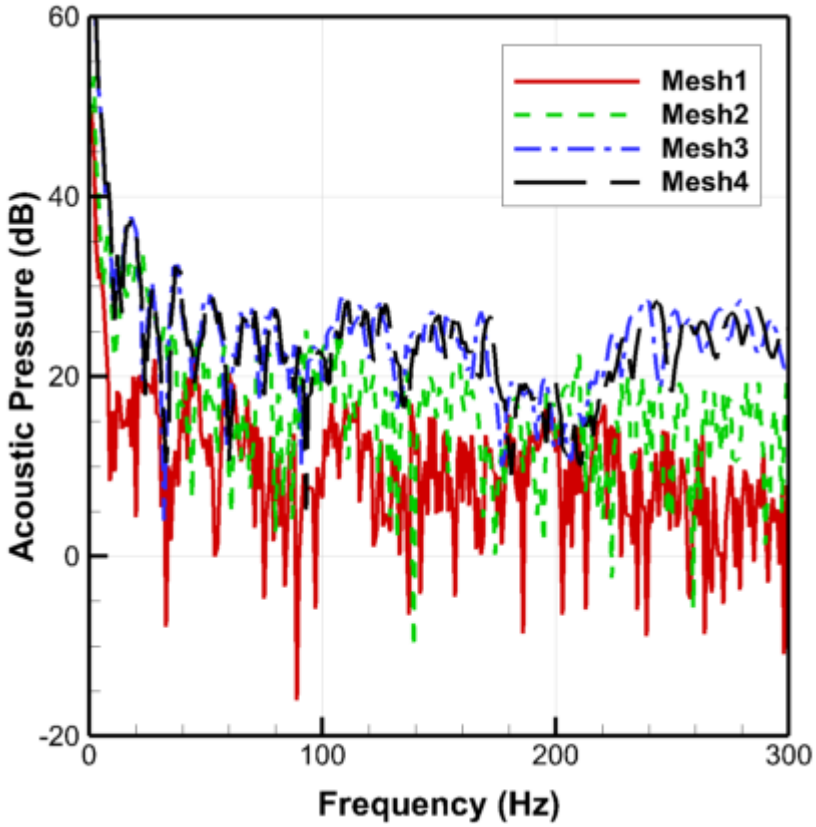


Figure 5.5. Frequency contents of the acoustic pressures for the axisymmetric elliptical model at $x$ = 10 mm obtained with four different meshes

### 5.3 Results and Discussion

All the results presented in this section are obtained after the flow reaches the time periodic state in terms of mean flow parameters. Mean axial velocity profiles at the maximum flow instant (P2) are shown in Figure 5.6. Note that velocity is non-dimensionalized by $U_{\max} = 1.246$ m/s, which is the maximum value of the pulsatile flow profile at the inlet. According to this figure, the jet created by the stenosis affects the downstream flow up to a distance of roughly 5$D$ for short, high slope and consecutive models. For the others, this distance extends to 6$D$ approximately. Fully developed mean flow conditions are observed after these lengths.

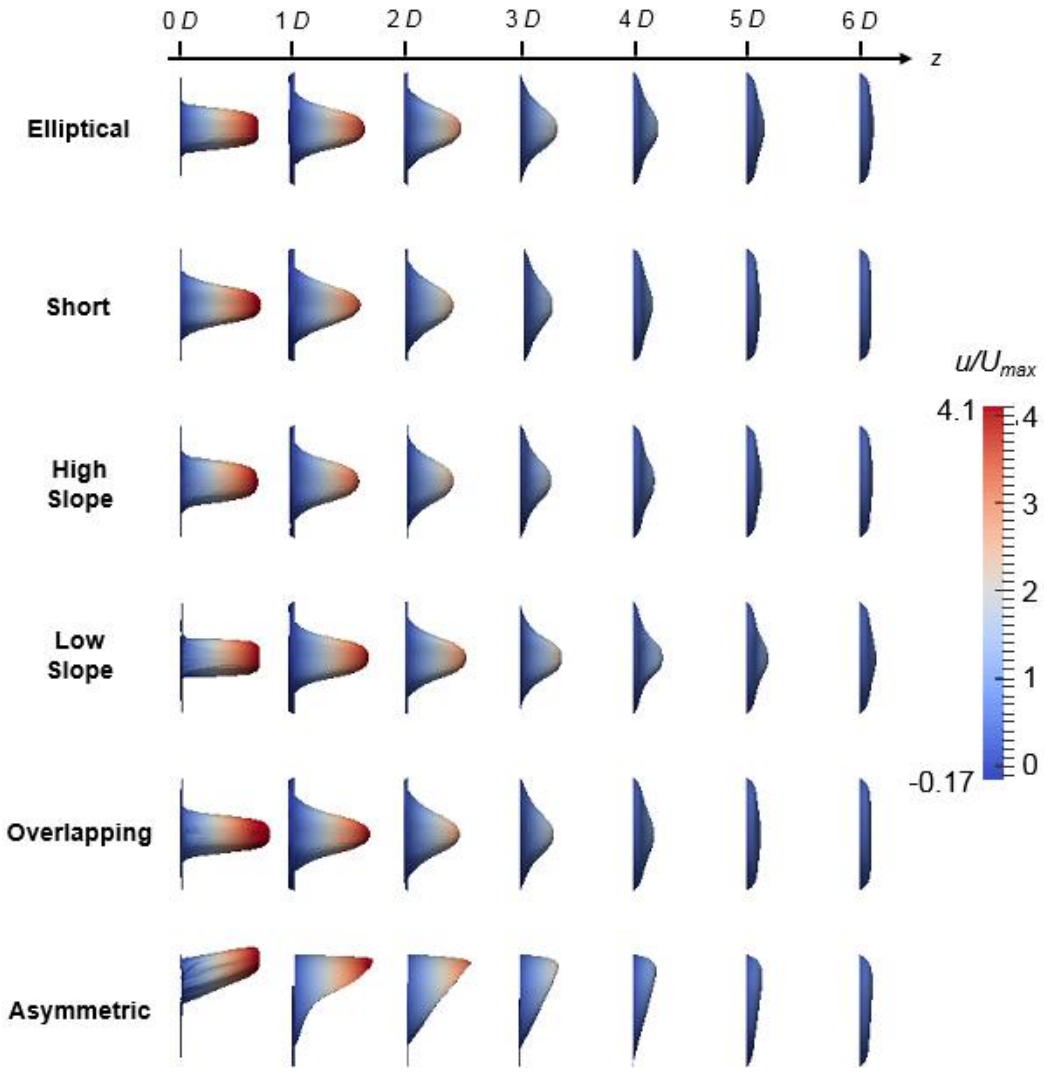


Figure 5.6. Non-dimensional mean axial velocity profiles after the stenosis exit

Figure 5.7 shows the variation of the mean pressure along the vessel wall after the stenosis at the maximum flow instant (P2). For the asymmetric model this data is extracted along three different lines on the wall as shown in Figure 3.11. The drop of wall pressure between stenosis exit and the exit of the flow domain is about 9 kPa for high slope and overlapping models, 8.5 kPa for elliptical and short models, 8 kPa for low slope model and 6.5 kPa for asymmetric model. It should be noted that pressure drop value is independent of data collection position on the wall for

asymmetric model. It has been found in the literature that the mean pressure drop at post-stenotic region affects turbulent wall pressure fluctuations [98]. Therefore, it may be expected that the models that will reveal the most wall pressure fluctuations after stenosis are high slope and overlapping models. On the other hand, the asymmetric model may be expected to show the opposite effect.

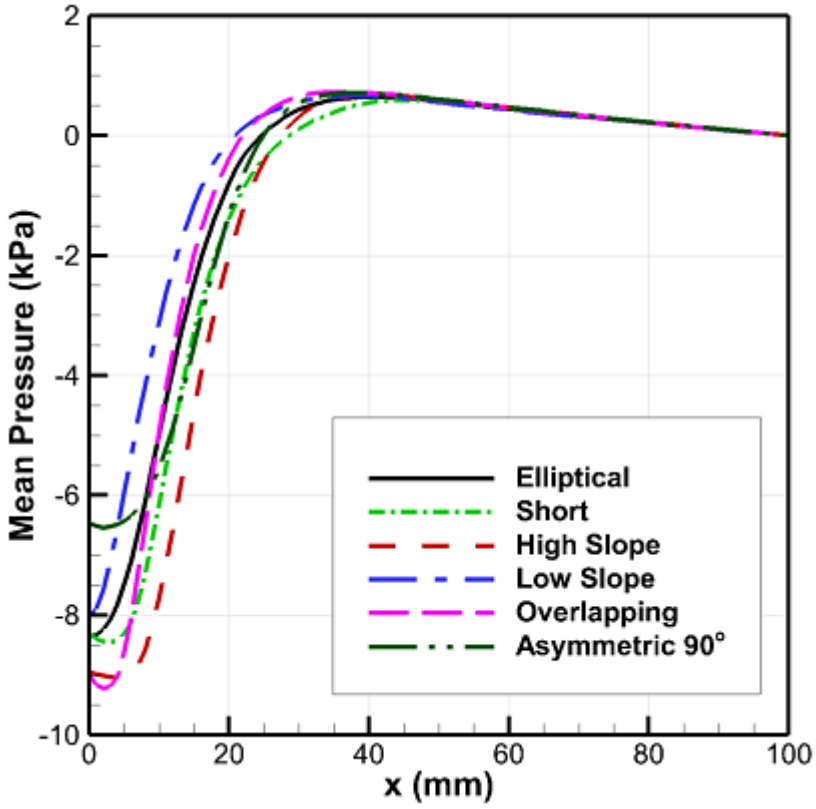


Figure 5.7. Mean wall pressures along the wall for different stenosis shapes

Figure 5.8 presents the TKE along the centerline of the flow jet core. This corresponds to the centerline of the vessel for the axisymmetric models and 2.05 mm above it for the asymmetric model. The TKE values in this plot is given at phase P2 and normalized by $(U_{max})^2$. This plot can be considered as a measure of the turbulent activity. Figure 5.8 indicates that TKE reaches the highest level at

post-stenotic region within a distance of approximately $x$ = 2.5 mm for high slope and overlapping models and $x$ = 5 mm for elliptical model. These values are followed by short and low slope models with $x$ = 10 mm after the stenosis exit. The furthest distance is found in the asymmetric model as $x$ = 12.5 mm. Then TKE decays gradually as the flow is re-laminarized. Overlapping model leads to a TKE rise of 1.2 and 1.3 times at the highest levels when compared with high slope and rest of the models, respectively. These results demonstrate the effect of the presence of overlapping and proximity of the stenosis throat to the stenosis entrance on the level of turbulence activity.

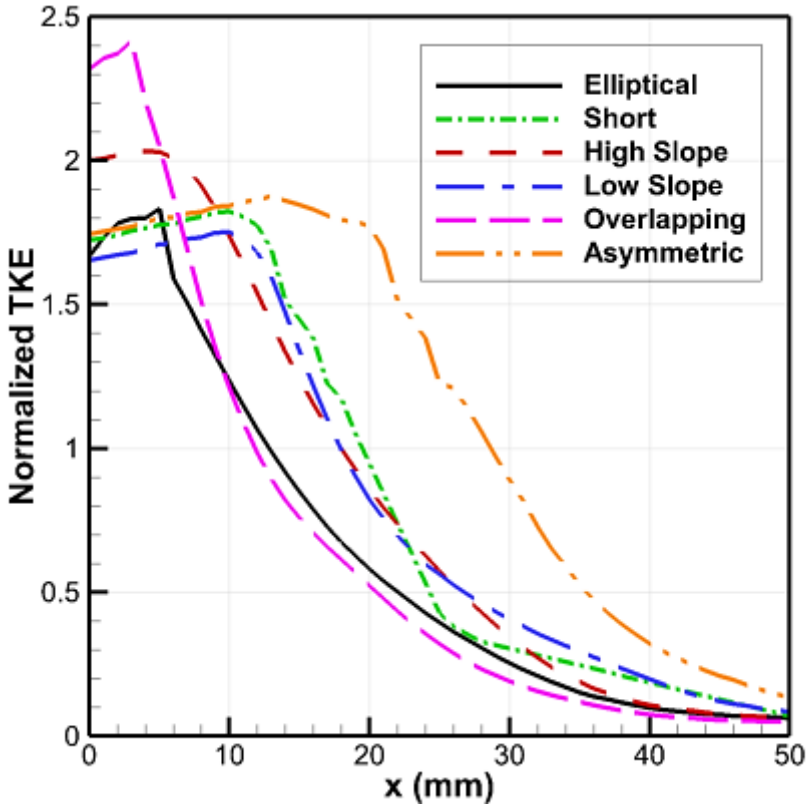


Figure 5.8. Normalized TKE along the stenosis centreline for different stenosis shapes

In Figure 5.9 instantaneous coherent structures at the instant of maximum flow velocity is visualized by means of vorticity magnitude normalized by $(U_{max}/D)$. It is seen that the flow jet is considerably shortened and transformed almost immediately to vortical structures just at the exit of the stenosis in the case of high slope and overlapping models. For the other models the transformation occurs after a certain distance from the stenosis exit.

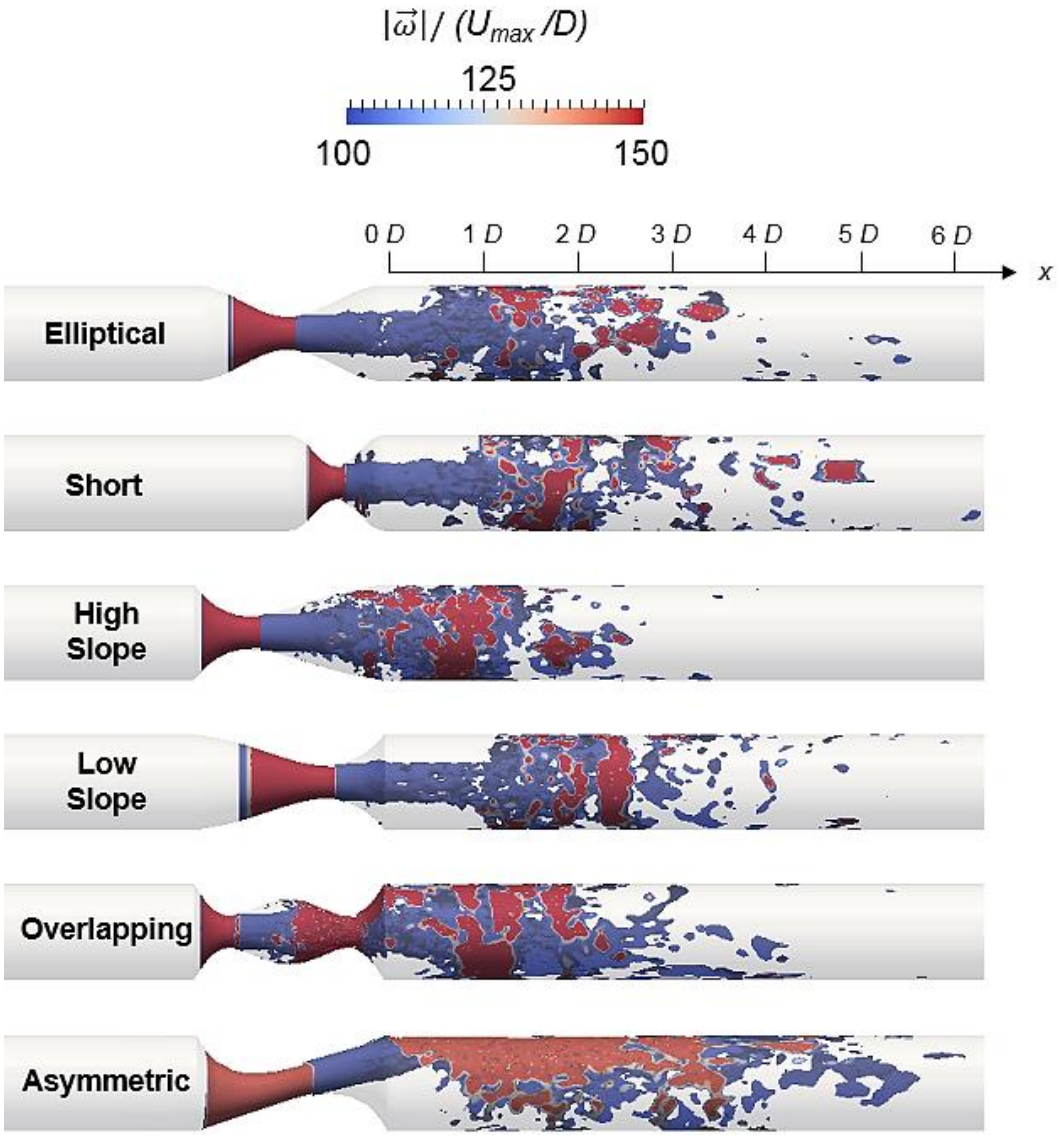


Figure 5.9. Coherent structures colored by instantaneous normalized vorticity magnitude

Acoustic pressure contours obtained by converting the wall pressure data gathered in the simulations into logarithmic scale after the procedure explained in Chapter 3.3. These pressure data collected during a pulsatile flow cycle at 41 nodes along the vessel wall with a sampling frequency of 5000 Hz as the flow reaches time periodic state in terms of mean flow parameters. The mentioned contours for an unstenosed vessel and for vessels with different stenosis models are given in Figure 5.10. Acoustic pressure calculated for the unstenosed vessel is very different in terms of spectral behavior than those with stenosis. For the unstenosed model, pressure decreases monotonically in the axial direction. However, for the models with stenosis, acoustic pressure makes a clear peak in the post-stenotic region. When the stenosed vessels are compared, it can be said that the length of region with higher acoustic activity is shorter for high slope and overlapping stenosis models for higher frequency levels.

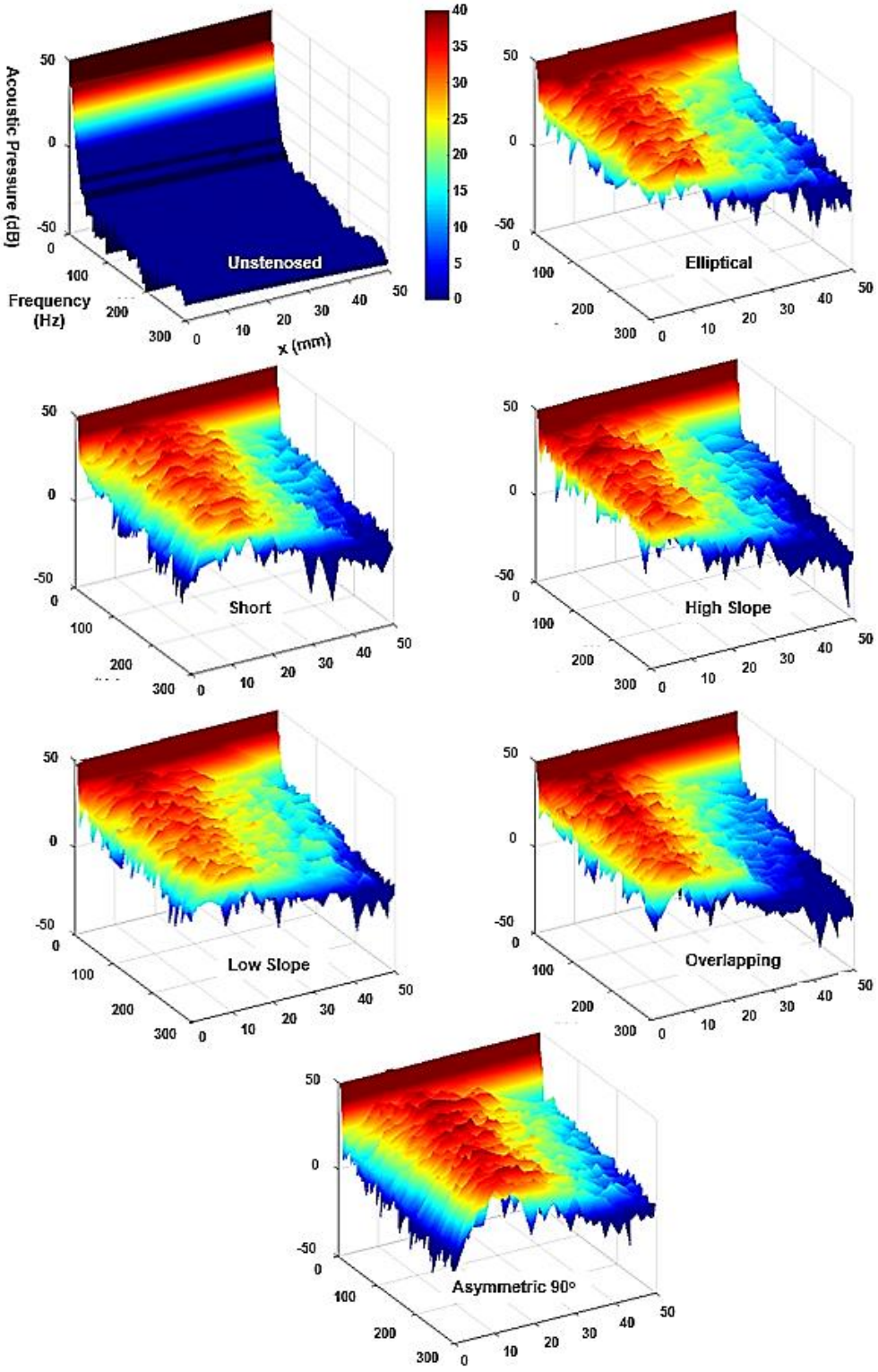


Figure 5.10. Acoustic pressure content for different stenosis shapes

In addition, to study the maximum excitation location of different models, axial variation of the RMS of wall pressure fluctuations, $p'_{RMS}$, is plotted in Figure 5.11. Overlapping and the shortening of the distance of the stenosis throat to the stenosis entrance increases the magnitude of the pressure oscillations, whereas the asymmetry creates a contrary effect. $p'_{RMS}$ reaches maximum value just at $x$ = 2.5 mm for high slope and overlapping models and 5 mm after stenosis for elliptical shape. Maximum level is reached at $x$ = 10 mm for short and low slope models and $x$ = 12.5 mm for asymmetric model. These values are compatible with ones given in TKE and enstrophy results. These positions indicate where acoustic signals propagate most strongly at post-stenotic region. It should be noted that that the pressure oscillation intensities are found to be equivalent in all regions of the vessel wall for the asymmetric model.

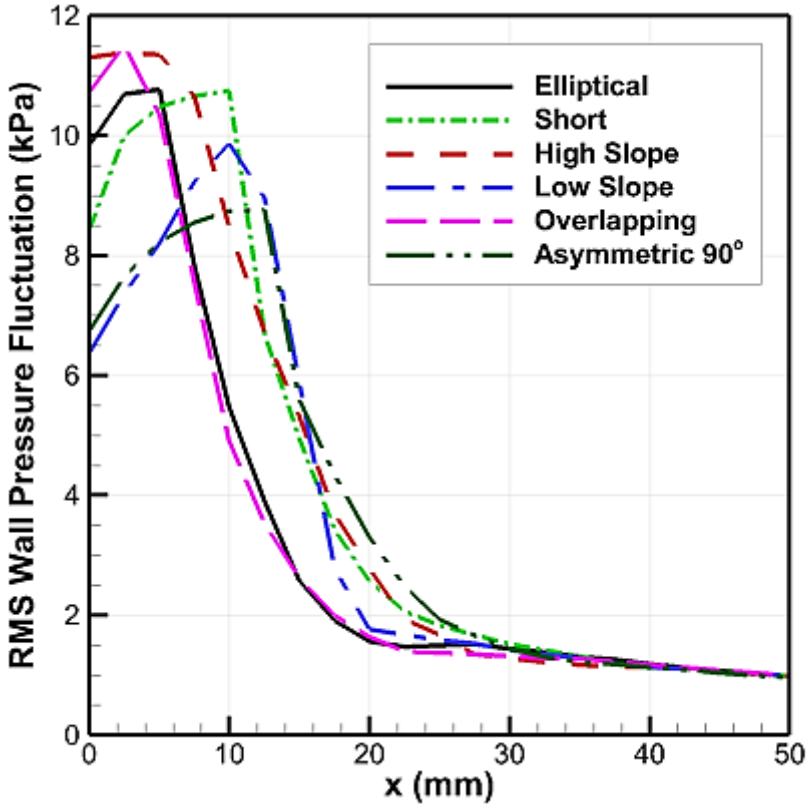


Figure 5.11. Axial variation of the RMS wall pressure fluctuations

Figure 5.12 shows the time history of wall pressure fluctuations obtained for the unstenosed and stenosed models at the maximum excitation points aforementioned above. For the asymmetric model, data are collected from the three points given in Figure 3.11 and the results are found to be the same. For this reason, only the result of the vessel wall region where the flow jet directed is presented. The pressure obtained from the wall of the unstenosed vessel does not contain any fluctuations because the flow remains in the laminar regime. On the other hand, pressure fluctuations due to turbulence are observed in all stenosed models. Maximum fluctuation activity is observed in the overlapping and high slope models. Both the fluctuation frequency and the magnitude are higher for these models. Asymmetric stenosis leads to lower fluctuation frequency and magnitude than all other models. It is also seen that the stenosis shape affects the extent in which the pressure fluctuations are intense during the pulsatile cycle. It is seen that the fluctuations for the high slope and consecutive stenosis models are intense during the P1, P2 and P3 phases, while they are limited to the P2 and P3 phases in other axisymmetric models and only to the P2 phase for the asymmetric one. These differences can be seen more clearly in the systolic part of the flow than in the diastolic part. It is seen that for all the models, the most intense pressure fluctuations are detected close to the maximum velocity instance. Clinically, this shows that it is easier to detect acoustic signals due to pressure fluctuations during heart contraction. The diastole phase exhibits a cleaner graph in terms of pressure fluctuations for all models. Here it is important to note that these findings and the differences between the results of various models can only be obtained with pulsatile simulations.

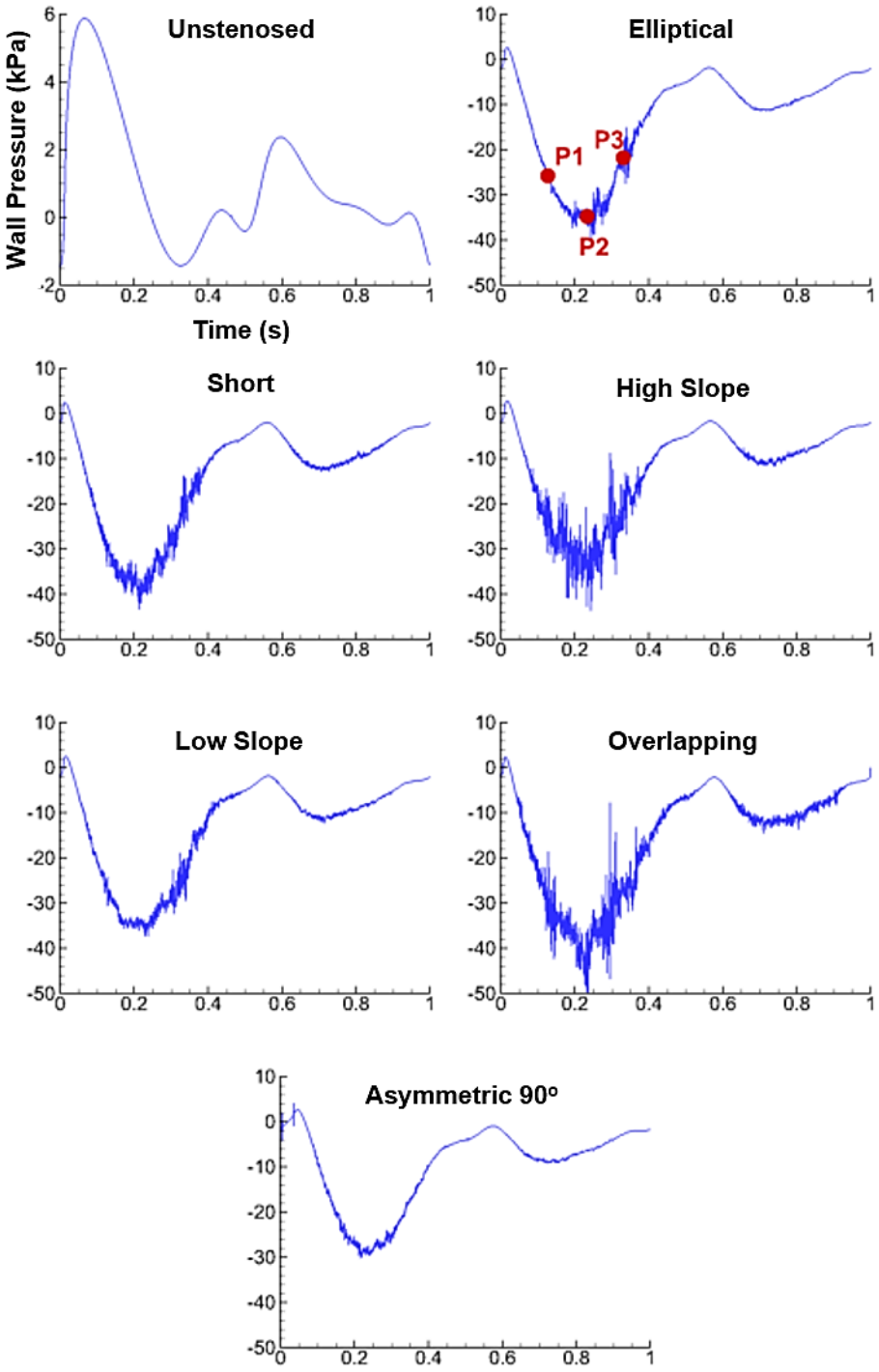


Figure 5.12. Time history of wall pressure fluctuations during one cycle at the maximum excitation points

Figure 5.13 shows the variation of frequency spectrum of wall pressure fluctuations, $E_{pp}$, with the Strouhal number, $St = fD/U$ for unstenosed and stenosed models for a complete flow cycle. These plots are obtained at the maximum excitation points. The solid lines drawn on each plot are intended to show the slope of the spectrum. The frequency at which the slope changes, usually called the 'break frequency', indicates the frequency at which the energy of the pressure fluctuations turns into noise [85]. Break frequency has been identified as an important metric in auscultation-based determination of the stenosis severity [17]. There is no change in the slope of the energy spectrum for the unstenosed vessel. This suggests that there is no turbulence activity in the healthy vascular flow and therefore no energy cascade occurs from large to small eddies. Break frequency is important for the non-invasive diagnosis of stenosis using the sound emitted from a vessel. These plots show that different stenosis shapes can change the value of the break frequency even if they have the same stenosis severity. Accordingly, it can be seen that short, high slope and overlapping stenosis models increase the break frequency level. However, asymmetric stenosis model generates a contrary effect. The higher the energy level of pressure fluctuations at break frequency at which these sounds are generated, the more the potential of them being transmitted through the arterial wall and being detectable by means of non-invasive means [36]. Based on this fact, it can be said that high slope and overlapping stenosis emits stronger and more detectable signals, where the situation is the opposite for the asymmetric model.

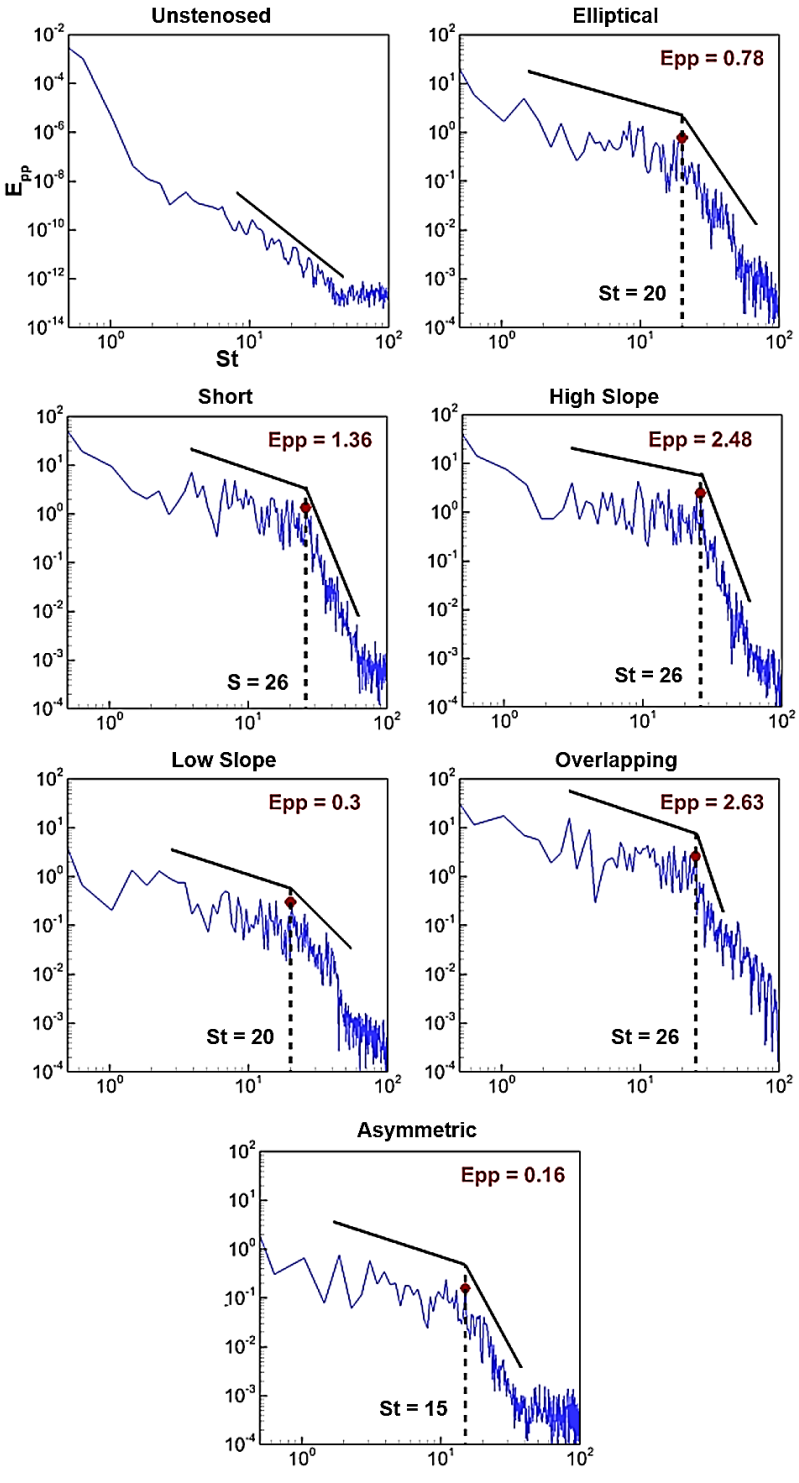


Figure 5.13.Frequency spectrum of wall pressure fluctuations for a pulsatile flow cycle

Time-frequency spectrograms of wall pressure fluctuations at the maximum excitation points for each model can be seen in Figure 5.14.

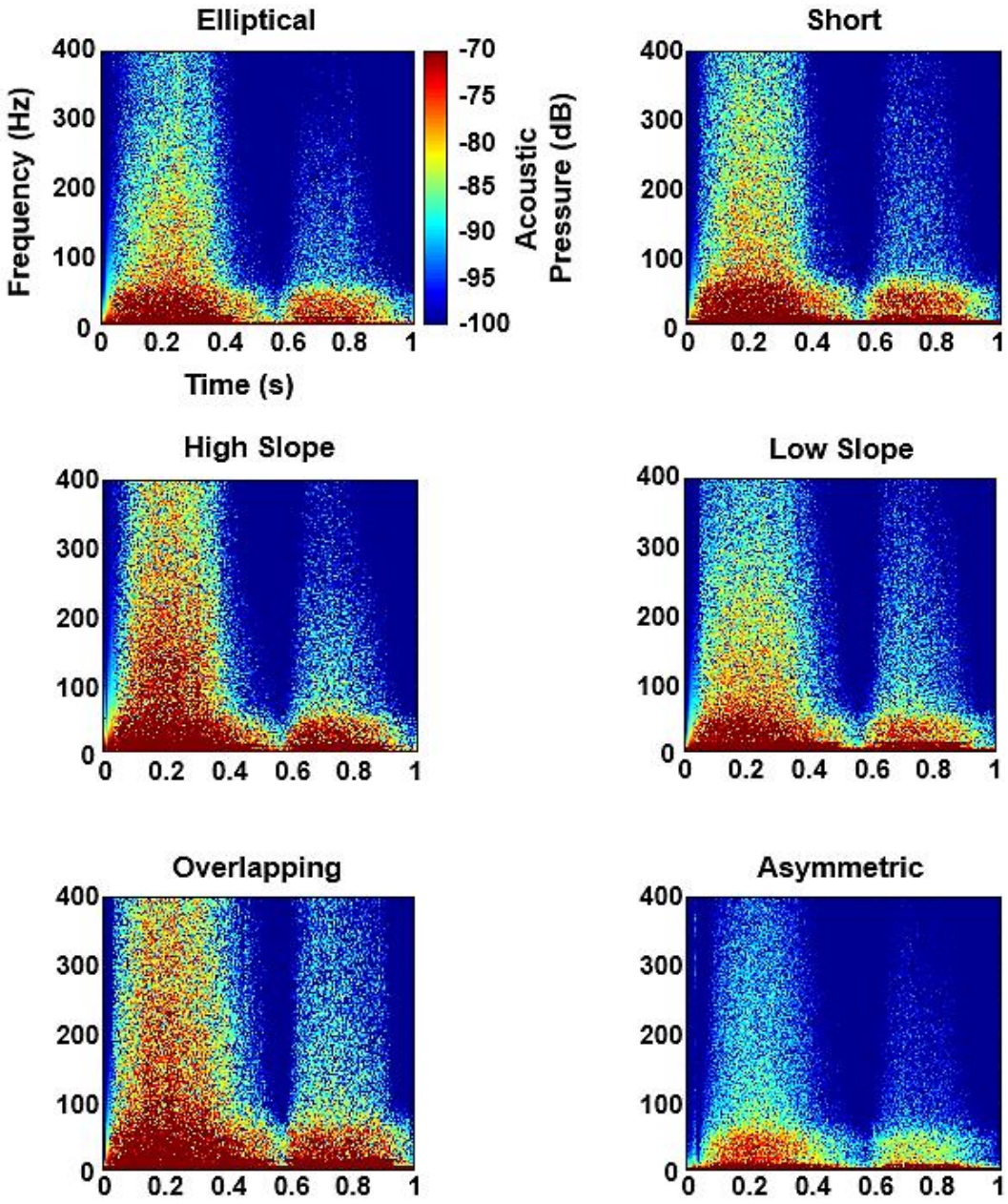


Figure 5.14. Spectrograms of wall pressure fluctuation for a pulsatile flow cycle

This figure clearly shows that the signal intensity is higher in the systolic part of the flow than in the diastolic part. It is understood that the highest signal intensity is that of the high slope and overlapping models and the lowest one is of the asymmetric case. This shows that the sound emitted from the high slope and overlapping models are more audible, which is consistent with the results obtained from the energy spectrum plots.

The wall pressure data obtained from the straight vessel and the maximum excitation points of stenosed models are converted into sound by using `soundsc` function of MATLAB. These sounds are different from the murmurs auscultated by a medical doctor through the skin with devices such as a stethoscope. The murmurs heard by the doctors are weakened as they spread from the vessel to the surrounding soft tissue. In addition, they become polluted by mixing with sounds generated during heartbeat and breathing. However, the sounds presented in this study are not exposed to such effects that distort their quality because they are directly obtained from inside the stenosed vessel. If a sensor technology can be developed to detect these murmurs from within the vessel, the obtained sounds can be used by the medical doctors for non-invasive diagnosis of the vascular stenosis. Generated sound files are attached to this thesis.

It is seen that the intensity of the sound emitted from the stenosed models is directly related to the fluctuation magnitude of the wall pressure. Accordingly, the sound levels are the highest for the high slope and overlapping models and lowest for the asymmetric one. The pressure fluctuation pattern is identified as another important factor affecting the characteristics of the emitted sound. It is known that the actual sound patterns obtained by Doppler ultrasonography, which is used to detect stenosed vessels, transform from triphasic configuration, heard in healthy blood vessels, to biphasic or monophasic configurations according to the severity of the stenosis [55]. This is actually the case for the sounds obtained from the current simulations. Once again it is important to note that these results can only be obtained with pulsatile simulations.

When the findings obtained are evaluated from a diagnostic point of view, it is seen that by means of a sensor technology that can measure the sound signals generated in the stenosed vessel valuable information can be obtained related to the shape of the stenosed region. Unfortunately, the morphological structure of the stenotic region is not considered in any of the current acoustic detection (AD) systems. This study showed that different shapes of stenoses affect the characteristics of the sounds emitted from stenosed arteries. Therefore, if acoustic-based systems are wanted to be developed for non-invasive diagnosis of stenosis, stenosis shape should also be considered in addition to stenosis severity. In this sense, this study aims to provide a valuable contribution to the literature.

## 5.4 Conclusion

Numerous numerical and experimental studies in the literature investigating the flow through a stenotic blood vessel include studies (although few in number) that examine the effect of different stenosis shapes on the post-stenosis flow regime. In these studies, researchers have not addressed the effect of different stenosis shapes on the sound emitting from stenosed vessels. The present study is carried out to fill this gap by investigating the effects of six different stenosis shapes (based on the elliptic stenosis shape) on the flow regime and emitting sound after the stenosis with the same severity, and determining the information provided for the purpose of non-invasive diagnosis. In the simulations performed for this purpose, physiological pulsatile flow as the inlet flow condition and non-Newtonian blood model as the fluid are used.

According to the mean axial velocity profiles at the maximum velocity instant of the pulsatile flow the length of the region where the flow is fully developed is shorter for short, high slope and overlapping stenosis shapes. It is also seen that high slope and overlapping models leads to a higher pressure drop at post-stenotic region. These models also shorten the length of the flow jet, trigger turbulence and increase vorticity magnitude at the stenosis outlet. On the contrary, the asymmetry

in the morphology of a stenosis leads to an opposite effect. The acoustic pressure contours show that high slope and overlapping stenosis models shorten the length of the region where the acoustic pressure intensity is high at higher frequencies. RMS of fluctuating wall pressured indicated that the high slope and consecutive forms of stenosis increase the severity of pressure fluctuations in the vessel wall in contrast to the asymmetric stenosis.

The wall pressure data obtained for a pulsatile flow cycle from the maximum activity points showed that the high slope and overlapping stenosis shapes increased the pressure fluctuation intensity and the duration of the high fluctuation intensity. These stenosis morphologies also increases the acoustic signal strength of stenosis induced vascular murmurs and frequency value at which these murmurs are generated. This makes it easier for the generated sound to be detected. Asymmetric stenosis model show a contrary effect on both wall pressure fluctuation intensity, acoustic signal strength and the frequency level at which the arterial murmurs are generated.

The sounds attached to this paper are generated using the pressure data obtained from the maximum activity points as an original contribution to the literature. These sounds leads to the interpretation that the high slope and overlapping stenosis shapes generates pressure fluctuation with higher intensity. This causes the sound emitted from the stenosed vessels with this shape to be harsher. Moreover, the fluctuation pattern affects the sound pattern. Sounds from healthy vessel and all forms of stenosis can be categorised as triphasic and biphasic sounds, respectively, according to the labels that doctors employ to classify the sounds emitted from stenosed vessels by means of doppler ultrasonography. This result suggests that numerical studies for acoustic based non-invasive diagnosis of stenosis should be performed under pulsatile flow conditions.

In conclusion, since the sounds emitted from the vessels with different stenosis shapes have different sound patterns, they can provide important information about

the shape of the stenosed region. Therefore, if an acoustic-based diagnostic system is to be developed, the stenosis shape must be taken into account.

# CHAPTER 6

# CONCLUSIONS AND FUTURE WORK

## 6.1 Conclusions

Atherosclerosis is one of the most frequent vascular diseases where a stenosis may develop in an artery which originates from narrowing of the vessel diameter. This pathology adversely affects blood flow. Acoustic radiations from the vessel during blood flow might be a sign of stenosis in blood vessels. In this study, LES are conducted to investigate the wall pressure fluctuations and resulting acoustic emission after stenosis in detail using OpenFOAM. For this purpose, simplified stenosed vessel models with different severities and shapes are used. Numerical simulations are conducted under both non-pulsatile and pulsatile flow configurations. Especially, high frequency pressure fluctuations arising from the turbulent flow around the stenosed region and the resulting acoustic emission are studied in detail, with the motivation of being able to use the results for non-invasive diagnostic purposes. The findings of this study are summarised chapter-wise, which are given below.

In Chapter 3, flow through vessel models with blunt axisymmetric and eccentric stenoses are investigated by LES under non-pulsatile flow conditions. The working fluid is chosen as water in order to be able to compare the results with that of previous studies. The effects of flow rate and radial eccentricity are investigated. For this purpose, simulations are performed with axisymmetric stenosis model at $Re = 1000$ and 2000 and with 16% and 32% eccentric stenosis models at $Re = 1000$. Increasing $Re$ for the axisymmetric model leads to a TKE rise.

Eccentricity also causes an increase in the TKE level. Calculated amplitude and spatial-spectral distribution of acoustic pressures at the post-stenotic region are compared with previous experimental and theoretical results. It is found that increasing the $Re$ does not change the location of the maximum RMS wall pressure fluctuations but causes a general increase in the spectrum level, although the change in the shape of the spectrum is not significant. On the other hand, eccentricity leads to a shift forward at the location of the maximum RMS wall pressure and an increase at the spectrum level in comparison with the axisymmetric model at the same $Re$. This effect becomes more distinct when radial eccentricity of the stenosis increases. Both the flow rate and eccentricity of the stenosis shape are evaluated to be clinically important parameters for non-invasive diagnosis of stenosis.

In Chapter 4, the effects of stenosis severity and eccentricity on the post-stenotic flow field and the murmurs radiated from the stenosed arteries are investigated by applying LES. Five different severities (50%, 60%, 75%, 87% and 95%) of axisymmetric and eccentric elliptical stenosis model have been used in these simulations. These simulations are conducted under physiological pulsatile flow conditions by using a non-Newtonian blood model as the fluid. The turbulent activity at the post-stenotic regions which is the reason for the generation of murmurs is seen to be started with the stenosis severity of 75%. This outcome is consistent with the given critical stenosis severity level in the literature. Increased stenosis severity and eccentricity have been found to increase turbulence activity and acoustic pressure intensity in the post-stenotic region. In addition, the energy level of the turbulent pressure flucuations at the break frequency increases with the severity of the stenosis and eccentricity. This situation leads to a stronger acoustic signal emission from the stenosed vessel. These signals, which are taken from the maximum activity locations, have been transformed into sound and more easily detectable murmur levels appeared at severer stenoses. It is determined that acoustically most active region of eccentric vessels is the position where the flow jet is directed. The sound emitted from this region is stronger than the axisymmetric

narrowing of the same stenosis severity. These results show that stenosis severity and eccentricity are two important parameters to be considered in developing acoustic based diagnostic methods.

In Chapter 5, effect of stenosis shape on the post-stenotic pressure fluctuations and the sound emitted from a stenosed blood vessel is studied. Simulations are performed with the same settings in Chapter 4. Findings indicate that the proximity of stenosis throat to stenosis entrance and overlapping of more than one stenosis shortens the length of the flow jet, trigger turbulence, increase vortical activity, turbulent kinetic energy and pressure fluctuations magnitude at the post-stenotic region. In addition, these morphological parameters strengthen the audible signal especially in the systolic phase of the pulsatile flow. On the other hand, asymmetry in stenosis form creates an opposite effect. It is another result obtained in this study that the pattern of pressure fluctuations affect the pattern of the audible sound. Accordingly, since stenosis shapes lead to different pressure fluctuation patterns, the sounds emitted from the vessels having these stenosis shapes are heard in different patterns. When examined from a diagnostic point of view, these findings indicate that morphological differences at stenotic region leads to noticeable changes in noise signals. Therefore, while developing acoustic based diagnostic techniques stenosis shape should also be considered in addition to stenosis severity.

We believe that the results presented in this thesis give a better insight and in-depth knowledge on the important fluid dynamics aspects of transient blood flow that are usually present in real-life pathological atherosclerotic arteries. In addition, a considerable contribution has been made to the literature on the importance of stenosis severity and different morphological parameters in the stenosed region on detecting these pathologies by means of a non-invasive acoustic manner.

## 6.2 Future Work

The recommendations for future work, based on the findings in the thesis, are given below.

- For simplicity, idealized vessel like models have been used in the present study. So, in future, more realistic models like curved and bifurcated vessels such as aorta and carotid arteries can be considered.
- We have assumed that the stenosis is formed by smooth mathematical functions such as a cosine curve. But in reality, this is not generally the case. Atherosclerotic vessels usually contains many small valleys and ridges which suggests that the more realistic biological stenosis wall is rough rather than smooth. So, in future, the irregular arterial stenosis obtained by means of MRA and/or CT images can be considered.
- In real life, there are structures such as soft tissues, muscles, bones and chest and abdominal cavity in the distance from the blood vessels to the skin surface. The effects of these structures on emission of generated arterial murmurs through the skin can be investigated by means of fluid-structure interactions.
- In this study, only the sounds generated on the vascular wall are examined. Additionally, the sound produced in the flow can be examined by coupling CFD solutions with the solutions obtained using acoustic models. By using this method, all of the acoustic propagation up to the skin surface can be solved.

## REFERENCES


[1] E. J. Benjamin, S. S. Virani, C. W. Callaway, A. R. Chang, S. Cheng, S. E. Chiuve, M. Cushman, F. N. Delling, R. Deo and S. S. de Ferranti, "Heart Disease and Stroke Statistics," American Heart Association, 2018.

[2] R. Ross, "Atherosclerosis-an inflammatory disease," *The New England Journal of Medicine*, vol. 340, pp. 115-126, 1999.

[3] The University of Utah Eccles Health Sciences Library, "The Internet Pathology Laboratory for Medical Education," [Online]. Available: https://library.med.utah.edu/WebPath. [Accessed 04 06 2018].

[4] H. E. Davies, C. G. Wathen and F. V. Gleeson, "The risks of radiation exposure related to diagnostic imaging and how to minimise them," *BMJ*, vol. 342, 2011.

[5] P. Doriot, P. Dorsaz, L. Dorsaz and W. Rutishauser, "Overestimation of stenosis severity by single plane geometric measurements," in *Computers in Cardiology*, Indianapolis, USA, 1996.

[6] J. S. Stroud, S. A. Berger and D. Saloner, "Numerical analysis of flow through a severely stenotic carotid artery bifurcation," *Journal of Biomechanical Engineering*, vol. 124, no. 1, pp. 9-20, 2002.

[7] G. J. Crystal and L. W. Klein, "Fractional flow reserve: physiological basis, advantages and limitations, and potential gender differences," *Current Cardiology Reviews*, vol. 11, no. 3, pp. 209-219, 2015.

[8] A. O. Borisyuk, "Experimental study of wall pressure fluctuations in rigid and elastic pipes behind an axisymmetric narrowing," *Journals of Fluids and Strucures,* vol. 26, pp. 658-674, 2010.

[9] M. M. Kartchner and L. P. McRae, "Auscultation for carotid bruits in cerebrovascular insufficiency," *J. Am. Med. Assoc.,* vol. 210, no. 3, pp. 494-497, 1969.

[10] R. S. Lees and C. F. Dewey, "Phonoangiography: a new noninvasive diagnostic method for studying arterial disease," *Proceedings of the National Academy of Sciences of the United States of America,* vol. 67, no. 2, pp. 935-942, 1970.

[11] H. W. Townes, J. M. Bowers and H. A. Braun, "Characteristics of innocent and stenotic cervical bruits," *Am Heart J,* vol. 79, pp. 734-741, 1970.

[12] M. M. Kartchner, L. P. McRae and F. D. Morrison, "Noninvasive detection and evaluation of carotid occlusive disease," *Arch. Surg.,* vol. 106, pp. 528-535, 1973.

[13] M. D. Ginsberg, S. A. Greenwood and H. I. Goldberg, "Noninvasive diagnosis of extracranial cerebrovascular disease: oculoplethysmography-phonoangiography and directional Doppler ultrasonography," *Neurology,* vol. 29, no. 5, pp. 623-631, 1979.

[14] S. L. House, K. Mahalingam, L. J. Hyland, E. B. Ferris, A. J. Comerota and J. J. Cranley, "Noninvasive flow techniques in the diagnosis of cerebrovascular disease," *Surgery,* vol. 87, no. 6, pp. 696-700, 1980.

[15] D. E. Strandness, "Noninvasive evaluation of arteriosclerosis. Comparison of methods.," *Arteriosclerosis,* vol. 3, pp. 103-116, 1983.

[16] C. T. Facts, "Advanced Analysis of the Carotid Phonoangiography and Diseases," [Online]. Available: http://www.clinicaltrialfacts.com/Carotid-Atherosclerosis/Advanced-Analysis-of-the-Carotid-Phonoan-144780. [Accessed 22 08 2018].

[17] G. W. Duncan, J. O. Gruber, C. F. Dewey, G. S. Myers and R. S. Lees, "Evaluation of carotid stenosis by phonoangiography," *New England Journal of Medicine,* vol. 293, no. 22, pp. 1124-1128, 1975.

[18] B. Kim and W. Corcoran, "Experimental measurement of turbulence spectra distal to stenosis," *Journal of Biomechanics,* vol. 7, pp. 335-342, 1974.

[19] C. Clark, "Turbulent velocity measurements in a model of aortic stenosis," *Journal of Biomechanics,* vol. 9, pp. 677-687, 1976.

[20] C. Clark, "Turbulent wall pressure measurements in a model of aortic stenosis," *Journal of Biomechanics,* vol. 10, pp. 461-472, 1977.

[21] R. Tobin and I. Chang, "Wall pressure spectra scaling downstream of stenoses in steady tube flow," *Journal of Biomechanics,* vol. 9, pp. 633-640, 1976.

[22] J. Fredberg, "Origin and character of vascular murmurs: Model studies," *Journal of the Acoustical Society of America,* vol. 61, no. 4, pp. 1077-1085, 1977.

[23] R. L. Kirkeeide, D. F. Young and N. R. Cholvin, "Wall vibrations induced by flow through simulated stenoses in models and arteries," *Journal of Biomechanics,* vol. 10, pp. 431-444, 1977.

[24] J. P. Kistler, R. S. Lees, J. Friedman, M. Pressin, J. P. Mohr, G. S. Roberson and R. G. Ojeman, "The Bruit of Carotid Stenosis Versus Radiated Basal Heart Murmurs," *Circulation,* vol. 57, pp. 975-981, 1977.

[25] A. Miller, R. S. Lees, J. P. Kistler and W. M. Abbott, "Spectral analysis of arterial bruits (phonoangiography): Experimental validation," *Circulation,* vol. 61, no. 3, pp. 515-520, 1980.

[26] R. Knox, P. Breslau and D. E. Strandness, "Quantitative Carotid Phonoangiography," *Stroke,* vol. 12, pp. 798-803, 1981.

[27] P. C. Lu, D. R. Gross and N. H. C. Hwang, "Intravascular pressure and velocity fluctuations in pulmonic arterial stenosis," *Journal of Biomechanics,* vol. 13, pp. 291-300, 1980.

[28] P. C. Lu, C. N. Hui and N. H. C. Hwang, "A model investigation of the velocity and pressure spectra in vascular murmurs," *Journal of Biomechanics,* vol. 16, no. 11, pp. 923-931, 1983.

[29] S. A. Jones and A. Fronek, "Analysis of break frequencies downstream of a constriction in a cylindrical tube," *Journal of Biomechanics,* vol. 20, pp. 319-327, 1987.

[30] S. Abdallah and N. Hwang, "Arterial stenosis murmurs: an analysis of flow and pressure field," *Journal of the Acoustical Society of America,* vol. 83, pp. 318-334, 1988.

[31] A. O. Borisyuk, "Modeling of noise generation by a vascular stenosis," *International Journal of Fluid Mechanics Research,* vol. 29, no. 1, pp. 65-86, 2002.

[32] A. O. Borisyuk, "Experimental study of wall pressure fluctuations in a pipe behind a stenosis," *International Journal of Fluid Mechanics Research,* vol. 30, no. 3, pp. 264-278, 2003.

[33] A. O. Borisyuk, "Experimental Study ofWall Pressure Fluctuations in a Pipe behind a Cylindrical Insertion with Eccentricity," *International Journal of Fluid Mechanics Research,* vol. 31, no. 2, pp. 160-175, 2004.

[34] A. O. Borisyuk, "Study of the Flow and Acoustic Fields in a Rigid-Walled Channel of Circular Cross-Section with a Local Axisymmetric Narrowing. Numerical Results," *International Journal of Fluid Mechanics Research,* vol. 34, no. 3, pp. 191-209, 2007.

[35] Y. Yazıcıoğlu, T. J. Royston, T. Spohnholtz, B. Martin, F. Loth and H. S. Bassiouny, "Acoustic radiation from a fluid-filled, subsurface vascular tube with internal turbulent flow due to a constriction," *Journal of Acoustical Society of America,* vol. 118, no. 2, pp. 1193-1209, 2005.

[36] R. Mittal, S. P. Simmons and H. S. Udaykumar, "Application of Large-Eddy Simulation to the Study of Pulsatile Flow in a Modeled Arterial Stenosis," *Journal of Biomechanical Engineering,* vol. 123, pp. 325-332, 2001.

[37] R. Mittal, S. Simmons and F. Najjar, "Numerical study of pulsatile flow in a constricted channel," *Journal of Fluid Mechanics,* vol. 485, pp. 337-378, 2003.

[38] O. R. Tutty, "Pulsatile flow in a constricted channel," *Journal of Biomechanical Engineering,* vol. 114, pp. 50-54, 1992.

[39] S. S. Varghese, S. H. Frankel and P. F. Fischer, "Direct numerical simulation of stenotic flows. Part 1. Steady flow," *Journal of Fluid Mechanics,* vol. 582, pp. 253-280, 2007.

[40] S. S. Varghese, S. Frankel and P. F. Fischer, "Direct numerical simulation of stenotic flows. Part 2. Pulsatile flow," *J. Fluid Mech.,* vol. 582, pp. 281-318, 2007.

[41] M. C. Paul, M. M. Molla and G. Roditi, "Large–Eddy simulation of pulsatile blood flow," *Medical Engineering and Physics,* vol. 31, pp. 153-159, 2009.

[42] A. Khair, A. Hossain, B. C. Wang, D. Kuhn and M. Molla, "Direct numerical simulation ofphysiological pulsatile flow through a stenotic channel," in *Turbulence, Heat and Mass Transfer*, Palermo, Italy, 2012.

[43] M. M. Molla and M. C. Paul, "Large Eddy Simulation of pulsatile flow through a channel with double constriction," *Fluids,* vol. 2, no. 1, pp. 1-19, 2017.

[44] J. H. Seo and R. Mittal, "A coupled flow-acoustic computational study of bruits from a modeled stenosed artery," *Medical and Biological Engineering and Computing,* vol. 50, pp. 1025-1035, 2012.

[45] S. Zhu, J. H. Seo, H. Bakhshaee and R. Mittal, "A computational method for analyzing the biomechanics of arterial bruits," *Journal of Biomechanical Engineering,* vol. 139, pp. 1-9, 2017.

[46] J. H. Seo, H. Bakhshaee, G. Garreau, C. Zhu, A. Andreou, W. R. Thompson and R. Mittal, "A method for the computational modeling of the physics of heart murmurs," *Journal of Computational Physics,* vol. 336, pp. 546-568, 2017.

[47] H. E. Salman, C. Sert and Y. Yazıcıoğlu, "Computational analysis of high frequency fluid–structure interactions in constricted flow," *Computers and Structures,* vol. 122, pp. 145-154, 2013.

[48] H. E. Salman and Y. Yazıcıoğlu, "Investigation of on skin surface response due to acoustic radiation from stenosed blood vessels," *The Journal of the Acoustical Society of America,* vol. 138, pp. 1747-1758, 2015.

[49] H. E. Salman and Y. Yazıcıoğlu, "Flow-induced vibration analysis of constricted artery models with surrounding soft tissue," *The Journal of the Acoustical Society of America*, vol. 142, pp. 1913-1925, 2017.

[50] K. Özden, C. Sert and Y. Yazıcıoğlu, "Numerical investigation of wall pressure fluctuations downstream of ideal and realistic stenosed vessel models," in *CMBBE*, Lisbon, 2018.

[51] A. N. Makaryus, J. N. Makaryus, A. Figgatt, D. Mulholland, H. Kushner, J. L. Semmlow, J. Mieres and A. J. Taylor, "Utility of an Advanced Digital Electronic Stethoscope in the Diagnosis of Coronary Artery Disease Compared With Coronary Computed Tomographic Angiography," *The American Journal of Cardiology*, vol. 111, no. 6, pp. 786-792, 2013.

[52] M. C. Grenier, K. Gagnon, J. Genest, J. Durand and L. G. Durand, "Clinical Comparison of Acoustic and Electronic Stethoscopes and Design of a New Electronic Stethoscope," *The American Journal of Cardiology*, vol. 81, no. 5, pp. 653-656, 1998.

[53] "CADence System," AUM Cardiovascular, [Online]. Available: https://aumcardio.com/cadence-system/. [Accessed 04 08 2018].

[54] "CADScor System," Acarix, [Online]. Available: http://www.acarix.com/our-technology/. [Accessed 04 08 2018].

[55] J. L. Thomas, S. Winther, R. F. Wilson and M. Bottcher, "A novel approach to diagnosing coronary artery disease: acoustic detection of coronary turbulence," *The International Journal of Cardiovascular Imaging*, vol. 33, pp. 129-136, 2017.

[56] F. Azimpour, E. Caldwell, P. Tawfik, S. Duval and R. F. Wilson, "Audible coronary artery stenosis," *The American Journal of Medicine,* vol. 129, no. 5, pp. 515-521, 2016.

[57] S. Winther, S. E. Schmidt, N. R. Holm, E. Toft, J. J. Strujik, H. E. Bøtker and M. Bøttcher, "Diagnosing coronary artery disease by sound analysis from coronary stenosis induced turbulent blood flow: diagnostic performance in patients with stable angina pectoris," *Int J Cardiovasc Imaging,* vol. 32, no. 2, pp. 235-245, 2016.

[58] H. K. Versteeg and W. Malalasekera, An Introduction To Computational Fluid Dynamics. The Finite Volume Method., London: Pearson Education Limited, 2007.

[59] J. Tu, G. H. Yeoh and C. Liu, Computational Fluid Dynamics. A Practical Approach., Oxford: Elsevier, 2008.

[60] SimVascular. [Online]. Available: http://simvascular.github.io/. [Accessed 24 08 2018].

[61] CRIMSON. [Online]. Available: http://www.crimson.software/. [Accessed 24 08 2018].

[62] D. Bluestein, "Utilizing Computational Fluid Dynamics in Cardiovascular Engineering and Medicine—What You Need to Know. Its Translation to the Clinic/Bedside," *Artificial Organs,* vol. 41, no. 2, pp. 117-121, 2017.

[63] D. C. Barber and D. R. Hose, "Automatic segmentation of medical images using image registration: diagnostic and simulation applications," *J Med Eng Technol,* vol. 29, pp. 53-63, 2005.

[64] W. P. Donders, W. Huberts, F. N. van de Vosse and T. Delhaas, "Personalization of models with many model parameters: an efficient

sensitivity analysis approach," *Int J Numer Method Biomed Eng,* vol. 31, no. 10, pp. 1-18, 2015.

[65] D. N. Ku, "Blood flow in arteries," *Annual Review of Fluid Mechanics,* vol. 29, pp. 399-434, 1997.

[66] H. Tennekes and J. L. Lumley, A First Course In Turbulence, MIT Press, 1972.

[67] S. S. Varghese and S. H. Frankel, "Numerical modeling of pulsatile turbulent flow in stenotic vessels," *Journal of Biomechanical Engineering,* vol. 125, pp. 445-460, 2003.

[68] T. S. Lee, W. Liao and H. T. Low, "Numerical simulation of turbulent flows through series stenoses," *Int. J. Numer. Meth. Fluids,* vol. 42, no. 7, pp. 717-740, 2003.

[69] T. S. Lee, W. Liao and H. T. Low, "Numerical study of physiological turbulent flows through series arterial stenoses," *Int. J. Numer. Meth. Fluids,* vol. 46, no. 3, pp. 315-344, 2004.

[70] M. X. Li, J. J. B-Brandt, P. R. Hoskins and W. J. Easson, "Numerical analysis of pulsatile blood flow and vessel wall mechanics in different degrees of stenoses," *Journal of Biomechanics,* vol. 40, pp. 3715-3724, 2007.

[71] A. Scotti and U. Piomelli, "Turbulent models in pulsating flows," *AIAA Journal,* vol. 40, no. 3, pp. 537-544, 2002.

[72] A. Scotti and U. Piomelli, "Numerical Simulation of Pulsating Turbulent Channel Flow," *Phys. Fluids A,* vol. 13, no. 5, pp. 1367-1384, 2001.

[73] S. S. Varghese, S. H. Frankel and P. F. Fischer, "Modeling transition to turbulence in eccentric stenotic flows," *Journal of Biomechanical Engineering,* vol. 130, no. 1, pp. 1-7, 2008.

[74] F. P. P. Tan, N. B. Wood, G. Tabor and X. Y. Xu, "Comparison of LES of Steady Transitional Flow in an Idealized Stenosed Axisymmetric Artery Model With a RANS Transitional Model," *Journal of Biomechanical Engineering,* vol. 133, no. 5, pp. 1-12, 2011.

[75] M. M. Molla, M. C. Paul and G. Roditi, "LES of additive and non-additive pulsatile flows in a model arterial stenosis," *Computer Methods in Biomechanics and Biomedical Engineering*, vol. 13, no. 1, pp. 105-120, 2010.

[76] A. Leonard, "Energy cascade in Large-Eddy Simulations of turbulent fluid flow," *Advances in Geophysics,* vol. 18A, pp. 237-248, 1974.

[77] M. Germano, U. Piomelli and W. Cabot, "A dynamic subgrid-scale eddy viscosity model," *Physics of Fluids A,* vol. 3, no. 7, pp. 1760-1765, 1991.

[78] L. di Mare and W. P. Jones, "LES of turbulent flow past a swept fence," *International Journal of Heat and Fluid Flow*, vol. 24, pp. 606-615, 2003.

[79] J. Smagorinsky, "General circulation experiment with the primitive equations. i. the basic experiment," *Monthly Weather Rev.,* vol. 91, pp. 99-164, 1963.

[80] E. de Villiers, The Potential of Large Eddy Simulation for the Modeling of Wall Bounded Flows, PhD Thesis: Imperial College of Science, Technology and Medicine, 2006.

[81] I. Çelik, M. Klein and J. Janicka, "Assessment measures for engineering LES applications," *Journal of Fluids Engineering,* vol. 131, pp. 1-10, 2009.

[82] SIEMENS, STAR CCM+ Documentation, 2017.

[83] I. B. Çelik, Z. N. Çehreli and I. Yavuz, "Index of Resolution Quality for Large Eddy Simulations," *Journal of Fluid Engineering,* vol. 127, pp. 949-958, 2005.

[84] L. H. Back and E. J. Roschke, "Shear-Layer Flow Regimes and Wave Instabilities and Reattachment Lengths Downstream of an Abrupt Circular Channel Expansion," *Journal of Applied Mechanics,* vol. 39, no. 3, pp. 677-681, 1972.

[85] M. C. Paul and M. M. Molla, "Investigation of physiological pulsatile flow in a model arterial stenosis using large eddy and direct numerical simulations," *Applied Mathematical Modeling,* vol. 36, pp. 4393-4413, 2012.

[86] T. G. Beach, C. L. Maarouf, R. G. Brooks, S. Shirohi, I. D. Daugs, L. I. Sue, M. N. Sabbagh, D. G. Walker, L. Lue and A. E. Roher, "Reduced clinical and postmortem measures of cardiac pathology in subjects with advanced Alzheimer's Disease," *BMC Geriatr,* vol. 11, pp. 1-7, 2011.

[87] Q. Long, X. Y. Xu, K. V. Ramnarine and P. Hoskins, "Numerical investigation of physiologically realistic pulsatile flow through arterial stenosis," *Journal of Biomechanics,* vol. 34, pp. 1229-1242, 2001.

[88] D. A. Steinman, T. L. Poepping, M. Tambasco, R. N. Rankin and D. W. Holdsworth, "Flow Patterns at the Stenosed Carotid Bifurcation: Effect of Concentric versus Eccentric Stenosis," *Annals of Biomedical Engineering,* vol. 28, pp. 415-423, 2000.

[89] D. F. Young and F. Y. Tsai, "Flow characteristics in models of arterial stenoses - I. Steady flow," *Journal of Biomechanics,* vol. 6, pp. 395-410, 1973.

[90] H. M. Loree, R. D. Kamm, C. M. Atkinson and R. T. Lee, "Turbulent pressure fluctuations on surface of model vascular stenoses," *American Journal of Physiology,* vol. 261, pp. 644-650, 1991.

[91] S. Waxman, M. A. Mittleman, S. W. Zarich, S. W. Fitzpatrick, S. M. Lewis, D. E. Leeman, S. J. Shubrooks, G. S. Abela and R. W. Nesto, "Plaque disruption and thrombus in Ambrose's angiographic coronary lesion types," *The American Journal of Cardiology,* vol. 92, no. 1, pp. 16-20, 2003.

[92] C. Tu and M. Deville, "Pulsatile flow of non-newtonian fluids through arterial stenoses," *Journal of Biomechanics,* vol. 29, no. 7, pp. 899-908, 1996.

[93] T. Ishikawa, L. Guimaraes, S. Oshima and R. Yamane, "Effect of non-newtonian property of blood on flow through a stenosed tube," *Fluid Dyn. Res.,* vol. 22, pp. 251-264, 1998.

[94] P. Mandal, "An unsteady analysis of non-newtonian blood flow through tapered arteries with a stenosis," *Int. J. Non-Linear Mech.,* vol. 40, pp. 151-164, 2005.

[95] A. M. Walker, C. R. Johnston and D. E. Rival, "On the Characterization of a Non-Newtonian Blood Analog and Its Response to Pulsatile Flow Downstream of a Simplified Stenosis," *Annals of Biomedical Engineering,* vol. 42, no. 1, pp. 97-109, 2014.

[96] M. M. Molla, "LES of Pulsatile Flow in the Models of Arterial Stenosis and Aneurysm, MSc Thesis," *Department of Mechanical Engineering University of Glasgow*, May 2009.

[97] B. Wiwatanapataphee, D. Poltern, Y. H. Wu and Y. Lenbury, "Simulation of pulsatile flow of blood in stenosed coronary artery bypass with graft," *Mathematical Biosciences and Engineering*, vol. 3, pp. 371-383, 2006.

[98] V. J. Shinde, J. P. Laval and M. Stanislas, "Effect of mean pressure gradient on the turbulent wall pressure–velocity correlations," *Journal of Turbulence*, vol. 15, no. 12, pp. 833-856, 2014.

[99] C. Zhu, J. H. Seo and R. Mittal, "Computational modelling and analysis of haemodynamics in a simple model of aortic stenosis," *Journal of Fluid Mechanics*, vol. 851, pp. 23-49, 2018.

[100] K. Bhaganagar, "Direct numerical simulation of flow in stenotic channel to understand the effect of stenotic morphology on," *Journal of Turbulence*, vol. 10, pp. 1-16, 2009.

[101] J. S. Stroud, S. A. Berger and D. Saloner, "Influence of stenosis morphology on flow through severely stenotic vessels: implications for plaque rupture," *Journal of Biomechanics*, vol. 33, pp. 443-455, 2000.

[102] J. Huston, D. A. Nichols, P. H. Luetmer, C. H. Rydberg, B. D. Lewis, F. B. Meyer, R. D. Brown and C. D. Schleck, "MR angiographic and sonographic indications for endraterectomy," *American Journal of Neuroradiology*, vol. 19, pp. 309-315, 1998.

[103] B. E. Cil, E. Akpınar, B. Peynircioğlu and S. Çekirge, "Utility of covered stents for extracranial internal carotid artery stenosis," *American Journal of Neuroradiology*, vol. 25, pp. 1168-1171, 2004.

[104] B. F. Ferrari, N. Wolosker, R. A. Rosoky, G. D'Ippolito, A. M. B. Wolosker and P. Puech-Leao, "Natural history of stenosis in the iliac arteries in patients with intermittent claudication undergoing clinical tratment," *Revista Do Hospital Das Clinicas*, vol. 59, pp. 341-348, 2004.

[105] P. Ward, "MRI and CT provide substantial boost to ischemic stroke care," in *European Congress of Radiology*, 2012.

[106] S. Singh and R. R. Shah, "A numerical model for the effect of stenosis shape on blood flow through an artery using power-law fluid," *Advances in Applied Science Research*, vol. 1, pp. 66-73, 2010.

[107] V. P. Sristava, S. Mishra and R. Rastogi, "Non-Newtonian Arterial Blood Flow through an Overlapping Stenosis," *Applications and Applied Mathematics*, vol. 5, no. 1, pp. 225-238, 2010.

## CURRICULUM VITAE

**Contact Information:**

Middle East Technical University

Department of Mechanical Engineering, Ankara, Turkey

*Office Phone:* +90 312 210 5245 *Email:* kozden@metu.edu.tr

*Mobile Phone:* +90 537 927 4017 kamil.ozden.me@gmail.com

**Education:**

- **B.Sc.,** Mechanical Engineering, Middle East Technical University, 2009
  CGPA: 2.71/4.00
- **M.Sc.,** Mechanical Engineering, Middle East Technical University, 2012
  CGPA: 3.36/4.00

  **Thesis Title:** Investigation of Reducing Run Time in Vehicle Level Finite Element Analyses for Curtain Airbag Development

  **Supervisor:** Prof. Dr. Mustafa İlhan Gökler

  **Co-supervisor:** Dr. Mustafa Erdener

- **Ph.D.,** Mechanical Engineering, Middle East Technical University, 2018
  CGPA: 3.64/4.00

  **Thesis Title:** Large Eddy Simulation of Pressure Fluctuations Inside Stenosed Blood Vessels Towards Noninvasive Diagnosis of Atherosclerosis

  **Supervisor:** Assoc. Prof. Dr. Cüneyt Sert,

  **Co-supervisor:** Assoc. Prof. Dr. Yiğit Yazıcıoğlu

**Areas of Expertise:**

- Computational Fluid Dynamics, Turbulence Modeling,
- Flow-generated bioacoustics
- Parallel computing, Multidomain modeling, Signal processing
- Crash simulation, Airbag folding and deployment simulation

**Experience:**

- Middle East Technical University, Research Assistant, (2009-2018)
    - Instructor: *ME 105 Computer Aided Engineering Graphics (2016 – 2018)*
    - Administrative Assistant: *Exam, Course and Workload Schedules (2014–2016)*
    - Course Assistant in ME Courses: *Mechanical Engineering Systems Laboratory, Statics, Manufacturing Technologies, Principles of Production Engineering, Manufacturing Engineering, Engineering Economy and Production Management*
- A New Overhead Rail System (Feb. 2010 – Dec. 2010)
  *Funded by TOFAŞ A.Ş., this project is conducted to design a new overhead rail system for TOFAŞ A.Ş. to use in assembly operations.*
- Investigation of reducing run time in vehicle level finite element analyses for CAB development (Feb. 2012 – May 2013)
  *This is a SAN-TEZ project conducted in co-operation with Ford OTOSAN A.Ş.*
- Investigation of stenosis severities and shapes in blood vessels with numerical simulations for diagnostic purposes.
  *Funded by BAP – METU* (Jan. 2014- Dec. 2016)
- Investigation of acoustic radiation generated by stenoses in blood vessels with Large Eddy Simulations.
  *Funded by BAP – METU* (Jan. 2017 – June 2018)

**Software Skills:**

- CFD Solvers and Pre/Post-Processors: OpenFOAM, Fluent, Nektar++, Ansys CFX, Gmsh, ICEM CFD, Ansys Meshing, Paraview, TecPlot, Fluent, CFD-Post
- Programming: MATLAB, Mathcad
- Crash Simulations: Altair HyperCrash, LS-DYNA
- Computer Aided Design: Siemens NX, SolidWorks, Catia, KeyCreator

**Language Skills:** Turkish (Native Language), English (Proficient)

**Publications:**

***Journal Publications:***

- **K. Özden,** C. Sert, Y. Yazıcıoğlu, *"Numerical Investigation of Wall Pressure Fluctuations Downstream of Axisymmetric and Eccentric Blunt Stenosis Models",* submitted to Journal of Engineering in Medicine.
- **K. Özden,** C. Sert, Y. Yazıcıoğlu, *"Effect of Stenosis Shape on the Sound Emitted from a Constricted Vessel",* in preparation for submission
- **K. Özden,** C. Sert, Y. Yazıcıoğlu, *"Effect of Stenosis Severity and Eccentricity on the Sound Emitted from a Constricted Vessel",* in preparation for submission

***Conference Proceedings:***

- **K. Özden,** M. İ. Gökler, M. Erdener, *"Investigation of the Effect of Folding Types on Deployment Characteristics of Driver Airbag",* 6th OTEKON Congress, Bursa, Türkiye, June 2012
- **K. Özden,** C. Sert, Y. Yazıcıoğlu, *"Investigation of Acoustic Radiation in Blunt and Elliptical Stenosed Vessels"*, 23rd Congress of the European Society of Biomechanics, Seville, Spain, July 2017.

- **K. Özden,** C. Sert, Y. Yazıcıoğlu, *"Numerical Investigation of Wall Pressure Fluctuations Downstream of Ideal and Realistic Stenosed Vessel Models"*, 15th Int. Symposium on Computer Methods in Biomechanics and Biomedical Eng., Lisbon, Portugal, March 2018.

***Ongoing Studies:***

- **K. Özden**, C. Sert, Y. Yazıcıoğlu, *"Effect of Curvature and Bifurcation on Wall Pressure Fluctuations Downstream of Stenotic Vessels"*
- H. Alemdar, Y. Yazıcıoğlu, M. Cüneyitoğlu Özkul, H. E. Salman, **K. Özden**, C. Sert *"Prediction of Stenosis Severity and Morphology by means of Machine Learning"*